Implementation of Interface Friction Finite Elements

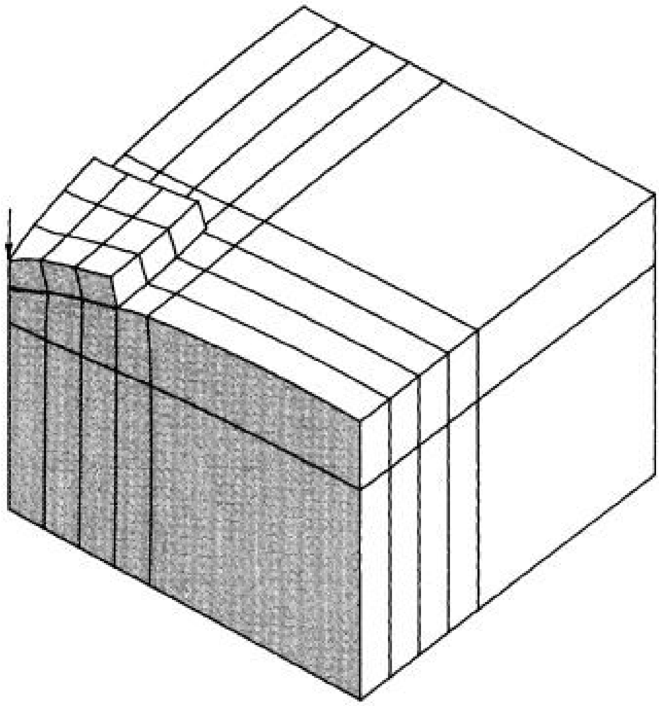

Stanislav Krejčí and Eira Lillestøl

Master thesis

Spring 2018

AALBORG UNIVERSITY
DENMARK

Structural & Civil Engineering, Aalborg University.

Aalborg University
Thomas Manns Vej 23
9220 Aalborg Ø
Phone 99408484
http://www.byggeri.aau.dk

AALBORG UNIVERSITY
STUDENT REPORT

Title:

Implementation of interface friction finite elements

Project:

4^{th} Semester - M.Sc. Structural and Civil Engineering

Project period:

September 1^{st} 2017 - June 8^{th} 2018

Master thesis group:

Stanislav Krejčí
Eira Lillestøl

Supervisor:

Johan Clausen

Pages: 58
Appendix: 40
End: June 8^{th} 2018

Abstract:

This thesis deals with a contact problems between dissimilar materials in geotechnics, specifically the interface between footing and soil. There are two groups of interface elements studied, the zero-thickness and thin-layer. Additionally there is analyzed the Augmented lagrange approach which is a part of the broader family of multi-freedom constraint solutions. The analysis is performed in commercial softwares such as MATLAB, Optum G2 and PLAXIS 2D. Furthermore the load bearing capacity is analyzed. The results are validated using the Chris Martin solution.

Stanislav Krejci　　Eira Lillestøl

Preface

The master thesis is produced by Stanislav Krejčí and Eira Lillestøl, studying on the 10^{th} semester of the MSc program "Structural and Civil Engineering" at Aalborg University. The thesis has been written in the period of September 1^{st} 2017 to the June 8^{th} 2018.

As a prerequisite for the reader, understanding of Finite Element Analysis, basic Continuum Mechanics and plasticity theory is advised.

The authors would like to address an expression of gratitude to our supervisor, Johan Clausen, for guidance and productive meetings.

Reading guide

In this master thesis, the references are done by Harvard method. Hence, in the text it will be shown as [Surname, Year] corresponding the a list at the end of the report. In the bibliography, the books and articles are listed with author, title, ISBN number for books, publisher and the year of release are presented.

When references are made within the master thesis, the equations are referred to in the text as Equation (1.1), whereas references to figures, tables, sections and chapters are done without brackets e.g. Section 1.1. However, references to Appendices are done by capital letters starting from A.

Structure of the thesis

This section describes the structure of the master thesis. The thesis starts by introducing the reader for project background and scope and limitations of the thesis. Thereafter, a formulation of the interfaces is carried out of the considered interface elements and are further explained and derived and the different constitutive relations are accounted for. Following, the interface elements presented in the formulation of interfaces are tested to detect the different element behaviors. This is done by a simple pull-out test. Furthermore, the model of the foundation is presented through MATLAB, PLAXIS 2D and Optum G2 where the different interface elements are implemented and compared. A flow chart of the thesis structure is seen in Figure 1.

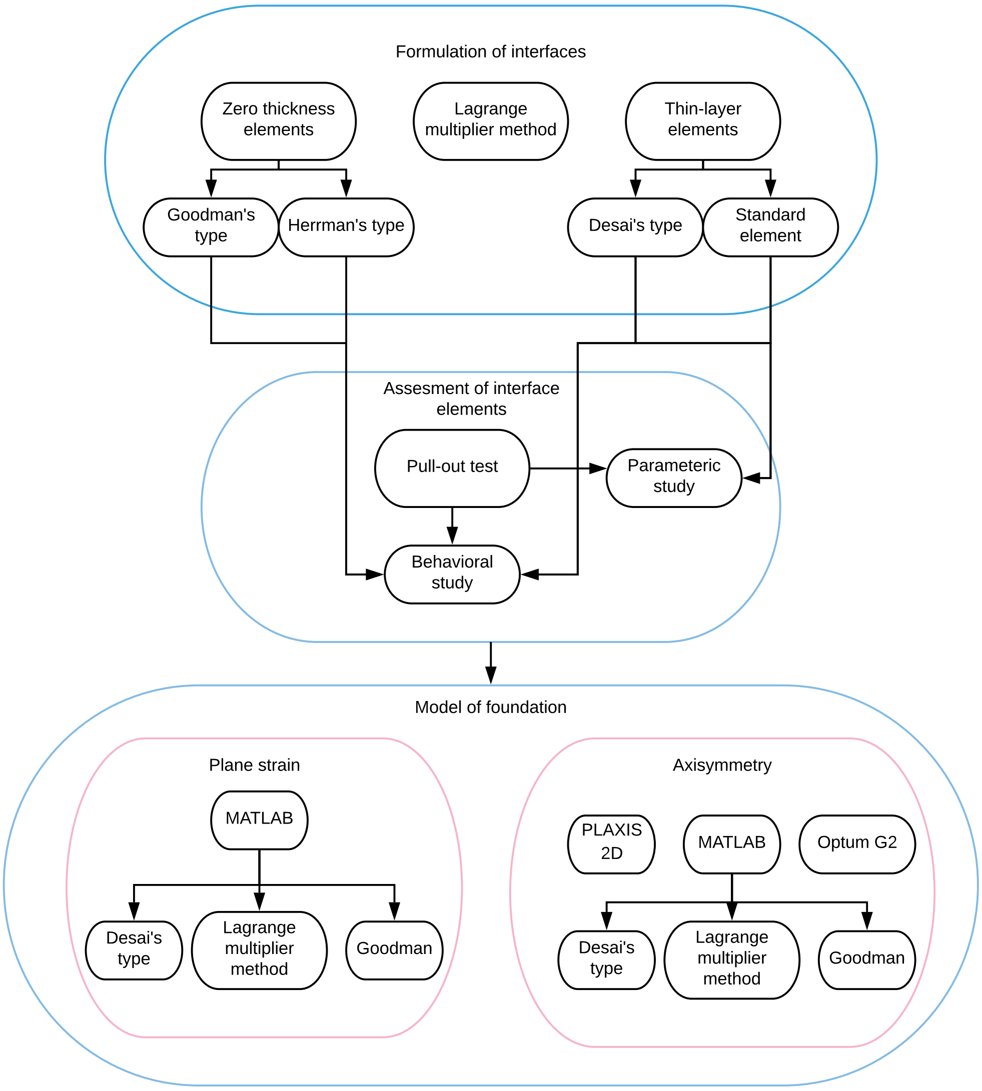

Figure 1: Flow chart of the structure of the master thesis

Table of contents

1 Introduction

Problems involving friction are of great importance in field mechanical and civil engineering. In reality, all movements involves friction and contact as for example walking, driving cars and riding a bike. In cases considering a footing or a tire that interacts with soil or a road may lead to a nonlinear problems. Due to the rapid improvement of modern computer technology, It is today possible to apply numerical tools to simulate the applications that include friction and contact mechanics. However, the most of the standard finite element software is not fully capable of solving these problems. Hence, there are still challenges to apply an efficient and strong finite element method for computational friction and contact mechanics.

Furthermore in civil engineering, a frequently considered problem is a uniform load acting on a foundation on soil. This particular problem is the main focus in this thesis. This tend to become a very complex problem that involves inelastic constitutive behavior of soil, deformations and sliding of the foundation relative to the soil domain. Due to the wide range of frictional and contact problems, the cases are today combined with either linear elastic or plastic deformation. This thesis considers Newton-Raphson scheme as a solution method for the nonlinear calculations, which is shown in Appendix E.

Many engineering problems involve contact and interaction between different materials. Such a problem include as mentioned above soil-structure interaction. In Finite Element Analysis of geotechnical structures, the interface elements are introduced to simulate that type of interaction. The interface elements should account for relative displacements along the interface to simulate accurately the deformation and physical behavior of the interacting materials. The interface element characteristics is further explained in Chapter 2, whereas the interface element behavior is accounted for in Chapter 3 and the implementation in the model in Chapter 4.

1.1 Project background

The phenomena of friction and contact problems have been investigated all the way back to the Egyptian times. The Egyptian people needed to move massive stone blocks to build the pyramids and had to overcome frictional forces. Thereafter, many distinguished scientist have investigated frictional contact problems, including Leonardo Da Vinci. He conducted an experiment that measured the friction force using blocks with the same weight but different contact area, shown in Figure 1.1 on following page. He discovered that the friction force is proportional to the weight of the blocks and independent of the contact area. By assembling this findings into a mathematical formula, the classical equation of friction is obtained in:

$$F_T = \mu N \tag{1.1}$$

F_T	Friction force
μ	Coefficient of friction
N	Normal force

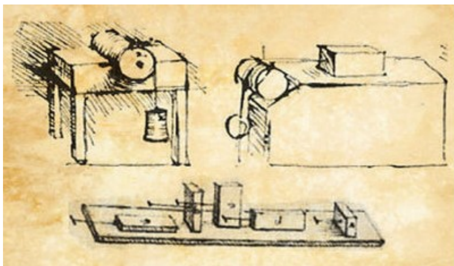

Figure 1.1: Da Vinci's experiments with blocks with different contact surfaces, Wriggers [2006].

Euler was the first mathematician who offered his thoughts on the matter in 1748. He introduced the triangular perspective that accounted for surface roughness, shown in Figure 1.2. Euler introduced the symbol μ for the friction coefficient, that is frequently used nowadays. Finally in 1785, Coulomb performed extensive experiments regarding friction.

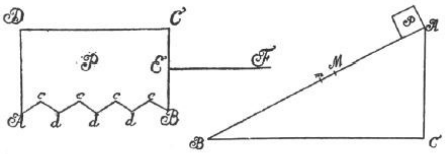

Figure 1.2: Euler's model with triangular perspective, Wriggers [2006].

He assumed the facts: normal pressure, extent of surface area, material properties and surface, ambient conditions and time dependency of friction force. In other words, Coulomb friction on how two surfaces become interlocked, is illustrated in Figure 1.3. This resulted

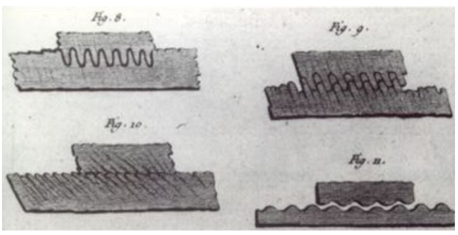

Figure 1.3: Illustration of Coulomb friction, Wriggers [2006].

in Equation (1.2) for the resistance to sliding of a body on a plane.

$$F_T = A + \frac{N}{\mu^*} \tag{1.2}$$

F_T	Friction force
μ^*	Inverse of the friction coefficient
N	Normal force
A	Cohesion

The second expression path the way for the study of interface. Nowadays, the equation is written as $F_T = A + \mu N$, and is the fundamental expression of several developments of friction and contact rules.

1.2 Literature review

The contact problems in finite element method has almost as deep history as the finite element method itself when introduced in early 1960's (Goodman [1968] Reference). The very first research done in this field is dated to 1968 by D. Ngo and A.C. Scordelis. In their research paper, they mention use of the linkage element which can be imagined as pair of bond links. The idea is further developed later by Herrman (Herrmann [1978]) known as Herrman's element in the literature. The proposed method recognize 3 different modes of interface behaviour, non-slip, slip and separation. As an alternative to the linkage elements, Goodman (Goodman [1968]), has developed joint element for simulation of interfaces in rocks. The element is originally 4-node rectangular and is designed as zero-thickness element, thus each of the pair of nodes has the same initial position. Furthermore, there has been derived higher order rectangular element on basis of Goodman's approach.

Further research was mainly focused on interface elements with very small but finite thickness. A lot development regarding thin-layer elements and constitutive relations has been done by Desai (Sharma and Desai [1992]). Unlike the mentioned zero-thickness type, the thin-layer elements are standard continuum elements with limited thickness. Therefore, this main investigation was about the influence of thickness and employing suitable constitutive relation. Another thin-layer type of the interface element was developed by Zienkiewicz(Francavilla and Zienkiewicz [1975]). Although it is conceptually similar to Desai's type using standard isoparametric shape functions and constitutive relation, the parameters suggested are anisotropic. There is also proposed ratio of stiffness parameters in the interface and in surrounding material being no more than 1:1000 in order to avoid ill-conditioning of system of equations. Slightly different method was proposed by Ghabousi et. al. and Wilson (et.al. [1973]). They suggested to use relative displacements as an independent degree of freedom. It has been shown in Wilson's (et.al. [1973]) work, that the proposed technique can increase accuracy of solution.

However, it comes with the cost of additional entries in the top of the element arrays in interface, which can increase computational time in case of more complex structures. The solution using relative displacement was further developed into 8-node biquatratic isoparametric element by Pande and Sharma. Worth to mention is their study on usability of conventional continuum isoparametric elements in interface, implying absolute degrees of freedom. Besides its simple implementation into the model as no special steps are required, the use of standard elements it not suitable according to their conclusion. The main disadvantage is the ill-conditioning of equations as the elements obey usually very high aspect ratio. This leads to another problem with inaccurate prediction of stresses, specifically the shear stress along interface.

1.3 Scope and limitations of the thesis

This thesis focuses mainly on the implementation and further assessment of interface elements used in geotechnical engineering into nonlinear finite element program of foundation on a soil domain. Based on wide literature study, the basic interface element can be divided into two groups:

- Zero thickness elements - including Herrman's type and Goodman's type
- Thin-layer elements - including Desai's type and standard continuum element

Furthermore, the material behaviour of the interface can be generally described by four modes of deformation:

- Non-slip - there is no relative displacement between nodes of connected elements and initial values for the interface normal and shear stiffness are applied. See Figure 1.4.
- Slip - the shear stress exceeds the maximum allowable value along the interface, thus relative displacement occur. See Figure 1.5.
- Separation - occurs when the interface normal stress becomes tensile and the interface which leads to that the normal and shear stiffness of the interface to become zero. It is usually related to positive relative normal displacement (as for soil materials with zero adhesion). See Figure 1.6.
- Re-bonding - where the normal stresses of the interface becomes compressed again after separation and the interface normal and shear stiffness are restored to their initial values.

The thesis is further limited to assessment of interface elements allowing the modes of slip or non-slip to be activated only. The chosen modes are controlled by shear resistance along interface, which is chosen based on failure criterion. For purpose of this thesis, the Mohr-Coulomb criterion is used which is further explained in Appendix F.

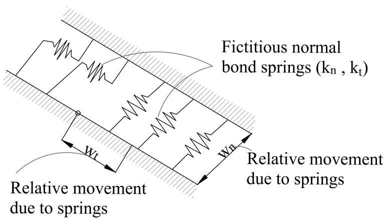

Figure 1.4: Non-slip mode

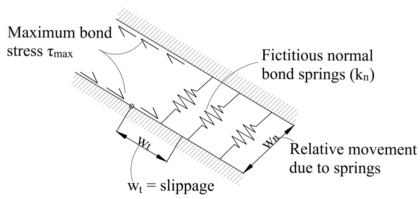

Figure 1.5: Slip mode

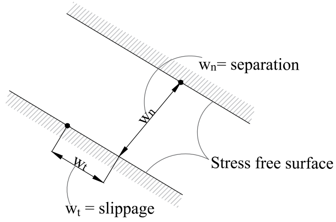

Figure 1.6: Separation

Formulation of interface elements 2

Within design of geotechnical structures, one of the biggest challenges involves the interaction between different materials and its accurate modelling in finite element software. There were developed many different approaches. The proposed solutions can be generally divided into two groups, Zero-thickness elements and Thin-layer elements described hereafter. This chapter take its basis from Herrmann [1978], Goodman [1968], Sharma and Desai [1992] and Appendix B.

One of the most important factor of accurately simulating the behavior of geological structures as a continuum is the ability to account for relative motion along the interface. For soil structures, the types of interfaces are more complex and diverse. Hence, any time soil interacts with a solid, the difference in relative stiffness between the two materials unavoidably generate an interface. The interaction along the interface is modelled by chosen element for use in a finite element analysis.

The challenge when introducing interface element is that the material of the interface is unknown and it is not desirable at this point to assign any material properties. Further analysis of the interface behavior and parameters needs to be performed before the material properties are determined.

Firstly, the elements chosen for further analysis are presented in these following sections. Further interface behavior and implementation will be accounted for in Chapters 3 and 4.

2.1 Zero-thickness element

As the name suggest, this group of elements have physically no thickness. This can be seen as a realistic way of modelling the interface as there is no extra layer of material added. Furthermore, there is no additional degrees of freedom added into the system stiffness matrix, therefore the computational time is not significantly affected. In this section two types of interfaces are defined and some of their features of each approach are presented.

2.1.1 Herrmann type

One of the first developments done regarding interface problems was a linkage element by Herrmann. The element is modelled by two link springs connecting each of the two pair of mating nodes, therefore the element has four nodes. The element recognize four modes of behaviour based on bond normal and tangential stresses along the interface. The modes are referred to as non-slip, slip, separation and re-bonding. The slip mode is activated when shear resistance is higher than the maximum allowable shear resistance corresponding to the Mohr-Coulomb yielding criteria explained further in Appendix F. In this case, the related stiffness value is set to zero and the maximum resistance is distributed as nodal load to surrounding surfaces. Similarly, when separation occurs there are both normal and tangential stress component set to zero as there is no stress transmitted between contact surfaces. When re-bonding occur, the stiffness is changed back to the original values.

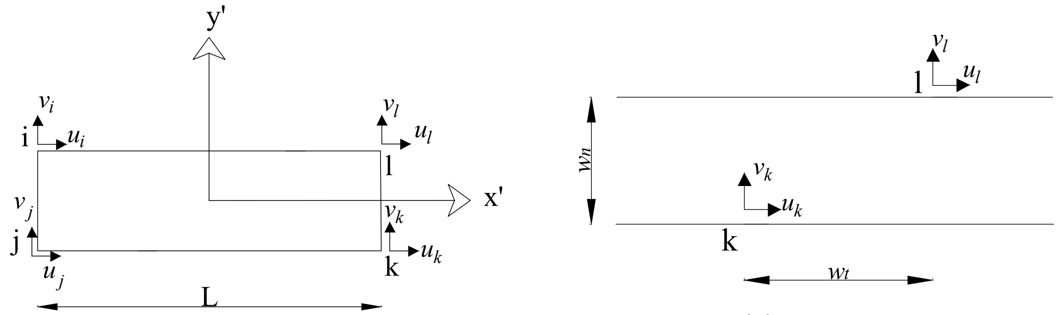

(a) Undeformed

(b) Deformed

Figure 2.1: Zero-thickness element by Herrman

Element stiffness

As mentioned above, the behaviour of element is connecting bond links through mating nodes. It can be seen in Figure 2.1b, that there are relative displacements in tangential and normal direction evaluated in each pair of nodes. The relative displacement is calculated from absolute displacements in each node as shown below

$$\begin{Bmatrix} w_t \\ w_n \end{Bmatrix} = \begin{Bmatrix} u_l - u_k \\ v_l - v_k \end{Bmatrix} = \begin{bmatrix} -1 & 0 & 1 & 0 \\ 0 & -1 & 0 & 1 \end{bmatrix} \begin{Bmatrix} u_k \\ v_k \\ u_l \\ v_l \end{Bmatrix} \tag{2.1}$$

w_t	Relative tangential displacements
w_n	Relative normal displacements
u_k, v_k, u_l, v_l	Displacements in local coordinate system (x', y')

This relationship is used for calculation of the nodal forces, which shown in:

$$f_{ix} = -f_{kx} = P_t\, w_t\, \frac{L}{2} \tag{2.2}$$

$$f_{iy} = -f_{ky} = P_n\, w_n\, \frac{L}{2} \tag{2.3}$$

L	Length of the interface
P_t	Tangential link spring stiffness per unit length
P_n	Normal link spring stiffness per unit length
f_{ij}	Nodal forces where $i = (k, l)$ and $j = (x, y)$

Introducing the normal and tangential link springs, also referred to as penalty numbers, Equations (2.2) and (2.3) can be written in matrix form yielding:

$$\frac{L}{2}\begin{bmatrix} -P_t & 0 \\ 0 & -P_n \\ P_t & 0 \\ 0 & P_n \end{bmatrix} \begin{Bmatrix} w_t \\ w_n \end{Bmatrix} = \begin{Bmatrix} f_{kx} \\ f_{ky} \\ f_{lx} \\ f_{ly} \end{Bmatrix} \tag{2.4}$$

Substituting the relative displacement by nodal displacements, the finite element equations are introduced as:

$$\frac{L}{2}\begin{bmatrix} P_t & 0 & P_t & 0 \\ 0 & P_n & 0 & -P_n \\ -P_t & 0 & P_t & 0 \\ 0 & -P_n & 0 & P_n \end{bmatrix} \begin{Bmatrix} u_k \\ v_k \\ u_l \\ v_l \end{Bmatrix} = \begin{Bmatrix} f_{kx} \\ f_{ky} \\ f_{lx} \\ f_{ly} \end{Bmatrix} \tag{2.5}$$

The interface behavior is modeled through fictitious springs at each of the two pairs of mating nodes and the nodal forces are related to the relative displacements through the link spring stiffnesses. Hence, the element stiffness equation can be written as:

$$[K]\{u\} = \{f\} \tag{2.6}$$

where the stiffness matrix $[K]$ only contains the tangential P_t and normal P_n link spring stiffness, $\{u\}$ as the nodal displacement vector and $\{f\}$ as the vector of nodal forces.

Element Stresses

The stresses, by definition forces per unit length, are evaluated for each half of the element as the two links behave independently. Which leads to the definition of the shear stress τ_s and normal stress σ_n shown in:

$$\tau_s = \frac{f_{ix}}{L/2} \tag{2.7}$$

$$\sigma_n = \frac{f_{iy}}{L/2} \tag{2.8}$$

Which can be rewritten as the following equations, by using Equation (2.6):

$$f_{ix} = P_t\,\frac{L}{2}\,(u_i - u_j) \tag{2.9}$$

$$f_{iy} = P_n\,\frac{L}{2}\,(v_i - v_j) \tag{2.10}$$

Yielding the expression for shear and normal stresses as seen in:

$$\tau_s = P_t\,(u_i - u_j) \tag{2.11}$$

$$\sigma_n = P_n\,(v_i - v_j) \tag{2.12}$$

The expressions for the link stresses on the other side are identical except for the denoted nodal letters.

Single element behavior

To demonstrate element behavior, one element is shown below in Figures 2.2 and 2.3. The element is loaded in node 4 by unit force in the positive horizontal direction. Whereas the element is fixed on the bottom between node 1 and 2. It can be seen that other nodes stays unaffected, as a consequence to independent behaviour of each link.

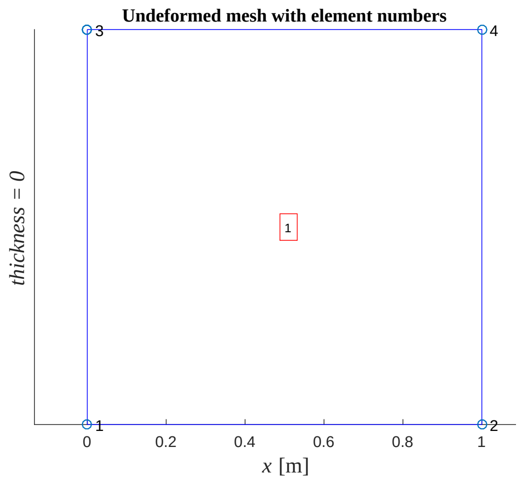

Figure 2.2: Undeformed mesh

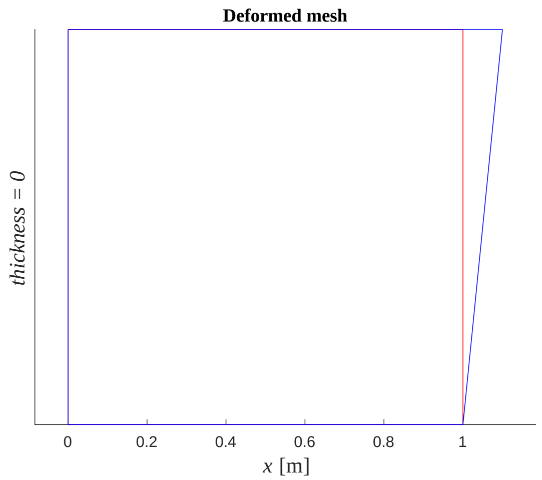

Figure 2.3: Deformed mesh

2.1.2 Goodman type

Goodman has developed a 4-node rectangular interface element for rock joints. The element structure and its implementation is fairly straight forward, which makes it the widely used. However, it proposes some kinematic inconsistencies, which are pinpointed in this section and solution to the problem is presented. The recognition of the four different behaviour modes remains the same also for Goodman's element. Therefore, no-slip, slip, separation and re-bonding can be simulated by changing stiffness values. A 4-noded zero thickness interface element is illustrated in Figure 2.4.

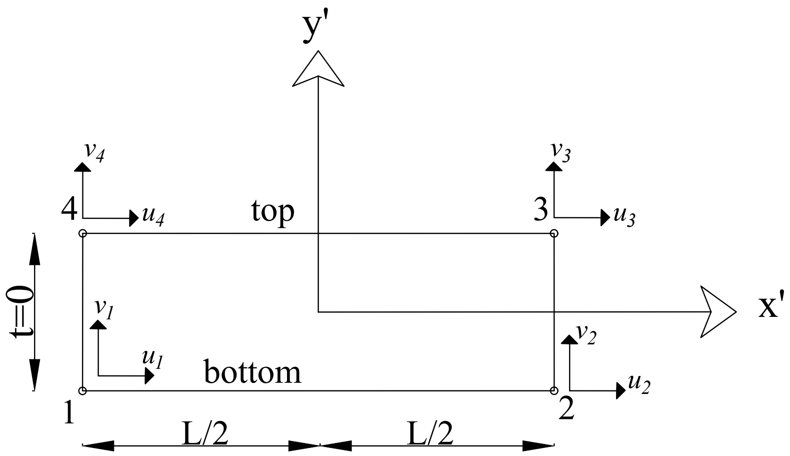

Figure 2.4: 4-noded Goodman zero thickness interface element

Element stiffness

Unlike for Herrman's type, the nodal displacement can be determined by using linear shape functions as shown in:

$$\begin{Bmatrix} u_b \\ v_b \end{Bmatrix} = \begin{bmatrix} N_1 & 0 & N_2 & 0 & 0 & 0 & 0 & 0 \\ 0 & N_1 & 0 & N_2 & 0 & 0 & 0 & 0 \end{bmatrix} \begin{Bmatrix} u \end{Bmatrix} \tag{2.13}$$

$$\begin{Bmatrix} u_t \\ v_t \end{Bmatrix} = \begin{bmatrix} 0 & 0 & 0 & 0 & N_2 & 0 & N_1 & 0 \\ 0 & 0 & 0 & 0 & 0 & N_2 & 0 & N_1 \end{bmatrix} \begin{Bmatrix} u \end{Bmatrix} \tag{2.14}$$

The calculation follows rather standard Finite Element procedure of obtaining the stiffness matrix. First of all, the relative displacement vector is obtained as in:

$$\begin{Bmatrix} w \end{Bmatrix} = \begin{Bmatrix} w_s \\ w_n \end{Bmatrix} = \begin{Bmatrix} u_t - u_b \\ v_t - v_b \end{Bmatrix} \tag{2.15}$$

w_s	Relative tangential displacement
w_n	Relative normal displacement
u_t, v_t, u_b, v_b	Displacements along x' and y' where $_t =$ "top", $_b =$ "bottom"

Substituting (2.13) and (2.14) into (2.15), we can express the relative displacement as in:

$$\{w\} = [B]\,\{u\} \tag{2.16}$$

where

$$\begin{bmatrix} B \end{bmatrix} = \begin{bmatrix} -N_1 & 0 & -N_2 & 0 & N_2 & 0 & N_1 & 0 \\ 0 & -N_1 & 0 & -N_2 & 0 & N_2 & 0 & N_1 \end{bmatrix} \tag{2.17}$$

In the next step, the stress-strain relationship needs to be established. As in the previous case, the relative displacement is considered as general strain, therefore the stiffness matrix can be obtain as:

$$\begin{bmatrix} K \end{bmatrix}^e = \int \begin{bmatrix} B \end{bmatrix}^T \begin{bmatrix} D \end{bmatrix} \begin{bmatrix} B \end{bmatrix} \,\mathrm{dx} \tag{2.18}$$

It can be obtain by solving above stated integral and the resulting stiffness matrix is expressed as:

$$\begin{bmatrix} K \end{bmatrix}^e = \frac{L}{6} \begin{bmatrix} 2k_s & 0 & k_s & 0 & -k_s & 0 & -2k_s & 0 \\ 0 & 2k_n & 0 & k_n & 0 & -k_n & 0 & -2k_n \\ k_s & 0 & 2k_s & 0 & -2k_s & 0 & -k_s & 0 \\ 0 & -k_n & 0 & 2k_n & 0 & -2k_n & 0 & -k_n \\ -k_s & 0 & -2k_s & 0 & 2k_s & 0 & k_s & 0 \\ 0 & -k_n & 0 & -2k_n & 0 & 2k_n & 0 & k_n \\ -2k_s & 0 & -k_s & 0 & k_s & 0 & 2k_s & 0 \\ 0 & -2k_n & 0 & -k_n & 0 & k_n & 0 & 2k_n \end{bmatrix} \tag{2.19}$$

$$u_3 = \frac{4F}{L\,k_s} \tag{2.20}$$

$$u_4 = \frac{-2F}{L\,k_s} \tag{2.21}$$

Single element behavior

The so called stresses (force per unit length) are evaluated in element center and as in Herrmann element, the relative displacement can be used for calculation. From the single element test performed under same set up as for Herrmann element, therefore loaded in horizontal direction in node 4, there is obvious kinematic inconsistency between top nodes, see Figure 2.6. This is justified in Equations (2.20) and (2.21), as the horizontal displacement are opposite to each other. This is due to the stiffness formulation and not result of ill-conditioning. Thus, the element is not further used in analysis. However, the values of stresses yields values as expected.

The solution to this problem was developed in Li and Kaliakin [1993] and involves merging two regular Goodman elements into one described in following section.

2.1.3 Improved 4-node and 6-node zero thickness element

The geometric characteristics of this element is the same as for the element in Section 2.1.2. However, the improved Goodman element have a different stiffness matrix given by

$$[K] = \frac{L}{48}\begin{bmatrix} 7k_s & 0 & -k_s & 0 & k_s & 0 & 7k_s & 0 \\ 0 & 7k_n & 0 & -k_n & 0 & k_n & 0 & -7k_n \\ -k_s & 0 & 7k_s & 0 & -7k_s & 0 & -k_s & 0 \\ 0 & -k_n & 0 & 7k_n & 0 & -7k_n & 0 & k_n \\ k_s & 0 & -7k_s & 0 & 7k_s & 0 & -k_s & 0 \\ 0 & k_n & 0 & -7k_n & 0 & 7k_n & 0 & -k_n \\ -7k_s & 0 & k_s & 0 & -k_s & 0 & 7k_s & 0 \\ 0 & -7k_n & 0 & k_n & 0 & -k_n & 0 & 7k_n \end{bmatrix} \tag{2.22}$$

The element stiffness matrix is obtained by merging two identical elements together as shown in Figure 2.5 for 4-noded case. The middle nodes 5 and 6 are then condense out yielding the stiffness matrix as shown in 2.22. In the similar way the stiffness matrix for 6-noded element is derived as

$$[K] = \frac{L}{24}\begin{bmatrix} 3k_s & 0 & -k_s & 0 & 0 & 0 & 0 & 0 & k_s & 0 & -3k_s & 0 \\ 0 & 3k_n & 0 & -k_n & 0 & 0 & 0 & 0 & 0 & k_n & 0 & -3k_n \\ -k_s & 0 & 6k_s & 0 & -k_s & 0 & k_s & 0 & -6k_s & 0 & k_s & 0 \\ 0 & -k_n & 0 & 6k_n & 0 & -k_n & 0 & k_n & 0 & -6k_n & 0 & k_n \\ 0 & 0 & -k_s & 0 & 3k_s & 0 & -3k_s & 0 & k_s & 0 & 0 & 0 \\ 0 & 0 & 0 & -k_n & 0 & 3k_n & 0 & -3k_n & 0 & k_n & 0 & 0 \\ 0 & 0 & k_s & 0 & -3k_s & 0 & 3k_s & 0 & -k_s & 0 & 0 & 0 \\ 0 & 0 & 0 & k_n & 0 & -3k_n & 0 & 3k_n & 0 & -k_n & 0 & 0 \\ k_s & 0 & -6k_s & 0 & k_s & 0 & -k_s & 0 & 6k_s & 0 & -k_s & 0 \\ 0 & k_n & 0 & -6k_n & 0 & k_n & 0 & -k_n & 0 & 6k_n & 0 & -k_n \\ -3k_s & 0 & k_s & 0 & 0 & 0 & 0 & 0 & -k_s & 0 & 3k_s & 0 \\ 0 & -3k_n & 0 & k_n & 0 & 0 & 0 & 0 & 0 & -k_n & 0 & 3k_n \end{bmatrix} \tag{2.23}$$

The stiffness matrix is conducted by that the improved element is a merge of two identical elements as shown in Figure 2.5 for 4-noded type which is used as an example in single element test herafter. The nodes 5 and 6 that are connecting the elements together are condensed out and its contribution is redistributed to the remaining corner nodes.

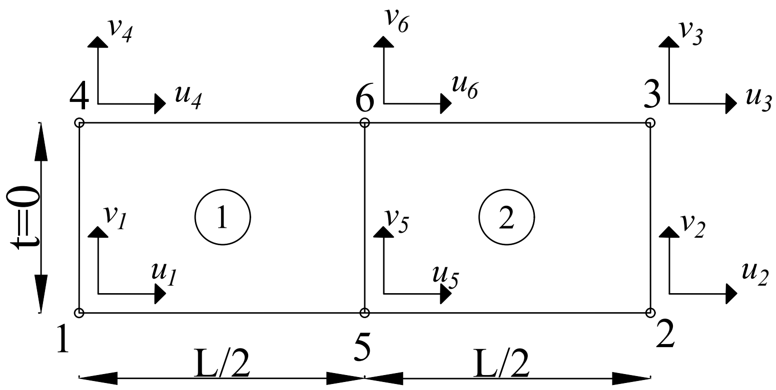

Figure 2.5: 4-noded improved Goodman zero thickness interface element

Single element behaviour

As can be seen from the single element test, see Figure 2.7), the displacement looks as expected with expected stress values.

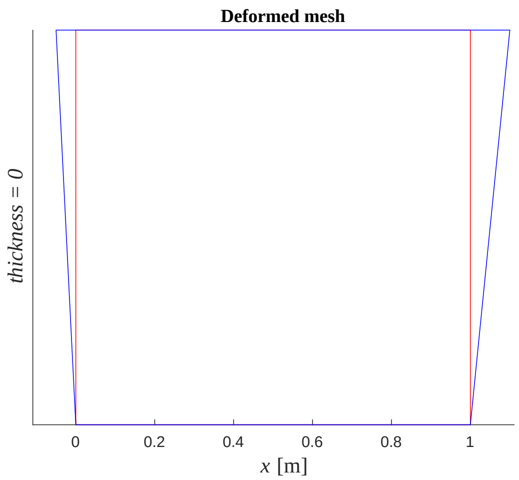

Figure 2.6: Original Goodman element

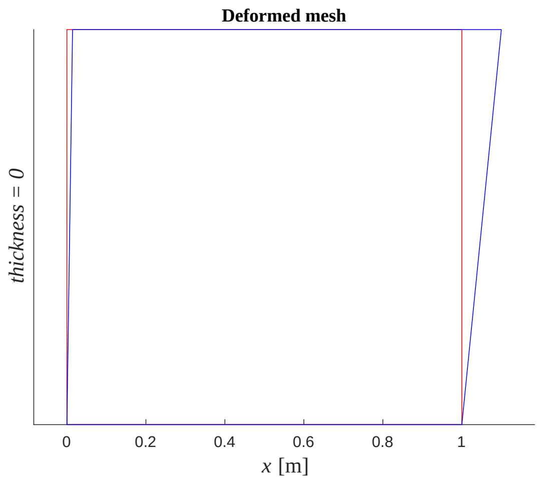

Figure 2.7: Improved 4-noded Goodman element

2.1.4 Constitutive model

Goodman's type

Due to the fact that it is assumed an interface element thickness of zero, the in-plane strains $\varepsilon_x = 0$ is negligible and thus also the in-plane stresses is equal to zero, $\sigma_x = 0$, the stress and strain vector are left with two parameters. As mentioned in Section 2.1.2, the vector containing relative displacements, $\{w\}$, is considered as general strains.

The constitutive model for the original interface element of Goodman can be presented in a general form as:

$$\begin{Bmatrix} \tau_s \\ \sigma_n \end{Bmatrix} = [D]\,\{w\} = \begin{bmatrix} k_s & 0 \\ 0 & k_n \end{bmatrix} \begin{Bmatrix} w_s \\ w_n \end{Bmatrix} \tag{2.24}$$

τ_s	Tangential stress
σ_n	Normal stresses
k_s	Tangential stiffness of the interface
k_n	Normal stiffness of the interface

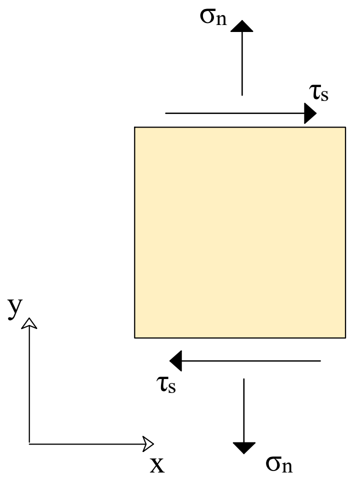

Figure 2.8: Goodman interface stresses

These interface stresses are related to the relative displacements by the interface constitutive relation which consists of one tangential stiffness k_s and one normal stiffness k_n in an uncoupled form. In the original constitutive relationship of the interface, there are non off-diagonal terms. This means that the shear and normal deformations are independent of each other. Furthermore it also implies that there is no dilatancy, or volume change if subjected to shear deformations.

Herrmann's type

Identical to the constitutive relations concerning the Goodmann's type, the relative displacements of the Herrmann element are also considered as general strain. The stresses are calculated from Equations (2.11) and (2.12), which leads to the representation of the the constitutive relation where the stresses are connected to the relative displacements through the link spring stiffnesses.

2.2 Thin layer interface element

Thin elements are mainly standard continuum elements of a small but finite thickness. The principal subjects to developing thin layer elements include suitable constitutive laws for the interface, the correct thickness of the thin elements and the integration of the respective modes of deformation. In this thesis the Desai type is taken under consideration.

2.2.1 Constitutive model

The case studied in this report concerning the thin layer interface elements, are represented by a 6-noded element.

As mentioned in Section 1.3 only modes slip and non-slip are considered in this report (see Figures 1.5 and 1.4). During the slip or no-slip mode, there is no relative motion under shear stress, τ, and normal stress, σ_n, is compressive. elastoplastic incremental constitutive matrix is obtained just as in the case of the surrounding soil elements, shown in:

$$\{d\sigma\} = [C]\{d\varepsilon\} \tag{2.25}$$

$\{d\sigma\}$	Vector of incremental stress
$\{d\varepsilon\}$	Vector of incremental strain
C	Constitutive matrix

In Equation (2.25) all the stresses and strains are included and the compressive stresses are considered positive. However, generally it is not possible to find properties of the thin layer from testing with solid specimens that simulate the material at the interface, but approximations can be made. In this case, with non-slip assumed, the properties are derived from shear at the interfaces between two bodies, presented as:

$$k_s = \frac{d\tau}{du_r} \tag{2.26}$$

$$k_n = \frac{d\sigma_n}{dv_r} \tag{2.27}$$

τ	Shear stress
u_r	Relative shear displacement
σ_n	Normal stresses
v_r	Relative normal displacement
k_s	Shear stiffness of the interface
k_n	Normal stiffness of the interface

The formulation of the thin layer element has previous been developed as a continuum finite element, where the constitutive response has been defined differently than the neighboring elements.

The layout of the thin layer interface element with respect to the global coordinate system of the entire structure is essential as the k_s and k_n in Equations (2.26) and (2.27) are local properties of the interface. Hence, the formulation is first presented with reference to the local coordinate system of the interface, followed by a presentation with respect to the global coordinate system of the structure. As the thickness approaches zero, the in-plain stress and strain become negligible compared to normal- and shear stress and strain components. As a result of this, the interface stresses and strains can be expressed in terms of the normal and shear components only.

Considering a 4-noded interface element shown in Figure 2.9, u' and v' represents displacements in the local coordinate system (x', y') and u and v are displacements with respect to the global coordinate system (x, y). The interface is positioned with an angle θ and a thickness t.

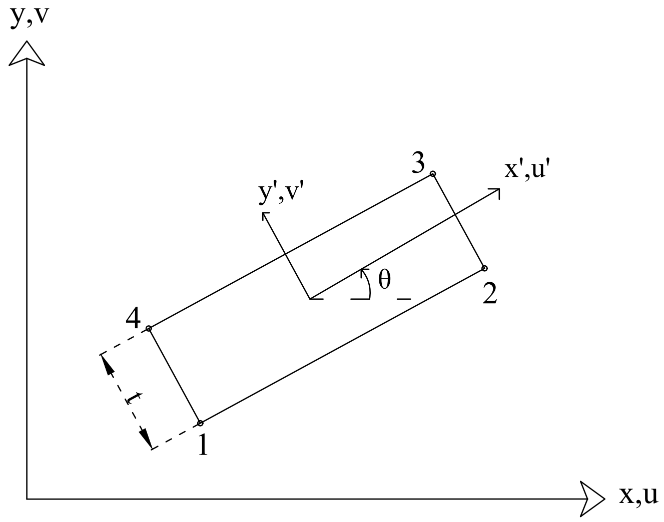

Figure 2.9: Four-noded interface element.

Formulation of the local coordinate system

Displacements, u' and v', at any point within the element are given by:

$$\begin{Bmatrix} u' \\ v' \end{Bmatrix} = \begin{bmatrix} N_1 & 0 & N_2 & 0 & N_3 & 0 & N_4 & 0 \\ 0 & N_1 & 0 & N_2 & 0 & N_3 & 0 & N_4 \end{bmatrix} \left\{ q' \right\} \tag{2.28}$$

or it can be expressed:

$$\{u'\} = [N]\{q'\}$$

$[N]$	Strain interpolation functions
$\{q'\}$	Vector of nodal displacements - $\{q'\} = (u'_1 v'_1 u'_2 v'_2 u'_3 v'_3 u'_4 v'_4)^T$

Strain-displacements relationship
For a two-dimensional case, the strain-displacement relationship is presented in:

$$\left\{ \varepsilon' \right\} = \begin{Bmatrix} \varepsilon'_x \\ \varepsilon'_y \\ \gamma'_{xy} \end{Bmatrix} = \begin{Bmatrix} \frac{\partial u'}{\partial x'} \\ \frac{\partial v'}{\partial y'} \\ \frac{\partial u'}{\partial y'} + \frac{\partial v'}{\partial x'} \end{Bmatrix} = [B]\{q^T\} \tag{2.29}$$

ε'_x, ε'_y and γ'_{yx}	Strain components
$[B]$	Strain interpolation matrix

In plane stress and strain components
The three stress components relevant to the strains in Equation (2.29) are σ'_x, σ'_y and τ'_{xy}. Furthermore, where σ'_x represents the inplane stress, σ'_y the stress normal to the interface and τ'_{xy} the shear stress of the interface, shown in Figure 2.10.

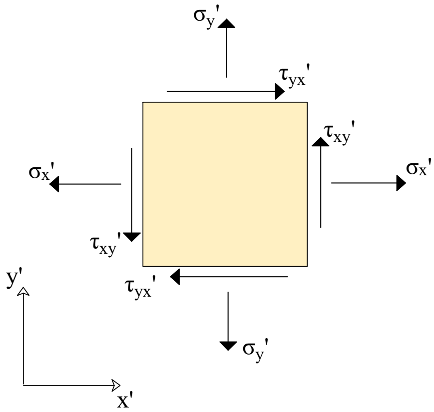

Figure 2.10: Desai interface stresses

Formulation of the global coordinate system

In the considered case, the inclination angle $\theta = 0$, thus the formulation of the coordinate system is derived as global. With respect to the global coordinate system $(x, y), u$ and v are given by:

$$\begin{Bmatrix} u \\ v \end{Bmatrix} = \begin{bmatrix} N_1 & 0 & N_2 & 0 & N_3 & 0 & N_4 & 0 \\ 0 & N_1 & 0 & N_2 & 0 & N_3 & 0 & N_4 \end{bmatrix} \begin{Bmatrix} q \end{Bmatrix} \tag{2.30}$$

or it can be expressed:

$$\{u\} = [N] \{q\}$$

$[N_i]$	Strain interpolation functions
$\{q\}$	Displacements of the nodes in x- and y-direction - $\{q^T\} = (u_1 v_1 u_2 v_2 u_3 v_3 u_4 v_4)$

Strain-displacement relationship

The strains are related to the displacements as shown in respectively:

$$\begin{Bmatrix} \varepsilon \end{Bmatrix} = \begin{Bmatrix} \varepsilon_x \\ \varepsilon_y \\ \gamma_{xy} \end{Bmatrix} = \begin{Bmatrix} \frac{\partial u}{\partial x} \\ \frac{\partial v}{\partial y} \\ \frac{\partial u}{\partial y} + \frac{\partial v}{\partial x} \end{Bmatrix} \tag{2.31}$$

or it can be expressed:

$$\{\varepsilon\} = [B] \{q\}$$

$\{\varepsilon_i\}$	Strain components with reference to the global coordinate system
$[B]$	Strain interpolation matrix

Stress-strain relationship

In order to relate the stresses in global coordinate system to the global strains. The normal

ε_n and shear γ strains in the local coordinate system are related to the global strains ε_x, ε_y and γ_{xy} as shown in:

$$\begin{Bmatrix} \varepsilon_n \\ \gamma \end{Bmatrix} = \begin{bmatrix} s^2 & c^2 & -c\,s \\ -2\,c\,s & 2\,c\,s & c^2 - s^2 \end{bmatrix} \begin{Bmatrix} \varepsilon_x \\ \varepsilon_y \\ \gamma_{xy} \end{Bmatrix} \tag{2.32}$$

or:

$$\{\varepsilon'\} = [T]\,\{\varepsilon\}$$

$[T]$	Transformation matrix
s	$\sin\theta$
c	$\cos\theta$
θ	Inclination of the interface as illustrated in Figure 2.9

Equivalently, the local and global stresses are related through the same relationship shown in:

$$\begin{Bmatrix} \sigma_n \\ \tau \end{Bmatrix} = \begin{bmatrix} s^2 & c^2 & -c\,s \\ -2\,c\,s & 2\,c\,s & c^2 - s^2 \end{bmatrix} \begin{Bmatrix} \sigma_x \\ \sigma_y \\ \tau_{xy} \end{Bmatrix} \tag{2.33}$$

or:

$$\{\sigma'\} = [T]\,\{\sigma\}$$

By using (2.31) and (2.33), in addition to setting the local and global strain relationships equal to each other, the stress-strain relation in the global coordinate system is obtained as:

$$\{d\,\sigma\} = [T^T]\,[\bar{C}]\,\{d\varepsilon\} = [C]\,\{d\varepsilon\} \tag{2.34}$$

Hence, the local constitutive matrix $[\bar{C}]$, gets transformed into the global constitutive matrix $[C]$ by the connection shown in Equation (2.34). The matrix $[C]$ can be both elastic ($[C^e]$) or elastoplastic ($[C^{ep}]$), depending on whether the system or the interface are considered elastic or elastoplastic.

Equation (2.34) is used to obtain the element stiffness matrix in the global coordinate system as:

$$[k] = \int_v [B^T]\,[C]\,[B]\,\mathrm{dV} \tag{2.35}$$

v	Element volume

The constitutive model

As mentioned before, the interface behavior is influenced by several factors, such as physical and geometrical properties of the surrounding material, material behavior and the thickness of the thin layer element. If the thickness is too large, the thin layer interface element will act like a normal solid element. Hence, the choice of thickness is essential to the modelling of thin layer elements. The assessment of the element thickness is carried out in a parametric study explained in detail i Section 3.1. As mentioned briefly in Section 1.2, Desai has previously performed a such a parametric study where he obtained satisfactory model for the interface behavior. Thus with a width ratio, $\frac{t}{B}$, in the range of 0,01 to 0,1.

Elastic constitutive model
During an analysis where the material behaves elastically to obtain a satisfactory value of the thickness t, an parametric study including finite element analysis has to be performed. This includes the parameters of ratio $\frac{t}{B}$, relative magnitudes of elastic properties of neighboring elements such as elastic modulus and Poisson ratio (E_N and ν_N) and the normal and the shear stiffness of the interface (k_n and k_s).

Assuming plain strain, the elastic constitutive matrix $[\bar{C}^e]$ yields:

$$[\bar{C}^e] = \frac{E}{(1+\nu)(1-2\nu)} \begin{bmatrix} 1-\nu & \nu & 0 \\ \nu & 1-\nu & 0 \\ 0 & 0 & \frac{1-2\nu}{2} \end{bmatrix} \tag{2.36}$$

where E and ν are the elastic modulus and the Poisson's ratio of the interface respectively. E and ν of the interface is to be derived from:

$$E \cong k_n\, t \tag{2.37}$$

$$G \cong k_s\, t \tag{2.38}$$

where G represents the shear modulus. The Poisson's ratio is found by the relations in:

$$\nu = \frac{E}{2\,G} - 1 = \frac{k_n}{k_s} - 1 \tag{2.39}$$

The case studied in this report concerning the thin layer element is the interfaces represented by 4 nodes with a formulation presented with elastic constitutive matrix. Due to the fact that the interface is horizontal, the inclination angle $\theta = 0$. So by substituting $\theta = 0$ into the transformation matrices $[T]$ and $[T']$ yields:

$$[C^e] = \begin{bmatrix} k_n\, t & 0 \\ 0 & k_s\, t \end{bmatrix} \tag{2.40}$$

2.3 Lagrange multiplier method

The Lagrange multiplier method differ from former interface approaches as it is not an element and its implementation requires additional computation.

2.3.1 Physical interpretation

The Lagrange method can be presented in many different mathematical approaches. The method is presented by using the simple six element bar shown in Figure 2.11

The constraints $u_2 = u_6$ are under consideration. During the Lagrange multiplier method, a rigid fictional bar is considered to connect the chosen degrees of freedom. The rigid bar may be removed if it is replaced by an appropriate reaction force pair, $-\lambda, \lambda$. These is called *constraint forces*. The constraint forces are inserted into the original stiffness equation (B.3), which yields:

$$\begin{bmatrix} K_{11} & K_{12} & 0 & 0 & 0 & 0 & 0 \\ K_{12} & K_{22} & K_{23} & 0 & 0 & 0 & 0 \\ 0 & K_{23} & K_{33} & K_{34} & 0 & 0 & 0 \\ 0 & 0 & K_{34} & K_{44} & K_{45} & 0 & 0 \\ 0 & 0 & 0 & K_{45} & K_{55} & K_{56} & 0 \\ 0 & 0 & 0 & 0 & K_{56} & K_{66} & K_{67} \\ 0 & 0 & 0 & 0 & 0 & K_{67} & K_{77} \end{bmatrix} \begin{Bmatrix} u_1 \\ u_2 \\ u_3 \\ u_4 \\ u_5 \\ u_6 \\ u_7 \end{Bmatrix} = \begin{Bmatrix} f_1 \\ f_2 - \lambda \\ f_3 \\ f_4 \\ f_5 \\ f_6 + \lambda \\ f_7 \end{Bmatrix} \tag{2.41}$$

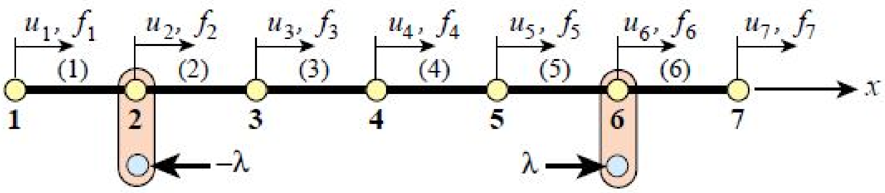

Figure 2.11: Physical interpretation of the Lagrange multiplier method to enforce the Multi freedom constraints, $u_2 = u_6$, Felippa [2004]

The λ is called the *Lagrange multiplier*. Due to that λ is unknown, it is moved to the left-hand-side, inserting it into the displacement vector. However, now there is 7 equations and 8 unknown displacements. To make the system solvable, the constraint condition $u_2 - u_6 = 0$ is inserted as Equation (2.42):

$$\begin{bmatrix} K_{11} & K_{12} & 0 & 0 & 0 & 0 & 0 & 0 \\ K_{12} & K_{22} & K_{23} & 0 & 0 & 0 & 0 & 1 \\ 0 & K_{23} & K_{33} & K_{34} & 0 & 0 & 0 & 0 \\ 0 & 0 & K_{34} & K_{44} & K_{45} & 0 & 0 & 0 \\ 0 & 0 & 0 & K_{45} & K_{55} & K_{56} & 0 & 0 \\ 0 & 0 & 0 & 0 & K_{56} & K_{66} & K_{67} & -1 \\ 0 & 0 & 0 & 0 & 0 & K_{67} & K_{77} & 0 \\ 0 & 1 & 0 & 0 & 0 & -1 & 0 & 0 \end{bmatrix} \begin{Bmatrix} u_1 \\ u_2 \\ u_3 \\ u_4 \\ u_5 \\ u_6 \\ u_7 \\ \lambda \end{Bmatrix} = \begin{Bmatrix} f_1 \\ f_2 \\ f_3 \\ f_4 \\ f_5 \\ f_6 \\ f_7 \\ 0 \end{Bmatrix} \tag{2.42}$$

The system in Equation (2.42) is called multiplier augmented system. Solving this system yield the wanted solutions for the degrees of freedom, as well as characterizing the constraint forces through λ.

2.3.2 Lagrange Multipliers for General Multi freedom constraints

The general procedure will be stated first as a recipe. Suppose that the system that is under consideration is a structure subjected to three MFCs, presented in Equation (2.43):

$$u_2 - u_6 = 0 \qquad 5u_2 - 8\,u_7 = 3 \qquad 3\,u_3 + u_5 - 4\,u_6 = 1 \tag{2.43}$$

1. Add these MFCs as the eighth, ninth and tenth equation, shown in Equation (2.44):

$$\begin{bmatrix} K_{11} & K_{12} & 0 & 0 & 0 & 0 & 0 \\ K_{12} & K_{22} & K_{23} & 0 & 0 & 0 & 0 \\ 0 & K_{23} & K_{33} & K_{34} & 0 & 0 & 0 \\ 0 & 0 & K_{34} & K_{44} & K_{45} & 0 & 0 \\ 0 & 0 & 0 & K_{45} & K_{55} & K_{56} & 0 \\ 0 & 0 & 0 & 0 & K_{56} & K_{66} & K_{67} \\ 0 & 0 & 0 & 0 & 0 & K_{67} & K_{77} \\ 0 & 1 & 0 & 0 & 0 & -1 & 0 \\ 0 & 5 & 0 & 0 & 0 & 0 & -8 \\ 0 & 0 & 3 & 0 & 1 & -4 & 0 \end{bmatrix} \begin{Bmatrix} u_1 \\ u_2 \\ u_3 \\ u_4 \\ u_5 \\ u_6 \\ u_7 \end{Bmatrix} = \begin{Bmatrix} f_1 \\ f_2 \\ f_3 \\ f_4 \\ f_5 \\ f_6 \\ f_7 \\ 0 \\ 3 \\ 1 \end{Bmatrix} \tag{2.44}$$

2. Three Lagrange multipliers are needed for three MCFs, λ_1, λ_2 and λ_3. Add the unknown multipliers to the nodal displacement vector.
3. The coefficient matrix is symmetrized by adding three columns that are the transpose of the 3 last rows in Equation (2.44).
4. A 3×3 zero matrix is inserted to the bottom right corner, yielding the solution in Equation (2.45):

$$\begin{bmatrix} K_{11} & K_{12} & 0 & 0 & 0 & 0 & 0 & 0 & 0 & 0 \\ K_{12} & K_{22} & K_{23} & 0 & 0 & 0 & 0 & 1 & 5 & 0 \\ 0 & K_{23} & K_{33} & K_{34} & 0 & 0 & 0 & 0 & 0 & 3 \\ 0 & 0 & K_{34} & K_{44} & K_{45} & 0 & 0 & 0 & 0 & 0 \\ 0 & 0 & 0 & K_{45} & K_{55} & K_{56} & 0 & 0 & 0 & 1 \\ 0 & 0 & 0 & 0 & K_{56} & K_{66} & K_{67} & -1 & 0 & -4 \\ 0 & 0 & 0 & 0 & 0 & K_{67} & K_{77} & 0 & -8 & 0 \\ 0 & 1 & 0 & 0 & 0 & -1 & 0 & 0 & 0 & 0 \\ 0 & 5 & 0 & 0 & 0 & 0 & -8 & 0 & 0 & 0 \\ 0 & 0 & 3 & 0 & 1 & -4 & 0 & 0 & 0 & 0 \end{bmatrix} \begin{Bmatrix} u_1 \\ u_2 \\ u_3 \\ u_4 \\ u_5 \\ u_6 \\ u_7 \\ \lambda_1 \\ \lambda_2 \\ \lambda_3 \end{Bmatrix} = \begin{Bmatrix} f_1 \\ f_2 \\ f_3 \\ f_4 \\ f_5 \\ f_6 \\ f_7 \\ 0 \\ 3 \\ 1 \end{Bmatrix} \tag{2.45}$$

2.3.3 The Theory Behind Lagrange Multipliers

The recipe presented in Equation (2.45), is based on well known mathematical approaches. Using the matrix notation introduced from Equation (B.3), the potential energy of the unconstrained finite element model is allowed to be represented as $\Pi = \frac{1}{2}\, u^T\, K\, u - u^T\, f$. To introduce the constraints, the Lagrangian multipliers needs to be collected in a vector λ in order to form the Lagrangian equation presented hereafter.

$$L(u, \lambda) = \Pi + \lambda^T\, (A\, u - b) = \frac{1}{2}\, u^T\, K\, u - u^T\, f + \lambda^T\, (A\, u - b) \tag{2.46}$$

Rewriting Equation (2.46) into matrix form yields Equation (2.47):

$$\begin{bmatrix} K & A^T \\ A & 0 \end{bmatrix} \begin{Bmatrix} u \\ \lambda \end{Bmatrix} = \begin{Bmatrix} f \\ b \end{Bmatrix} \tag{2.47}$$

The master stiffness matrix K in Equation (2.47) is conditioned to border with A and A^T. Solving this system yields u and λ. The last mentioned can be interpreted as forces of constraints in the following order: a removed constraint can be replaced by a system of forces characterized by λ multiplied by the constraint coefficients. More precisely, the constraint forces are $A^T \lambda$.

2.3.4 Evaluation of the Lagrange Multiplier method

On the contrary to the penalty function method (See Appendix B), the Lagrange multiplier method has the advantage of being exact where it provides directly the constraint forces. As the penalty function method, it can be extended to nonlinear constraints.

One of the downsides to the Lagrange multiplier method is that it introduces additional equations. By adding these to the original finite element, the system is expanded and it requires additional space for storing such a system. Finally, as the master-slave method, it is sensitive to the degree of linear independence of the constraints: if the constraint $u_2 = u_6$ is specified twice, the bordered stiffness is singular.

2.3.5 The Augmented Lagrangian Method

There is a connection between the general matrix forms of the Lagrangian multiplier method and the penalty function method, that is called *The Augmented Lagrangian Method*. Because the lower diagonal block of the bordered stiffness matrix in Equation (2.47) is zero, it is not possible to directly eliminate λ. To make it possible to eliminate λ, $\varepsilon\, S^{-1}$ is inserted to replace 0. S is a constraint-scaling diagonal matrix of appropriate order and ε is a small number. $w = \frac{1}{\varepsilon}$ is a large number of ε.

To maintain exactness of the second equation, $\varepsilon\, S^{-1}\, \lambda$ is added to the right-hand side yielding Equation (2.48):

$$\begin{bmatrix} K & A^T \\ A & \varepsilon\, S^{-1} \end{bmatrix} \begin{Bmatrix} u \\ \lambda \end{Bmatrix} = \begin{Bmatrix} f \\ \varepsilon\, S^{-1}\, \lambda^P\, b \end{Bmatrix} \tag{2.48}$$

where the superscript P, is attached to the λ on the right-hand-side and is acting like a tracer. It is now possible to solve for λ and thereafter for u. The results may be presented as Equation (2.49):

$$\begin{aligned} (K + w\, A^T\, S\, A)\, u &= f + w\, A^T\, S\, b - A^T\, \lambda^P \\ \lambda &= \lambda^P + w\, S\, (b - A\, u) \end{aligned} \tag{2.49}$$

If $\lambda^P = 0$ is inserted in the first equation in (2.49), it yields Equation (2.50):

$$(K + w\, A^T\, S\, A)\, u = f + w\, S\, b \tag{2.50}$$

Here by introducing $W = w\, S$, the general matrix equation (B.14) is retrieved of the penalty method.

This relation introduces the development of the iterative procedures where the accuracy of the penalty function method is desired to improve, while keeping w constant. This strategy avoids the previously mentioned problems surrounding the penalty function method when the weight w is gradually increased. This method is easily developed by reviewing the Equation (2.49). By using superscript k as an iteration index and keeping w fixed, the Equation (2.49) can be solved.

$$\begin{aligned} (K + A^T\, W\, A)\, u^k &= f + A^T\, W\, b - A^T\, \lambda^k \\ \lambda^{k+1} &= \lambda^k - W\, (b - A\, u^k) \end{aligned} \tag{2.51}$$

As for $k = 0, 1, \ldots,$ beginning with $\lambda^0 = 0$. Then u^0 is the penalty solution. If the process converges, the exact Lagrangian solution is recovered without the Lagrangian system in the Equation (2.48) needed to be solved directly.

The constraint force calculated out from the Lagrange multiplier λ can be seen as friction force acting on the interface. Thus, by introducing the factor μ, the interface with different roughness can be simulated. Therefore, the method is used as another approach for modelling interface.

All of these different types of interface elements are implemented in MATLAB and further explanation of the implementation of the elements are accounted for in Section 4.2.

Assessment of chosen elements 3

In this chapter the solutions described in Chapter 2 for modelling interface are assessed in simple pull-out test and outputs are presented and discussed.

3.1 Simple Pull-out test

In order to examine the behaviour of interface elements proposed in Chapter 2, the simple pull out test is conducted. As shown in the Figure 3.1, the soil is modelled as 4-noded rectangular elements with reinforcement in the middle, which is modeled as a 2-noded bar element. The soil domain is fully constrained in horizontal direction. To assure statically admissible model, the nodes at the bottom are also constrained in vertical direction as shown in Figure 3.1. There are in total four interface elements connecting the reinforcement with the soil. In order to emphasize behaviour of the interface, the surrounding material is modelled as linear elastic with parameters as follows:

Table 3.1: Parameters for the system

	E	ν
Soil	2000 kPa	0.25
Bar	20 000 kPa	-

The interface is in the first stage analyzed using a linear elastic constitutive model and a parametric study is conducted for both, normal and tangential behavior of the interface elements for stiffness coefficients.

The model is in first step loaded from the top at nodes 10, 11 and 12 by a uniform load of $q = 10$kN as shown in the Figure 3.1. The pull-out force $F_q = 10$kN is applied at node 15 in 2kN increments in the following steps, while the top load is kept constant for the whole analysis. Therefore, the model is exposed to six load steps in total.

3.1.1 Improved Goodman 4-node and 6-node element

As name suggests, the element is derived from the Goodman element, that is described in detail in the Chapter 2.1.2. In the assessment of normal behaviour there are two key parameters, the normal stress and the value of penetration. As mentioned before, there cannot be determined the one correct value of stiffness. Therefore, the parametric study needs to be performed before the analysis. Thus, the stiffness parameters k_n and k_s are chosen from 10^4 to 10^{10}.

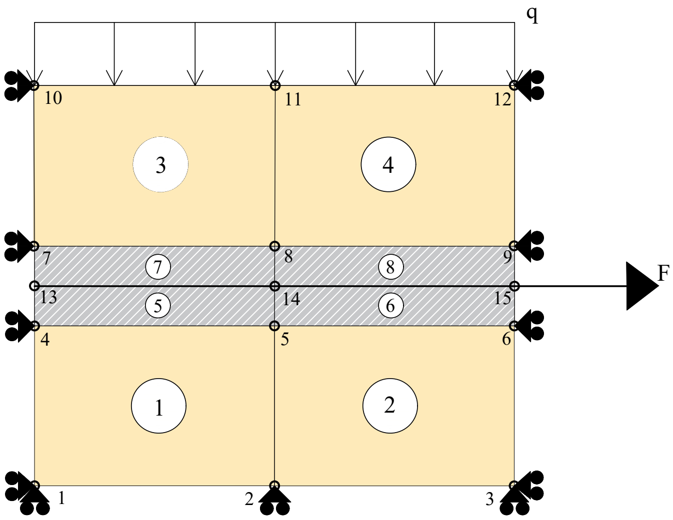

Figure 3.1: Simple pull-out test

Normal behavior

Under the given case, one can expect to have uniform normal stresses within the soil domain equal to the applied load from the top. The vertical stresses in the interface and its dependency on different chosen stiffness coefficients are presented in Table 3.2 and 3.3 for 4-noded and 6-noded element respectively, where σ_s represents the stresses in the soil and σ_i the stresses in the interface.

Table 3.2: Normal stresses in soil and interface vs. k_n [Pa] for 4-node element

k_n	10^4	10^5	10^6	10^7	10^8	10^9	10^{10}
σ_s [Pa]	10.000	10.000	10.000	10.000	10.000	10.000	10.000
σ_i [Pa]	10.000	10.000	9.999	9.995	9.998	10.006	-

Table 3.3: Normal stresses in soil and interface vs. k_n [Pa] for 6-node element

k_n	10^4	10^5	10^6	10^7	10^8	10^9	10^{10}
σ_s [Pa]	10.000	10.000	10.000	10.000	10.000	10.000	10.000
σ_i [Pa]	10.000	10.000	9.999	9.998	9.998	10.002	-

Table 3.4: Relative normal displacement [m] vs. k_n for 4-node and 6-node element

k_n	10^4	10^5	10^6	10^7	10^8	10^9	10^{10}
$v_8 - v_5$	$4 \cdot 10^{-3}$	$4 \cdot 10^{-4}$	$4 \cdot 10^{-5}$	$4 \cdot 10^{-6}$	$4 \cdot 10^{-7}$	$4 \cdot 10^{-8}$	-
$(v_8 - v_5)/v_5$ (%)	107.7	10.77	1.065	0.107	0.012	0.001	-

As can be seen from the Table 3.2, the interface elements in both cases yields satisfactory normal stresses for different stiffness coefficients. However, from the Table 3.4 we can observe the inverse relation between the relative displacement and the stiffness coefficient. It can be seen that node 5 and 8 are penetrating each other. In other words the relative displacement between those two nodes is non-zero value, despite being constrained. For the stiffness of 10^4 we can observe a penetration error of over 100%. As the stiffness of the interface is increased to 10^6, the relative error drops down to almost 1%, which in terms of finite element is acceptable inaccuracy. The error in relative displacement can be decreased almost to zero by using higher stiffness coefficient. However, it comes with price of inaccurate normal stresses and, in some cases, the convergence cannot be achieved.

Tangential behavior

In the next steps, the pull-out load is applied in the node of the reinforcement in increments of 2kN up to the total load of 10kN. The tangential displacements shown in m and stresses in kPa of the interface elements after every load increment are presented hereafter.

Table 3.5: Displacement in [m] of the bar for stiffness coefficient $k_s = 10^6$ [Pa] for 4-node element

Node	Load step [kN]					
	0	2	4	6	8	10
13	$-1.7 \cdot 10^{-23}$	$7.2 \cdot 10^{-8}$	$1.4 \cdot 10^{-7}$	$2.2 \cdot 10^{-7}$	$2.9 \cdot 10^{-7}$	$3.6 \cdot 10^{-7}$
14	$-4.4 \cdot 10^{-18}$	$5 \cdot 10^{-7}$	$1 \cdot 10^{-6}$	$1.5 \cdot 10^{-6}$	$2 \cdot 10^{-5}$	$2.5 \cdot 10^{-5}$
15	$-1.7 \cdot 10^{-23}$	$6.9 \cdot 10^{-6}$	$1.4 \cdot 10^{-5}$	$2.1 \cdot 10^{-5}$	$2.8 \cdot 10^{-5}$	$3.5 \cdot 10^{-5}$

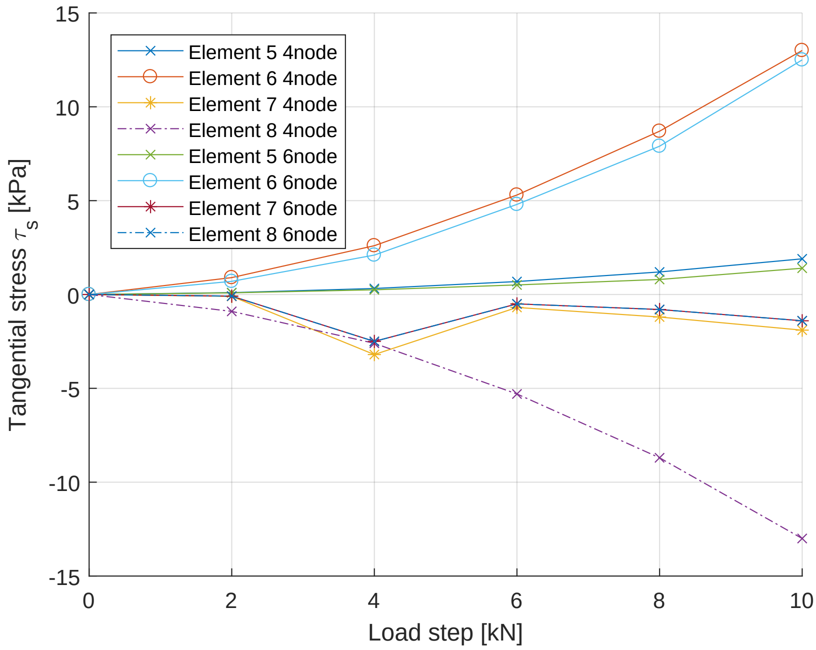

Figure 3.2: Tangential stresses for stiffness coefficient $k_s = 10^6$ [Pa] for 4-node and 6 node element

It can be observed in Table 3.5, that the bar yield some displacements even when there is no load applied. However, the values are effectively zero and does not affect the results in the next steps. Furthermore, it can be observed similar pattern in vertically neighbouring elements. The obvious difference in sign is due to the method of calculation of stresses. The discrepancy in load step of 4kN common for both interface elements in Element 7 is due to some numerical error during calculation, which is not observed for any other stiffness coefficient. To examine tangential response of interface element further, the analysis is done for stiffness coefficient of $k_s = 10^8$ and results are presented in similar way hereafter.

Table 3.6: Displacement in [m] of the bar for stiffness coefficient $k_s = 10^8$ [Pa]

Node	Load step [kN]					
	0	2	4	6	8	10
13	$-1 \cdot 10^{-24}$	$7.2 \cdot 10^{-10}$	$2.2 \cdot 10{-}9$	$4.5 \cdot 10^{-9}$	$7.6 \cdot 10^{-9}$	$1.1 \cdot 10^{-8}$
14	$5.3 \cdot 10^{-16}$	$3.2 \cdot 10^{-8}$	$9.7 \cdot 10^{-8}$	$1.9 \cdot 10^{-7}$	$3.2 \cdot 10^{-7}$	$4.9 \cdot 10^{-7}$
15	$-1 \cdot 10^{-24}$	$6.9 \cdot 10^{-8}$	$2.1 \cdot 10^{-7}$	$4.2 \cdot 10^{-7}$	$6.9 \cdot 10^{-7}$	$1.1 \cdot 10^{-6}$

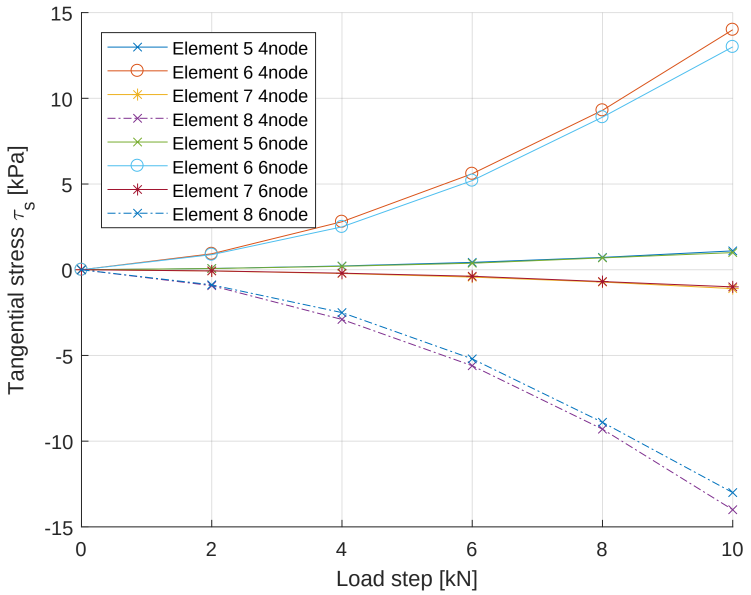

Figure 3.3: Tangential stresses for stiffness coefficient $k_s = 10^8$ [Pa] for 4-node and 6-node element

The behavior of interface elements in horizontal direction is as expected from the single element analysis shown in Chapter 2. Consequently, the higher stiffness yields higher values of stresses as can be seen in Figure 3.3. On the other hand, the lower values of stiffness may give more accurate stresses, whereas the error caused by penetration in normal direction would become over 27 (%). Furthermore, it can be seen correlation of the tangential stresses between two examined elements of Goodman, 4-node and 6-node.

3.1.2 Herrman element

The analysis of Herrman's element in interface is conducted using same model as for previous case. Thus, the model is loaded by q = 10kN on the top of the element 3 and 4, shown in the Figure 3.1. The normal stresses and relative normal displacement of the interface are studied and shown below.

Table 3.7: Normal stresses in soil and interface vs. k_n [Pa]

k_n	10^4	10^5	10^6	10^7	10^8	10^9	10^{10}
σ_s [Pa]	10.000	10.000	10.000	10.000	10.000	10.000	10.000
σ_i [Pa]	10.000	10.000	10.000	10.000	10.000	9.999	9.999

Table 3.8: Relative normal displacement in [m] vs. k_n [Pa]

k_n	10^4	10^5	10^6	10^7	10^8	10^9	10^{10}
$v_8 - v_5$	$1 \cdot 10^{-3}$	$1 \cdot 10^{-4}$	$1 \cdot 10^{-5}$	$1 \cdot 10^{-6}$	$1 \cdot 10^{-7}$	$1 \cdot 10^{-8}$	-
$(v_8 - v_5)/v_5$ (%)	27	2.7	0.069	0.007	0.0012	0.001	-

As it can be seen in Table 3.7, the normal stresses in the interface are more stable for different stiffness coefficients than it could be observed for Goodman element. However, for stiffness of higher order, small inaccuracy occurs. Moreover, it takes more iteration steps until convergence is reached. In the Table 3.8 it is shown relative displacements of the interface for set of stiffness values. It can be observed inverse relation with the stiffness coefficients. In terms of normal behaviour, the stiffness of 10^6 can be assumed as sufficient yielding relative error in displacement less than 1 (%).

In the next step, the tangential behavior is examined in similar way to the previous case. Thus, the horizontal load is applied in node 15 in increments of 2kN up to total load of 10kN. The tangential stresses and displacement after every step are shown hereafter.

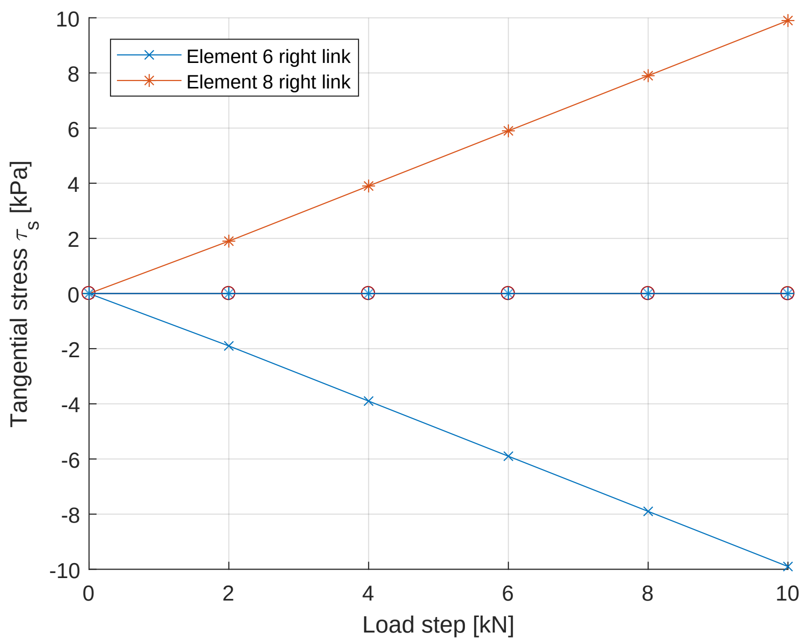

Figure 3.4: Tangential stresses for stiffness coefficient of 10^6

Table 3.9: Displacement in [m] of the bar for stiffness coefficient $k_s = 10^6$ [Pa]

Node	Load step [kN]					
	0	2	4	6	8	10
13	$-2 \cdot 10^{-13}$	$1.2 \cdot 10^{-12}$	$3.6 \cdot 10{-9}$	$5.1 \cdot 10^{-8}$	$1.9 \cdot 10^{-7}$	$2.6 \cdot 10^{-7}$
14	$-1 \cdot 10^{-9}$	$1.8 \cdot 10^{-8}$	$7.1 \cdot 10^{-8}$	$1.1 \cdot 10^{-7}$	$9.3 \cdot 10^{-7}$	$5.5 \cdot 10^{-6}$
15	$-2 \cdot 10^{-13}$	$2.9 \cdot 10^{-6}$	$3.9 \cdot 10^{-6}$	$5.9 \cdot 10^{-6}$	$7.8 \cdot 10^{-6}$	$9.9 \cdot 10^{-6}$

Regarding tangential stresses, the Herrman element seems to provide the most accurate stresses out of the presented zero-thickness elements, yielding the stresses as one could expect for given load. However, the stresses are evaluated in each link separately, for left and right link within one element respectively and as we learned in single element test, there is no transion between them as seen in the Figure 3.4. Therefore, there are non-zero tangential stresses present only in links where the load is applied. Another disadvantage concerning the Herrman element is that it cannot be used in fully plastic analysis as the element cannot account for hardening Li and Kaliakin [1993].

3.1.3 Thin-layer element

As a next approach of modeling interface, the thin-layer element is analyzed. In the first step the standard continuum element is analyzed following by the Desai thin layer element developed specifically for interface problems.

The analysis is performed for several sets of properties, which can be seen in Table 3.10 below. Each of the set is used for four different thickness ratios.

Table 3.10: Sets of properties

Set	k_n [Pa]	k_s [Pa]	ν
1	$4.5 \cdot 10^4$	$2.0 \cdot 10^4$	0.125
2	$4.5 \cdot 10^4$	$2.25 \cdot 10^4$	0.0
3	$1 \cdot 10^4$	$0.45 \cdot 10^6$	0.1
4	$1 \cdot 10^6$	$0.45 \cdot 10^8$	0.1
5	$1 \cdot 10^8$	$0.45 \cdot 10^8$	0.1

For each of the set is used aspect ratio t/B of 0.1, 0.01, 0.001 and 10^{-6} where B represents the width of the interface element, whereas the t represents the thickness.

Standard continuum element

In previous cases, there are analyzed several elements invented specifically for interface. It would be interesting to see how a regular continuum element can (or cannot) simulate the interface behavior. The set up used in analysis is same as for previous case and can be seen in Table 3.10. Following the previous procedure, the normal behavior is examined first.

Table 3.11: Normal stress and penetration for 1. set

t/B	σ_n [Pa]	$v_8 - v_5$ [m]
$1 \cdot 10^{-1}$	-10.000	$4.291 \cdot 10^{-4}$
$1 \cdot 10^{-2}$	-10.000	$4.291 \cdot 10^{-4}$
$1 \cdot 10^{-3}$	-10.000	$4.291 \cdot 10^{-4}$
$1 \cdot 10^{-6}$	-9.999	$4.291 \cdot 10^{-4}$

Table 3.12: Normal stress and penetration for 2. set

t/B	σ_n [Pa]	$v_8 - v_5$ [m]
$1 \cdot 10^{-1}$	-10.000	$4.444 \cdot 10^{-4}$
$1 \cdot 10^{-2}$	-10.000	$4.444 \cdot 10^{-4}$
$1 \cdot 10^{-3}$	-10.000	$4.444 \cdot 10^{-4}$
$1 \cdot 10^{-6}$	-9.999	$4.444 \cdot 10^{-4}$

The normal behavior seems to be identical to the one of Desai type as it can be seen in Table 3.11 and 3.12. However, the small deviation from the expected value of -10kPa is observed more often especially for smaller aspect ratio and higher stiffness. The result for sets 3. - 5. can be found in Appendix A.

In the next step, the shear respond of the standard element under different set of properties is analyzed and results are presented hereafter.

Table 3.13: Shear stress in interface for 4.set

t/B	Shear stress τ_y [Pa] in Gauss points			
	1	2	3	4
$1 \cdot 10^{-1}$	$-2.010 \cdot 10^{-1}$	$-1.339 \cdot 10^{-1}$	$1.256 \cdot 10^{1}$	$1.262 \cdot 10^{1}$
$1 \cdot 10^{-2}$	$-2.417 \cdot 10^{-1}$	$-2.410 \cdot 10^{-1}$	$1.275 \cdot 10^{1}$	$1.275 \cdot 10^{1}$
$1 \cdot 10^{-3}$	$-2.452 \cdot 10^{-8}$	$-2.452 \cdot 10^{-7}$	$1.274 \cdot 10^{1}$	$1.274 \cdot 10^{1}$
$1 \cdot 10^{-6}$	no convergence	no convergence	no convergence	no convergence

Table 3.14: Shear stress in interface for 5.set

t/B	Shear stress τ_y [Pa] in Gauss points			
	1	2	3	4
$1 \cdot 10^{-1}$	$-2.175 \cdot 10^{-1}$	$-1.505 \cdot 10^{-1}$	$1.262 \cdot 10^{1}$	$1.269 \cdot 10^{1}$
$1 \cdot 10^{-2}$	$-2.417 \cdot 10^{-1}$	$-2.410 \cdot 10^{-1}$	$1.275 \cdot 10^{1}$	$1.275 \cdot 10^{1}$
$1 \cdot 10^{-3}$	$-2.448 \cdot 10^{-8}$	$-2.448 \cdot 10^{-7}$	$1.274 \cdot 10^{1}$	$1.274 \cdot 10^{1}$
$1 \cdot 10^{-6}$	no convergence	no convergence	no convergence	no convergence

Desai thin layer element

Conceptually, it is a regular continuum element with small thickness, which in the limit can go to zero. The difference from the standard continuum element, however, is in the calculation of constitutive matrix, whose entries are depending on chosen values of thickness and stiffness coefficients, see Chapter 2.2. As a part of the analysis of the element, the parametric study of above mentioned parameters is done by using the model shown in Figure 3.1.

The normal behavior is examined in the first step and the results can be seen below.

Table 3.15: Analysis of normal behavior of the interface for 1. set

t/B	σ_n [Pa]	$v_8 - v_5$ [m]
$1 \cdot 10^{-1}$	-10.000	$4.291 \cdot 10^{-4}$
$1 \cdot 10^{-2}$	-10.000	$4.286 \cdot 10^{-4}$
$1 \cdot 10^{-3}$	-10.000	$4.286 \cdot 10^{-4}$
$1 \cdot 10^{-6}$	-9.999	$4.286 \cdot 10^{-4}$

Table 3.16: Analysis of normal behavior of the interface for 2. set

t/B	σ_n [Pa]	$v_8 - v_5$ [m]
$1 \cdot 10^{-1}$	-10.000	$4.444 \cdot 10^{-4}$
$1 \cdot 10^{-2}$	-10.000	$4.444 \cdot 10^{-4}$
$1 \cdot 10^{-3}$	-10.000	$4.444 \cdot 10^{-4}$
$1 \cdot 10^{-6}$	-9.999	$4.444 \cdot 10^{-4}$

For the sake of analysis, only first two sets are shown here, the other three can be found in Appendix A. It can be seen no significant deviation from the expected stress values of -10.000kPa. Additionally, the relative displacement, representing the penetration of the neighbouring soil into interface converged approximately at $4 \cdot 10^{-4}$. This value is smaller by order of 10^{-1} in comparison to the Improved Goodman element for similar stiffness coefficient. In the next sets, which can be seen in Appendix A, the similar pattern can be seen when stiffness is increased while no significant inaccuracy is observed regarding normal stresses in the interface.

As mentioned in Chapter 2, when the interface element thickness approaches zero, the previously studied zero-thickness elements should be restored. This assumption can be shown in Table 3.17 and 3.18 hereafter. It can be seen that the values of the in-plane strain ε_x converge to zero with decreasing thickness. Moreover, the in-plane stress σ_x tend to converge to one value. In the Table 3.18 for the 2. set of parameters with the Poisson ratio equal to zero $\nu = 0$, it can be seen zero values for both in-plane components for all thicknesses. Therefore, the assumption is proved and the in-plane entries can be avoided when thickness approaches zero without any significant error.

Table 3.17: In-plane stresses and strains for 1. set

t/B	σ_x [Pa]	ε_x
$1 \cdot 10^{-1}$	-1.418	$2.130 \cdot 10^{-6}$
$1 \cdot 10^{-2}$	-1.428	$2.142 \cdot 10^{-7}$
$1 \cdot 10^{-3}$	-1.429	$2.142 \cdot 10^{-8}$
$1 \cdot 10^{-6}$	-1.429	$2.142 \cdot 10^{-11}$

Table 3.18: In-plane stresses and strains for 2. set

t/B	σ_x [Pa]	ε_x
$1 \cdot 10^{-1}$	$1.222 \cdot 10^{-15}$	$2.717 \cdot 10^{-16}$
$1 \cdot 10^{-2}$	0	0
$1 \cdot 10^{-3}$	0	0
$1 \cdot 10^{-6}$	0	0

The rest of the tables for sets 3. -5. can be found in Appendix A. The tangential behavior is examined after applying the pull-out force of 10kN. The values of shear stress are presented for each Gauss point, whose positions regarding the numbers can be seen in Figure 3.5. The shear stress is analyzed for each set of parameters and presented in Table 3.19 and 3.20 below.

Table 3.19: Shear stress in interface for 4. set

t/B	Shear stress τ_y [Pa] in Gauss points			
	1	2	3	4
$1 \cdot 10^{-1}$	$-2.642 \cdot 10^{-1}$	$-1.903 \cdot 10^{-1}$	$1.251 \cdot 10^{1}$	$1.258 \cdot 10^{1}$
$1 \cdot 10^{-2}$	$-2.455 \cdot 10^{-1}$	$-2.447 \cdot 10^{-1}$	$1.274 \cdot 10^{1}$	$1.274 \cdot 10^{1}$
$1 \cdot 10^{-3}$	$-2.455 \cdot 10^{-1}$	$-2.455 \cdot 10^{-1}$	$1.274 \cdot 10^{1}$	$1.274 \cdot 10^{1}$
$1 \cdot 10^{-6}$	$-2.452 \cdot 10^{-1}$	$-2.452 \cdot 10^{-1}$	$1.274 \cdot 10^{1}$	$1.274 \cdot 10^{1}$

Table 3.20: Shear stress in interface for 5. set

t/B	Shear stress τ_y [Pa] in Gauss points			
	1	2	3	4
$1 \cdot 10^{-1}$	$-2.660 \cdot 10^{-1}$	$-1.921 \cdot 10^{-1}$	$1.251 \cdot 10^{1}$	$1.259 \cdot 10^{1}$
$1 \cdot 10^{-2}$	$-2.454 \cdot 10^{-1}$	$-2.446 \cdot 10^{-1}$	$1.274 \cdot 10^{1}$	$1.274 \cdot 10^{1}$
$1 \cdot 10^{-3}$	$-2.453 \cdot 10^{-1}$	$-2.453 \cdot 10^{-1}$	$1.274 \cdot 10^{1}$	$1.274 \cdot 10^{1}$
$1 \cdot 10^{-6}$	$-2.452 \cdot 10^{-1}$	$-2.452 \cdot 10^{-1}$	$1.274 \cdot 10^{1}$	$1.274 \cdot 10^{1}$

Table 3.21: In-plane stresses and strains for Desai element 3. set

t/B	σ_x [Pa]	ε_x
$1 \cdot 10^{-1}$	$-5.179 \cdot 10^{1}$	$7.654 \cdot 10^{-6}$
$1 \cdot 10^{-2}$	$-5.179 \cdot 10^{1}$	$3.982 \cdot 10^{-6}$
$1 \cdot 10^{-3}$	$-5.179 \cdot 10^{1}$	$3.614 \cdot 10^{-6}$
$1 \cdot 10^{-6}$	$-5.179 \cdot 10^{1}$	$3.574 \cdot 10^{-6}$

Table 3.22: In-plane stresses and strains for Desai element 4. set

t/B	σ_x [Pa]	ε_x
$1 \cdot 10^{-1}$	$-5.058 \cdot 10^{1}$	$7.654 \cdot 10^{-4}$
$1 \cdot 10^{-2}$	$-5.294 \cdot 10^{1}$	$2.789 \cdot 10^{-4}$
$1 \cdot 10^{-3}$	$-5.314 \cdot 10^{1}$	$1.755 \cdot 10^{-5}$
$1 \cdot 10^{-6}$	$-5.317 \cdot 10^{1}$	$1.251 \cdot 10^{-5}$

Table 3.23: In-plane stresses and strains for Desai element 5. set

t/B	σ_x [Pa]	ε_x
$1 \cdot 10^{-1}$	$1.054 \cdot 10^{4}$	$1.121 \cdot 10^{-3}$
$1 \cdot 10^{-2}$	$5.524 \cdot 10^{2}$	$1.145 \cdot 10^{-3}$
$1 \cdot 10^{-3}$	$-4.721 \cdot 10^{2}$	$1.145 \cdot 10^{-3}$
$1 \cdot 10^{-6}$	$-5.858 \cdot 10^{2}$	$1.145 \cdot 10^{-3}$

It can be observed that for both sets, the values of shear stresses are changing only slightly as the thickness is decreasing. Moreover, the difference between these two sets is negligible so it can be assumed as converged state. The shear stress in top Gauss points 3 and 4 shown in the Figure 3.5 yields similar results as in the Goodman zero-thickness element. However, it needs to be noted that the same increase in stresses is observed with increasing the stiffness, which in some cases can yield unrealistic values of shear stress. Additionally, the top value seems to be decreased by shear stress in bottom Gauss points 1 and 2. This is due to the natural deformation pattern of quadratic elements as seen in Figure 3.6. The remaining data for sets 1. - 3. can be found in Appendix A.

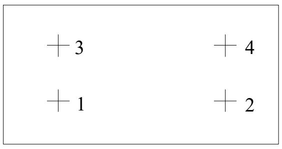

Figure 3.5: Gauss points in a quadratic 4 noded element

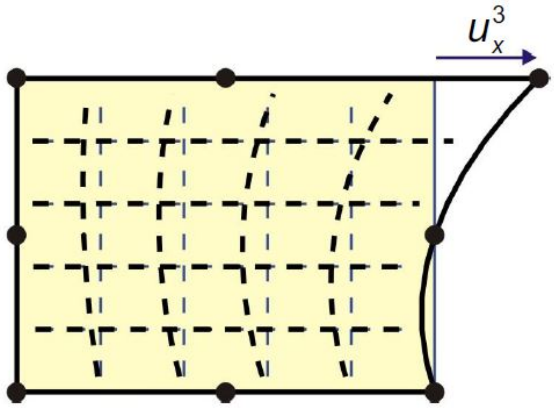

Figure 3.6: Natural deformation pattern of quadratic element, Clausen [2016].

Finally, the horizontal displacement of the reinforcement is analyzed and results can be seen in Table 3.24 and 3.25 below for converged 4. and 5. sets according to the shear analysis. The results for the remaining sets of parameters are shown in Appendix A.

Table 3.24: Horizontal displacement [m] of the reinforcement for 4. set

t/B	Horizontal displacement in bar nodes		
	13	14	15
$1 \cdot 10^{-1}$	$5.329 \cdot 10^{-6}$	$1.227 \cdot 10^{-5}$	$3.660 \cdot 10^{-5}$
$1 \cdot 10^{-2}$	$6.118 \cdot 10^{-6}$	$1.877 \cdot 10^{-5}$	$3.714 \cdot 10^{-5}$
$1 \cdot 10^{-3}$	$6.157 \cdot 10^{-6}$	$1.890 \cdot 10^{-5}$	$3.712 \cdot 10^{-5}$
$1 \cdot 10^{-6}$	$6.160 \cdot 10^{-6}$	$1.890 \cdot 10^{-5}$	$3.712 \cdot 10^{-5}$

Table 3.25: Horizontal displacement [m] of the reinforcement for 5. set

t/B	Horizontal displacement in Bar nodes		
	13	14	15
$1 \cdot 10^{-1}$	$4.996 \cdot 10^{-8}$	$5.864 \cdot 10^{-8}$	$3.829 \cdot 10^{-7}$
$1 \cdot 10^{-2}$	$5.465 \cdot 10^{-8}$	$1.269 \cdot 10^{-7}$	$3.851 \cdot 10^{-7}$
$1 \cdot 10^{-3}$	$5.503 \cdot 10^{-8}$	$1.907 \cdot 10^{-7}$	$3.848 \cdot 10^{-7}$
$1 \cdot 10^{-6}$	$5.507 \cdot 10^{-8}$	$1.920 \cdot 10^{-7}$	$3.848 \cdot 10^{-7}$

The displacement is gradually increasing in nodes closer to the location of the applied force, as expected. Furthermore, the magnitude of the displacement is in accordance with the displacement of Goodman zero thickness element for given parameters. It can be observed slight increase of the values as the element becomes narrower. This could be due to the more concentrated impact of the applied force.

4 Model of footing

In this chapter the focus is on load bearing capacity analysis of a footing resting on a soil domain. The main objective of this chapter is to test the footing in PLAXIS 2D and Optum G2, which are FEM tools specialized for geotechnical problems. Additionally, the analysis is carried out in MATLAB software. The footing is analyzed in regards to the ultimate limit state.

It is possible to utilize multiple models for numerical calculations of the soil response. The footing will be tested using the Mohr-Coulomb constitutive model according to the Appendix G. Following, the steps of the numerical analysis are presented. Firstly, the model is constructed in PLAXIS 2D and Optum G2, i.e. it is defined the soil stratigraphy and the structure. Secondly, the different parameters such as stiffness and strength parameters are defined. The following step is to carry out a convergence analysis that is necessary and an important part before analysis in order to eliminate possible sources of errors. As for any finite element analysis, the procedure is divide into three main parts, as shown in the Figure 4.1.

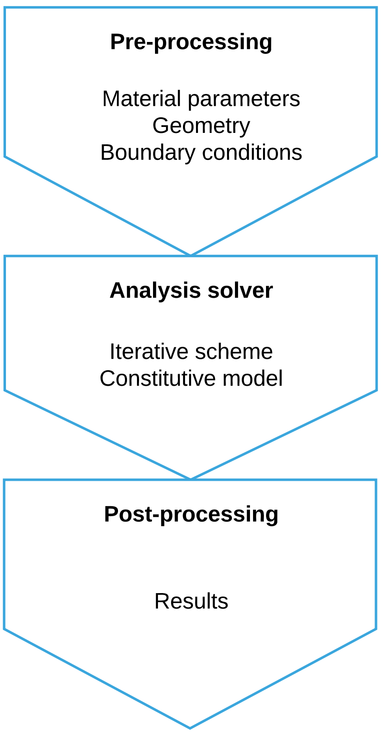

Figure 4.1: Finite Element procedure

4.1 Model in software

To construct the most similar model for all the used softwares, the set up in the pre-processing part for the three different programs are identical. Since the analysis is conducted in elasto-plasticity, the strength parameters needs to be included as well. Thus, the set of material properties can be seen in Table 4.1.

Table 4.1: Soil parameters for model

	E	ν	c	φ	ψ	γ
Soil	30MPa	0.25	1kPa	25°	25°	15kN/m^3

Additionally, the models in MATLAB, PLAXIS 2D and Optum G2 are processing the same boundary conditions, thus the domain is fully constrained from the bottom. Additionally, the side boundary nodes are constrained only in horizontal direction, allowing for the effect of the footing. Furthermore for PLAXIS 2D and MATLAB, the load is simulated by forced displacement of the target of 0.1m that are acting on the top nodes ranging from the top left corner to the specified length of the footing, that are set to be 1m. The model is illustrated in the Figure 4.2. The types of interface elements featured in the commercial software are not specified. The interface elements are modelled by plates that are assigned interface material and strength properties. In addition, it is possible to assign a virtual thickness to the interface. This will be further explained in Section 4.1.1. In this chapter, interface thicknesses of 0.01m and 0.005m are studied. However, solely 0.01m is analyzed in PLAXIS 2D, when that is the lowest allowable interface thickness for this commercial program.

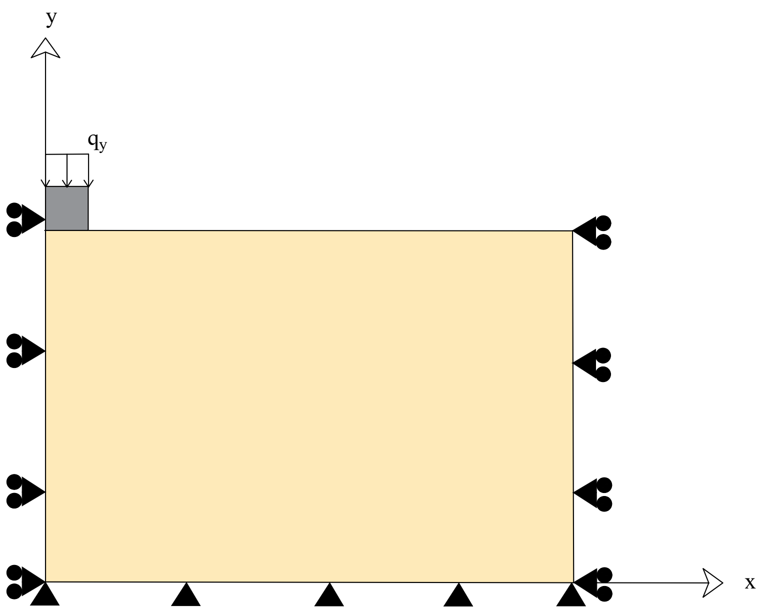

Figure 4.2: Model of the footing

4.1.1 PLAXIS 2D

Model setup

The model in PLAXIS 2D represents a circular foundation on a soil domain. The model is designed axisymmetric around the y-axis (see the Figure 4.3).

The soil domain is chosen to exceed 20 times the radius of the foundation in length along the x-axis with the foundation placed at the far left edge. The depth of the soil domain relative to the y-coordinate zero reference is set to 15 times the radius of the foundation.

Due to simplicity and that the main focus is directed towards the interface elements, so the soil domain only consists of one soil type. PLAXIS 2D allows the foundation to be simulated by the forced displacement only and it is fixed in the horizontal direction and therefore to the axis of revolution, allowing axisymmetry. This is illustrated as vertical lines at the top of the soil in Figure 4.3. The main soil domain, coloured in light blue in the Figure 4.3 contains soil parameters of shown in the Table 4.1. The soil follows the Mohr-Coulomb yield criterion and is considered elastic perfectly-plastic. The model is assumed associated where the friction angle φ is equal to the dilation angle ψ, $\varphi = \psi$.

The next step is to establish the interface. Interfaces are joint elements that are created between two different materials to allow proper modelling of soil-structure interaction. Interfaces may be used to simulate the thin zone of intensely shearing material at the contact. The interface is created as a line at the top of the geometry line where the interaction with the soil takes place. It is possible to choose any interface thickness by the feature virtual interface thickness. The interface is placed at the geometry line, that allows a full interaction between structural object and the surrounding soil. To be able to differentiate between the two possible interfaces along the geometry line, the interfaces are identified by a minus sign seen in the Figure 4.3 and a plus sign. The interface has a property called virtual thickness assigned to it. This property is a imaginary dimension used to define the material properties of the interface. Generally, the virtual thickness is suppose to be small, however if it is too small numerical ill-conditioning may occur.

The material properties of the interface element are chosen to be related to the soil model parameters of the surrounding soil. By choosing these material properties for the interface, a suitable value of the strength reduction factor R_{int} needs to be specified.

By selecting Mohr-Coulomb model, R_{int} is the main interface parameter. R_{int} can be selected from values ranging from $0-1$. In reality, the real soil-structure interaction in the interface is weaker and more flexible than the surrounding soil, which means that the R_{int} should be chosen to be less than 1. A search through literature was carried out to find the most suitable R_{int} for this type of interaction, but due to lack of satisfying accurate information, R_{int} is assumed to be 2/3 recommended by PLAXIS [2016]. In case of that the interface is elastic, both slippage and gapping could be expected to occur. In this report gapping is not considered, thus the elastic slip displacement is presented as:

$$\frac{\tau}{K_s} = \frac{\tau\, t_i}{G_i} \qquad \text{where} \qquad G_i = R_{int}^2\, G_{soil} \leq G_{soil} \tag{4.1}$$

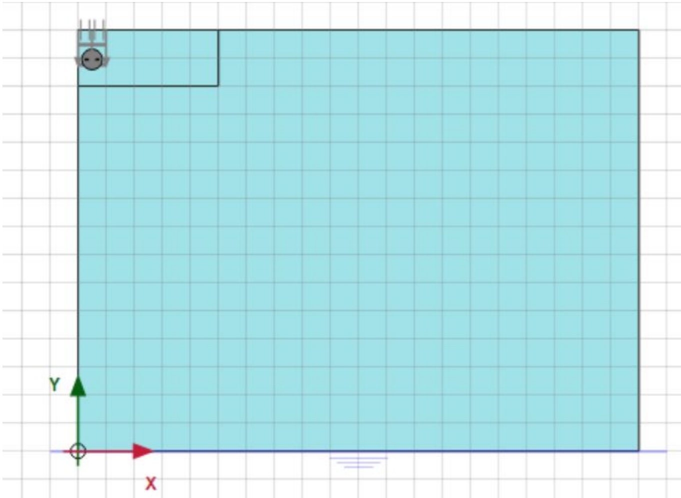

Figure 4.3: Model in PLAXIS 2D

τ	Shear stress
G_i	Shear modulus of the interface
t_i	Virtual interface thickness
K_s	Elastic interface shear stiffness

From (4.1), it is noticeable that the stiffness is highly dependent on the virtual thickness of the interface element. Something to have in mind is that a reduced value of R_{int} not only reduces the interface strength but also the interface stiffness. An elastic perfectly-plastic model is used to describe the behavior of the interfaces of the model. The Coulomb criterion is used to distinguish between elastic behavior, where small displacements can occur within the interface, and plastic interface behavior when permanent slip may occur. For the interface to remain elastic, the shear stress is expressed as:

$$|\tau| < -\sigma_N \tan \varphi_i + c_i \tag{4.2}$$

For plastic behavior, τ is given by:

$$|\tau| = -\sigma_N \tan \varphi_i + c_i \tag{4.3}$$

$\lvert\tau\rvert$	Shear stress
σ_N	Effective normal stress
φ_i	Interface friction angle
c_i	Cohesion of the interface

The interface properties are calculated from the soil properties by applying the strength reduction factor to the following rules:

$$c_i = R_{int}\, c_{soil} \tag{4.4}$$

$$\tan \varphi_i = R_{int} \tan \varphi_{soil} \leq \tan \varphi_{soil}$$

$$\psi_i = 0^\circ \quad \text{for} \quad R_{int} < 1 \quad \text{otherwise} \quad \psi_i = \psi_{soil}$$

In addition to the Mohr-Coulomb shear stress criterion, the tension cut-off criterion is also applied as:

$$\sigma_n < \sigma_{t,i} = R_{int}\,\sigma_{t,soil} \tag{4.5}$$

$\sigma_{t,soil}$	Tensile strength of the soil

When the load and the interface have been added to the model, the final step before the analysis is to discretize the model by generating a mesh. The generated mash transforms the model in to a finite element model consisting of 6-noded triangular elements. This is performed by the embedded codes and function in the PLAXIS 2D software. To achieve the most accurate results, the mesh close to the foundation needs to be as fine as possible. This has been done by implementing an additional soil polygon that is located in an area under the footing. This area is refined more times than the rest of the soil domain. This is done due to that the mesh close to the foundation is where it is expected the most of the deformations will occur. The refined finite element model is shown for the initial phase and for the deformed phase in Figure 4.4.

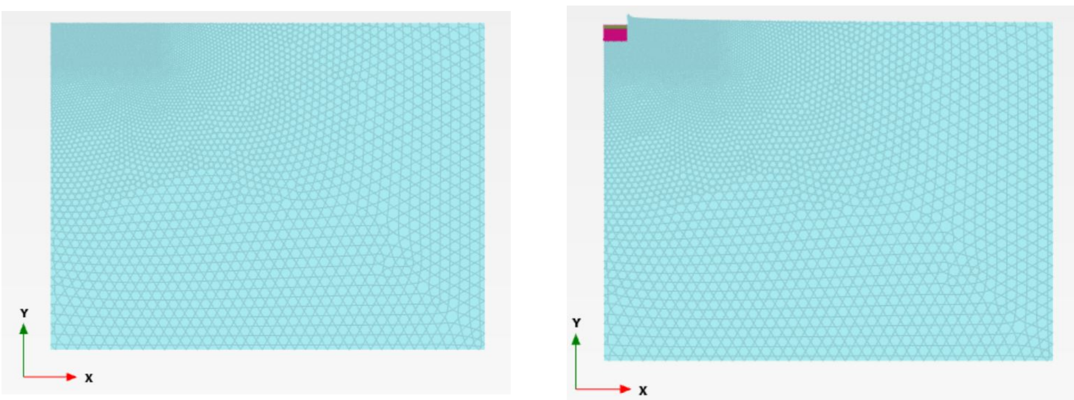

(a) Initial model (b) Deformed model

Figure 4.4: Mesh of the PLAXIS 2D model

Phases in the analysis

When all the soil and interface parameters are assigned to PLAXIS 2D, the calculation phases are defined. The ULS is analyzed and the calculation is divided into two phases:

1. *Initial phase*
   In this phase the K_0 procedure is chosen to calculate the initial stresses for the model. The vertical stresses that are in equilibrium with the self weight of the soil are generated. The horizontal stresses are than calculated from the specified value of K_0.

2. *Ultimate load phase*
   In this phase, the ultimate load that can be applied on the footing before the soil fail is calculated. This is presented in a load-displacement curve in Section 4.3.

4.1.2 Optum G2

OPTUM G2 is a finite element program for strength and deformation analysis of geotechnical boundary value problems. It is possible to compute limit loads and bearing capacities without having to perform a traditional step-by-step elastoplastic analysis. Apart from these features, a traditional step-by-step elastoplastic analysis is performed so that the models is as comparable as possible.

Model setup

The model in Optum G2 is also presented as a foundation on a soil domain. This model also is designed axisymmetric around the y-axis, see Figure 4.5.

The soil domain's dimensions and soil parameters correspond to the ones in PLAXIS 2D and are identical to the ones in the Table 4.1. This also include the supports and the conditions for the foundation. In this model, the green domain represents the soil and the grey domain represents the foundation.

The vertical load, q_y is modeled with load multiplier characteristics. Multiplier loads appear red and depending in which type of analysis, magnified to reach a certain value. In this case, the load multiplier is set to $1 \mathrm{kN/m^2}$, so the ultimate limit load is easy to retrieve from the result data. The soil-structure interaction is accounted for by the plate

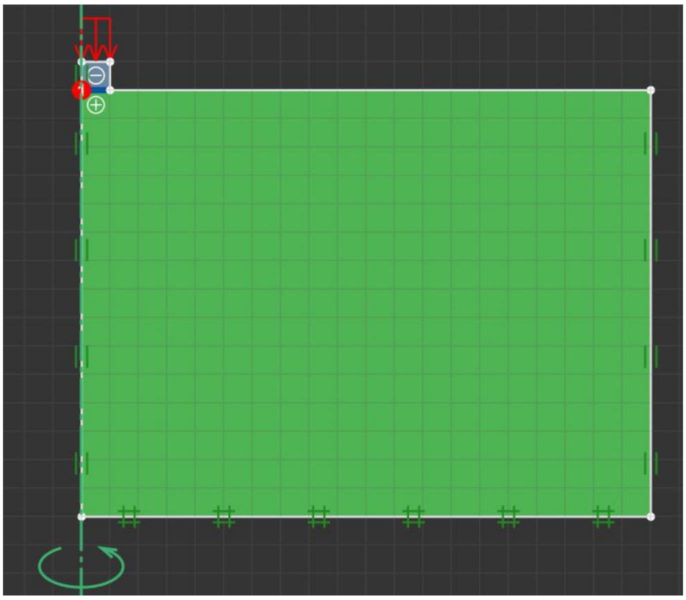

Figure 4.5: Model designed in Optum G2

feature. The plates are assigned to the segments that are a part of the domain to which solid materials already have been assigned. It is possible to choose any interface element thickness by the feature called interface thickness. The interface appear as plus and minus sign and can be modified by selecting a given rigid plate. These plates are beam elements that are used to model walls and various other thin layer elements. It is possible to specify a reduction factor such that the interface strength is reduced as compared to the parent material. For Mohr-Coulomb model, the reduced interface strength is the equal to the conditions used in PLAXIS 2D, see Equation 4.4.

Multiplier Elastoplastic Analysis

In this model, multiplier elastoplastic analysis which is a combination of limit analysis and elastoplastic analysis types. As in a limit analysis, the multiplier loads are amplified until system collapse. This is done in a step-by-step elastoplastic manner with deformations computed in each load step. There are three main fields in this analysis. This includes time scope, element type and number of elements. The element type used is 6-noded Gauss elements, as they are called in the software and these elements are triangular. This is consistent with the PLAXIS 2D model and the MATLAB model. Mesh refinement, here called mesh adaptivity, is specified with an amount of elements to start with and an amount of elements to end with.

When defining the load stepping N, target scheme is chosen. This scheme will continue the load stepping until the specified target is reached. This target is specified as a maximum absolute displacement u_{target}, as a load multiplier. The load stepping is performed in 50 steps of equal magnitude to be as comparable to the MATLAB model as possible.

When the load stepping settings are chosen, the next step is to appoint the wanted settings for the mesh. Mesh adaptivity is chosen so that mesh refinement is possible. Following, adaptivity iterations as set by default to three, meaning the number of adaptive refinement steps. Thereafter, the adaptivity frequency is specified, meaning how often the mesh is adapted for analysis. This is by default set to three. Next, the start elements specify the number of elements in the first adaptive iteration, which is there chosen to be 1000. Concerning adaptivity control shear dissipation is chosen for its efficiency. This control leads the mesh being refined according to the shear distribution of the plastic shear dissipation which is dependent on mean stress and the volumetric strain.

4.1.3 Convergence study of PLAXIS 2D and Optum G2

Before any further study of the numerical analysis from commercial softwares, it is necessary to perform a convergence study of the model to eliminate the errors in results. It is expected a higher stress concentration near the footing, therefore the mesh is refined in that region. Refining the mesh means an increase of nodes, and by this an increase in computational time will occur. Hence, it is not always suitable. Both the commercial program's refinement methods are explained in Sections 4.1.1 and 4.1.2.

A convergence analysis is performed to achieve the most accurate results from the software. This convergence analysis is performed by running the models in both software with an increase in degrees of freedom, and an increase in the refined mesh in the interested area. In the Figure 4.6, the results of a convergence analysis are presented for the model with interfaces with a thickness of 0.01m for PLAXIS 2D and Optum G2, as well as the results for Optum G2 with an inteface thickness of 0.005m. There are 8 meshes examined, there the degrees of freedom ranges from 1000 to 47 000. As can be seen in Figure 4.6 there are changes in the load bearing capacity from the number of degrees of freedom. From step 1 to step 2 there is a difference in load bearing capacity of 3.24%, which is not sufficient. By increasing the numbers of degrees of freedom, the error is reduced to 0.2%, which is more than sufficient. It can be seen load decrease in bearing capacity happens for PLAXIS 2D from step 1 to step 2 of . This is a difference of 3.60% and is not satisfactory. Thus a third step of convergence analysis is performed, yielding a difference of 2.48% from step 2. This is a somewhat big difference and a smaller difference is wanted, but due to instability in the PLAXIS 2D model, the model with 13 424 degrees of freedom is used in the further analysis. Considering the fact that the PLAXIS 2D model experienced some instability, the Optum G2 modeled used for further analysis has 13 958 degrees of freedom with an interface thickness of $t = 0.01$m and 13 774 degrees of freedom with an interface thickness of $t = 0.005$m. The results of the software analysis will be presented in a load-displacement graph in Section 4.3 and compare to the results from MATLAB.

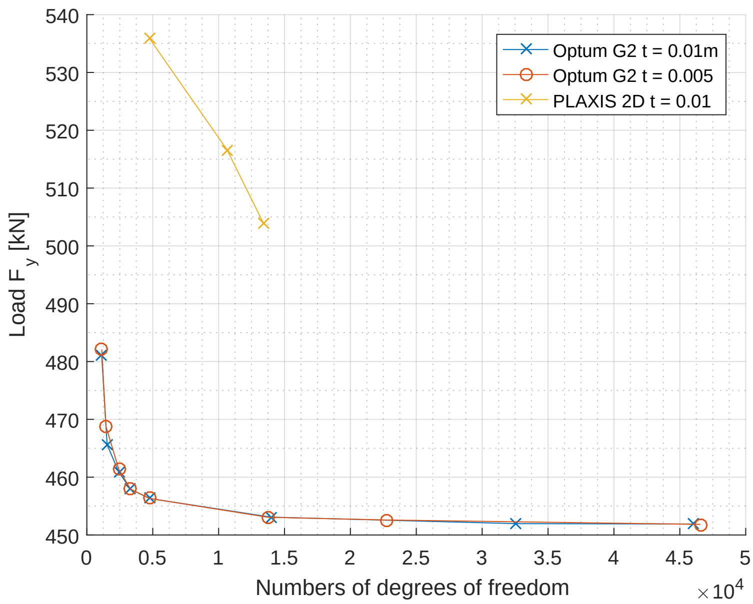

Figure 4.6: Convergence of the model

4.2 MATLAB model

In this section the code used for implementation of the interface element is presented and briefly described.

4.2.1 Model construction

In the next step, the geometry needs to be established. As mentioned in previous Section 4.1.1, the footing is symmetrical around the vertical axis and can be modelled in axisymmetry. Therefore, the geometry of the soil domain is created as a 2D object. Its dimensions are based on the width of the footing and are subject of the analysis in the first stage. The domain is discretized using the LST (Linear-Strain Triangle) elements, which consist of 6 nodes in total. The mesh initially used in the model is unstructured with refinements around the edge of the footing where the highest stress gradient is expected to occur as can be seen below. Once the mesh is established, the load and constrains needs to be specified, illustrated in Figure 4.7.

When the pre-processing step is done, the model is prepared for the analysis, therefore enters the Solver step according to the Figure 4.1.

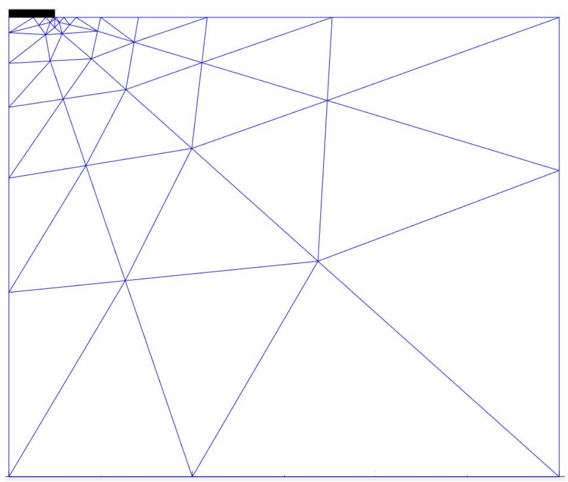

Figure 4.7: Geometry of the footing in MATLAB

Iterative scheme

As mentioned earlier, the model is non-linear, therefore iterative process of solving the finite element equations needs to be employed. The overview of possible iterative schemes can be studied at Appendix E. In the present model, the Newton-Raphson method is used which are explained in detail in Appendix E. Furthermore, the iterative technique require some convergence tolerance, when the residual is small enough. This residual is set to 10^{-5} in this model. The forced displacement mentioned earlier is applied in 10 steps in total.

Constitutive model

In the analysis, there is used the Modified Mohr-Coulomb model utilizing associated perfect plasticity, Clausen and Damkilde [2006].

4.2.2 Model calibration

Before the implementation of THE interface elements and the analysis of load bearing capacity with the software and analytical results, the so called calibration study should be performed in order to eliminate the amount of error sources.

Mesh density

Another important aspect of analysis is to use sufficient degree of discretization in order to produce reasonable results. Essentially, the more refined mesh, the better. However, in some cases the decrease in number of degrees of freedom can save a lot of computational memory while keeping the error negligible, therefore it can shorten the time needed for calculation.

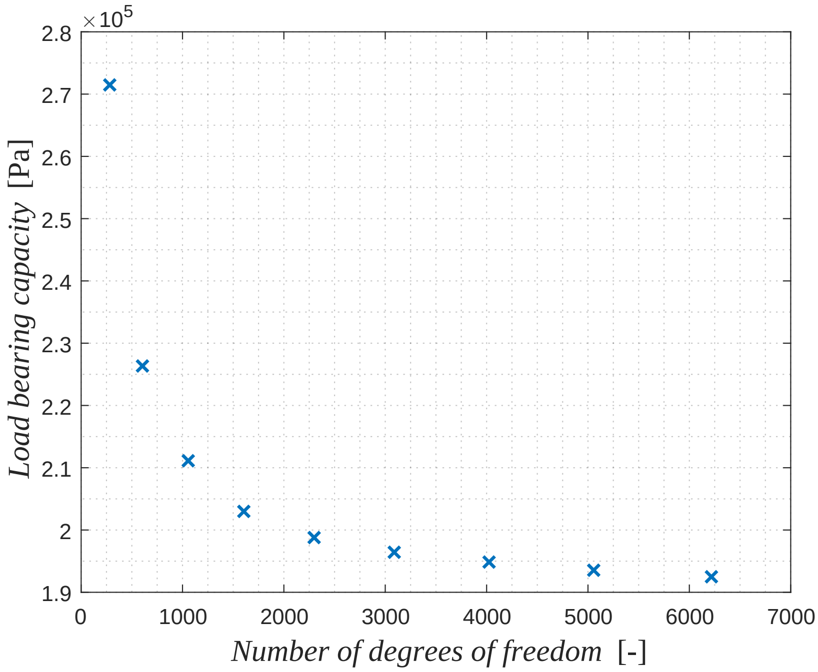

Figure 4.8: Analysis of mesh density in Matlab

There are 9 mesh sets examined, utilizing multiple total amount of degrees of freedom going from 289 for the most coarse set to the most finer set with 6222 degrees of freedom. As can be seen in Figure 4.8, there is no significant changes in value of load bearing capacity when the number of degrees of freedom approaches over 4000. Thus, the mesh set of 8 utilizing 4018 degrees of freedom is used for further analysis. The set employ in total 960 elements.

Mesh quality

One of the primary index of mesh quality is the magnitude of distortion of elements in the mesh, the skewness. The skewness shows how close to the ideal shape is the element. One of the method of evaluation the skewness is called Normalized Equiangular Skewness, SAS IP [2017]. The skewness is defined as in Equation (4.6).

$$\max\left[\frac{\theta_{max}-\theta_e}{180-\theta_e}, \frac{\theta_e-\theta_{min}}{\theta_e}\right] \tag{4.6}$$

where

θ_{max}	Largest angle in the face or cell
θ_{min}	smallest angle in the face or cell
θ_e	angle for an equiangular face/cell

The quality mesh for 2D element has the value of skewness approximately 0.1. On the other hand, the values over 0.75 are considered as a bad scaled element according to the Table 4.2.

Table 4.2: Mesh quality, SAS IP [2017]

Value of skeweness	Element quality
1	degenerate
$0.9- < 1$	bad (sliver)
$0.75 - 0.9$	poor
$0.5 - 0.75$	fair
$0.25 - 0.5$	good
$> 0 - 0.25$	excellent
0	equilateral

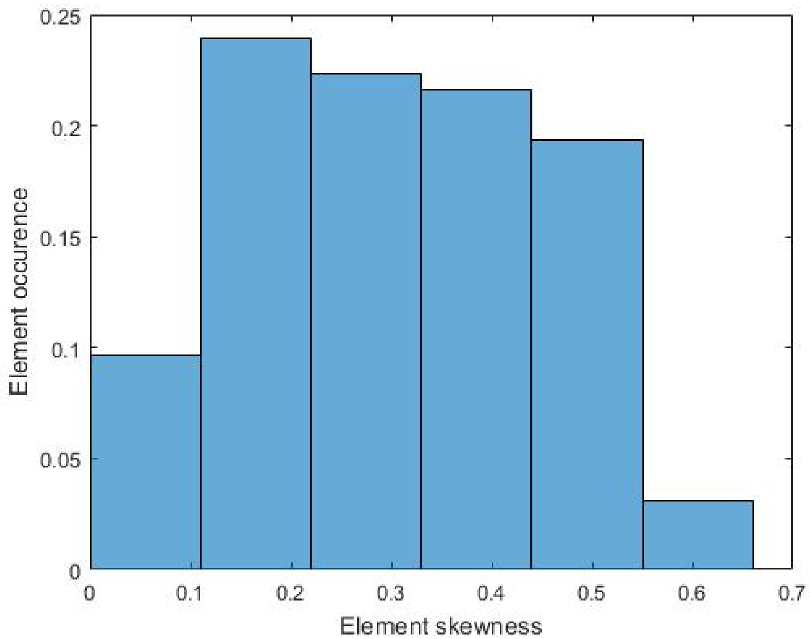

Figure 4.9: Analysis of mesh quality in Matlab

It can be seen, that over 95 % of the elements in the domain are with skeweness 0.5 or less, therefore the quality of the elements can be considered as satisfying and the effect on overall results should not be significant.

4.2.3 Implementation of interface elements

The purpose of this analysis is to prove the usability of the zero-thickness elements and thin-layer elements studied in Chapter 2 in the finite element model of the footing. Thus, the position of elements is placed along the simulated footing in top left corner as can be seen in Figure 4.7. The element implementation is straightforward and follows standard finite element procedure of assembling regular elements into the finite element model. In the first step, it needs to be created the extra nodes along the width of the footing. This is done by extracting the nodes of footing stored in the Nodeset matrix. Once the additional nodes are created and assembled into the topology matrix, the coordinate matrix needs to be adjusted accordingly. In case of zero thickness element, the extra nodes obey same coordinates as for the footing, whereas the nodes of thin-layer element has the vertical coordinate extended by the value of thickness of the element.

Furthermore, the Lagrange approach requires no additional nodes as it works as a frictional spring in each of the nodes along the footing. The method is more described in the Chapter 2.

4.3 Analysis of footing model with interface

The analysis is done in both plain strain and axisymmetry. Furthermore the results for plain strain case are normalized based on the Terzhaghi formula Clausen [2016] for surface footing shown hereafter in Equation 4.7 with use of bearing capacity factors taken from Chris Martin Martin [2016] regarding roughness coefficients. Due to the availability of load bearing capacity factors for different roughness only for strip footing, therefore plain strain case, there is comparison of results between the commercial softwares, PLAXIS 2D and Optum G2, and MATLAB software. However, the analytical results for model in axisymmetry are presented for fully rough and fully smooth interface providing the limit values within which the analysis should fit.

$$q_u = c\,N_c + \gamma\,r\,N_\gamma \tag{4.7}$$

There are 3 interface approaches analyzed, the Desai thin layer element, the Goodman Zero thickness element and the Lagrange approach. Furthermore, the Desai element is modelled for two thicknesses of 0.01 m and 0.005 m. The set of material parameters used throughout the analysis is shown in Table 4.1.

4.4 The case of plane strain

The results for roughness coefficients of 1/2 and 2/3 are presented hereafter. As mentioned earlier, the load bearing capacity is normalized for Terzaghi formula. Furthermore the vertical displacement values are normalized for the half of the length of the strip footing r.

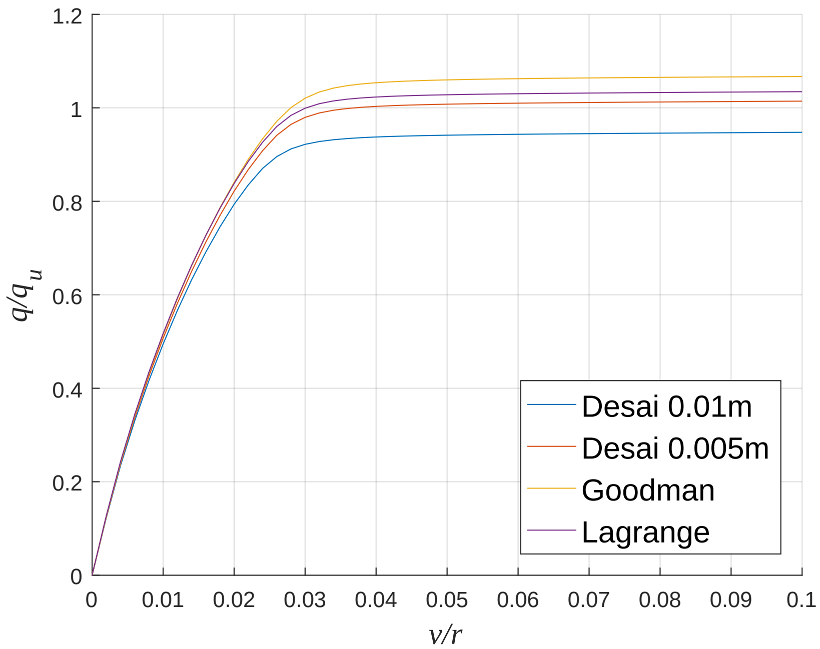

Figure 4.10: Load-displacement curve for roughness 1/2

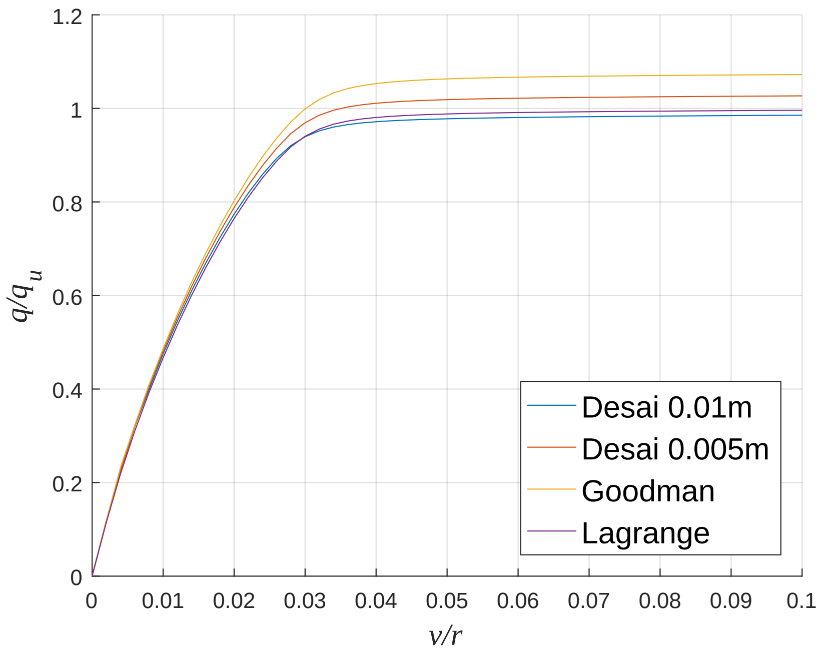

Figure 4.11: Load-displacement curve for roughness 2/3

Overall, the results from all chosen interface approaches convergence to the analytical solution. It can be seen, that for Desai type with thickness of $0.1m$, the disparity is the highest for both roughness coefficients. However, this error decrease with increased roughness coefficient down to around 3% as it can be seen in Figure 4.11. Little bit overconservative results with respect to analytical solution yields the Goodman interface with error over 2%. As opposed to the former approach, the deflection is increasing with increasing roughness. As most accurate solution with smallest deviation to the analytical value is the Lagrange approach with an error of 2.4%. However, the computational time is the highest out of the all assessed elements. It can be seen, that for thinner Desai element of 0.005m there is better correlation with analytical results than for the Desai with bigger thickness.

4.5 The case of axisymmetry

Figure 4.12 shows the load bearing capacity of the element with an interface thickness of 0.005m. There is also included the load bearing capacity using the Terzaghi formula for fully smooth and fully rough circular foundation, and these are used as upper and lower boundaries. Looking at the curves it can be seen that the Lagrange Method yields the highest load bearing capacity, whereas the Desai element yield a difference from the Lagrange method of 4.46%. The load bearing capacity from Optum G2 yields a difference of 7.69% from the Lagrange Method and 3.07% from Desai and it is the approach that yields the lowest load bearing capacity out of all examined interface approaches.

Due to the fact that the analytical solution given by Terzaghi formula does not provide the solution for any roughness between fully rough and fully smooth for axisymmetry, the exact comparison cannot be done for roughness coefficient of 2/3.

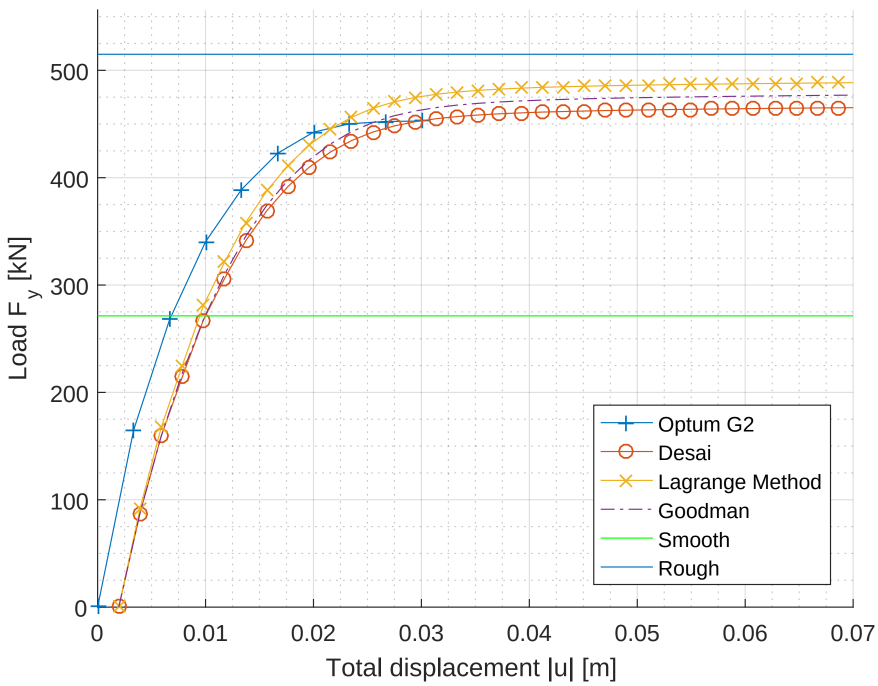

Figure 4.12: Load-displacement curve for an interface thickness of 0.005m

Figure 4.13 shows the load bearing capacity of the element with an interface thickness of 0.01m. As in the previous casem the load bearing capacity from Terzaghi formulas for fully smooth and fully rough circular foundation, are used as upper and lower boundaries. Looking at the curves, it is shown that PLAXIS 2D yields the highest load bearing capacity, with a difference of 2.85% from the Lagrange method. The elements that gives the most similar results is the Desai and the results from Optum G2, with a difference of 0.7%. However, the difference between the Desai and the Lagrange method is now increased to 7.11% which is an increase of 2.35%. By decreasing the interface thickness, the error between Optum G2 and Lagrange Method is also decreasing, as well as the difference between Desai and Lagrange method.

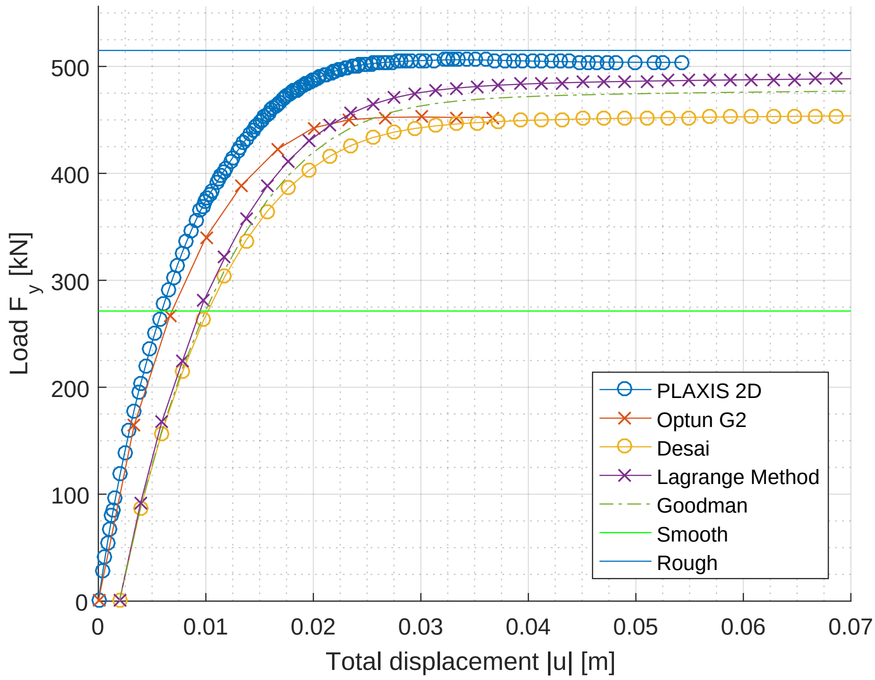

Figure 4.13: Load-displacement curve for an interface thickness of 0.01m

4.5.1 Sensitivity study of reduction factors

Figure 4.14 illustrates how the change in reduction factors are affecting the load bearing capacity of the model. Looking at the curves, it can be seen that Optum G2 is following a linear increase in the load bearing capacity from a reduction factor 0 - 0.5. Thereafter the curve starts to converge, and the model is not that affected by increase in reduction factor.

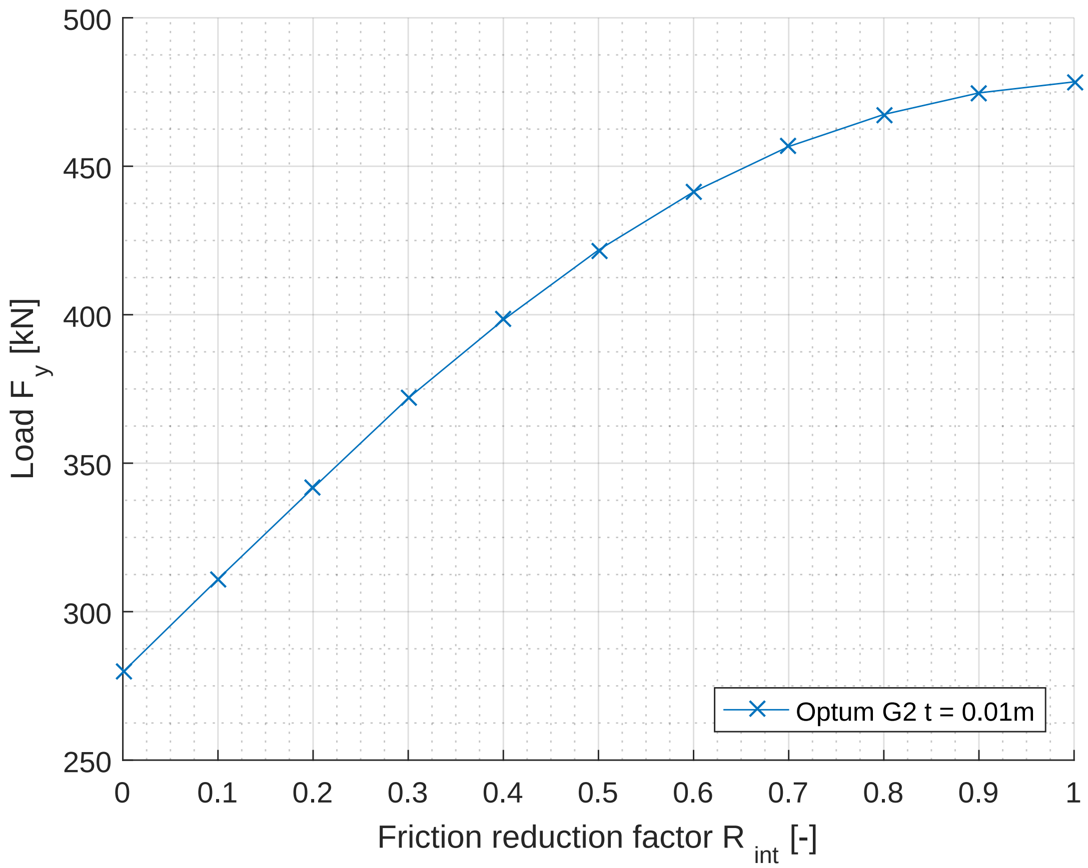

Figure 4.14: Sensitivity study of reduction factors from Optum G2

5 Conclusion

In this chapter the summary of studied approaches of modelling the interface is presented and possible future study is discussed.

The results from the Simple pull-out test has shown that the behavior of assessed interface elements are affected by many factors. To start with, the stiffness coefficient seems to be affecting the overall normal behavior regarding the Zero-thickness group of elements. There can be observed clear inverse pattern in relation between the stiffness coefficient and the rate of the interpenetration. The error can be significant for stiffness values such as 10^4. The solution seems to be in increasing the stiffness to sufficiently high order so the penetration is minimized. However, regarding the Goodman element, the tangential stresses are dependent on the value of chosen tangential stiffness coefficient, which in cases of higher values of stiffness yields unrealistic tangential stresses. On the other hand, the Herrman element does not rely on the value of tangential stiffness. Additionally, the tangential stresses seems to be more accurate. Nevertheless, the response to the applied horizontal load is taken only by the right link, therefore there is no transfer of forces within the interface element. Thus, the element is not suitable for further use despite the tangential stresses are as expected. Regarding the kinematic inconsistency, the original Goodman element, which has not been included in the Simple pull-out test, has experienced a deformation in the opposite direction of one of the nodes as opposed to the expectation. Therefore, the Improved Goodman type has been introduced, which solved the problem with inconsistency while maintaining the same tangential stresses from the original type.

The thin-layer group of elements has been analyzed as an another approach. There are two types included. The Desai type, which is designed specifically for interface problems, and the standard continuum element, which is added for sake of comparison, are tested. There has been observed the correlation between both elements. However, the difference occur when the thickness approaches value as low as 10^{-4}, where the standard continuum element becomes singular.

Finally, the chosen interface elements are analyzed in the footing model and compared to the analytical solution provided by Chris Martin and to the solution from commercial softwares. From the plain strain case, the Goodman type yields overconservative values while the other assessed types stays below or are equal to the analytical solution. In regards to axisymmetry case, the results from the interface with thickness of 0.01m for PLAXIS 2D yields values almost as high as for fully rough case according to analytical solution. This could be particularly due to not fully converged mesh. Disregarding the PLAXIS 2D solution, the Lagrange approach yields the highest load bearing capacity closely followed by Goodman approach. On the other hand, the most conservative solution is obtained from Desai and Optum G2 approaches as they are almost identical. However, the analytical solution for roughness of 2/3 is provided only for strip footing, i.e. plain strain. Regarding the axisymmetry, the validation is only possible for fully rough or fully smooth interface. According to the sensitivity study of reduction factors representing the roughness of interface, there is no significant change in load bearing capacity when the factor is increased over 0.6. Therefore, the results obtained from all types of interface approaches are in range according to the analytical upper boundary.

5.1 Suggestions for further study

The more extended parametric study of stiffness coefficients could be interesting to study in case of Zero-thickness elements as in thesis are used equal coefficients for normal and tangential direction. Additionally, the different elastoplastic constitutive models can be assessed with Desai interface element as suggested in literature. Furthermore, the response of the interface elements can be studied within non-associated plasticity.

To analyze a different model than a footing on soil would be also interesting. Such a model could be a triaxial test. Considering this case, the results of analysis of the commercial softwares used could be validated by actual experimental data.

Bibliography

Clausen, 2016. Johan Clausen. *Finite element formulation of two-dimensional elastic problems*. 2016.

Clausen and Damkilde, 2006. Johan Clausen and Lars Damkilde. *A Simple And Efficient FEM-Implementation Of The Modified Mohr-Coulomb Criterion*. Lund Universitet, 2006.

Cook et al., 2002. Robert D. Cook, David S. Malkus, Michael E. Plesha and Robert J. Witt. *Concepts and Applications of Finite Element Analysis*. ISBN: 978-0-471-35605-9, Fourth Edition. John Wiley & Sons, INC., 2002.

et.al., 1973. Ghambousi et.al. *Finite Element for Rock Joints and Interfaces*. 1973.

Felippa, 2004. Carlos A. Felippa. *Introduction to Finite Element Analysis*. University of Colorado, 2004.

Francavilla and Zienkiewicz, 1 1975. A. Francavilla and O. C. Zienkiewicz. *A note on numerical computation of elastic contact problems*. International Journal for Numerical Methods in Engineering, 9(4), 913–924, 1975. ISSN 1097-0207. doi: 10.1002/nme.1620090410. URL `http:https://doi.org/10.1002/nme.1620090410`.

Goodman, 1968. Richard E. Goodman. *A model for the mechanics of jointed rock*. vol. 94,no.sm3. American Society of Civil Engineers, 1968.

Herrmann, 1978. Leonard R. Herrmann. *Finite element analysis of contact problems*. vol. 104,no.em5. American Society of Civil Engineers, 1978.

Li and Kaliakin, 1993. Jianchao Li and Victor N. Kaliakin. *Numerical Simulation of Interfaces in Geomaterials: Development of New Zero-thickness Interface Elements*. University of Delaware , Newark, 1993.

Logan, 2017. Daryl L. Logan. *A First Course in the Finite Element Method*. ISBN: 0-534-55298-6. Chris Carson, 2017.

Martin, 2016. Chris Martin. *http://www.eng.ox.ac.uk/civil/people/cmm/software*. 2016.

NPTEL, 2015. NPTEL. *FEM for Two and Three Dimensional Solids: Axisymmetric Element*. 2015.

Ottosen and Ristinmaa, 2005. Ottosen and Ristinmaa. *Mechanics of Constitutive Modelling*. ISBN: 0-008-044606-X, 1st Edition. Elsevier, 2005.

PLAXIS, 2016. PLAXIS. *Material Models Manual*. 2016.

SAS IP, 2017. Inc. SAS IP. *Mesh quality measurement*. 2017.

Sharma and Desai, **1992**. K. G. Sharma and C. S. Desai. *Analysis and implementation of thin layer element for interfaces and joints*. 1992.

Wriggers, **2006**. Peter Wriggers. *Computational Contact Mechanics*. ISBN: 978-3-540-32608-3. Springer-Verlag Berlin Heidelberg, 2006.

List of Figures

List of Tables

Analysis of interface elements A

The remaining results from analysis are shown hereafter

A.1 The Desai thin layer element

A.1.1 Analysis of normal and in-plane components

Table A.1: Normal analysis of interface for 3. set

t/B	σ_n [Pa]	$v_8 - v_5$ [m]
$1 \cdot 10^{-1}$	-10.000	$1.960 \cdot 10^{-5}$
$1 \cdot 10^{-2}$	-10.000	$1.960 \cdot 10^{-5}$
$1 \cdot 10^{-3}$	-10.000	$1.960 \cdot 10^{-5}$
$1 \cdot 10^{-6}$	-9.999	$1.960 \cdot 10^{-5}$

Table A.2: Normal analysis of interface for 4. set

t/B	σ_n [Pa]	$v_8 - v_5$ [m]
$1 \cdot 10^{-1}$	-9.999	$1.960 \cdot 10^{-5}$
$1 \cdot 10^{-2}$	-10.000	$1.960 \cdot 10^{-5}$
$1 \cdot 10^{-3}$	-9.999	$1.960 \cdot 10^{-5}$
$1 \cdot 10^{-6}$	-9.999	$1.960 \cdot 10^{-5}$

Table A.3: Normal analysis of interface for 5. set

t/B	σ_n [Pa]	$v_8 - v_5$ [m]
$1 \cdot 10^{-1}$	-10.000	$1.960 \cdot 10^{-7}$
$1 \cdot 10^{-2}$	-10.000	$1.960 \cdot 10^{-7}$
$1 \cdot 10^{-3}$	-10.000	$1.960 \cdot 10^{-7}$
$1 \cdot 10^{-6}$	-9.999	$1.960 \cdot 10^{-7}$

Table A.4: In-plane stresses and strains for Desai element 3. set

t/B	σ_x [Pa]	ε_x
$1 \cdot 10^{-1}$	$-5.179 \cdot 10^{1}$	$7.654 \cdot 10^{-6}$
$1 \cdot 10^{-2}$	$-5.179 \cdot 10^{1}$	$3.982 \cdot 10^{-6}$
$1 \cdot 10^{-3}$	$-5.179 \cdot 10^{1}$	$3.614 \cdot 10^{-6}$
$1 \cdot 10^{-6}$	$-5.179 \cdot 10^{1}$	$3.574 \cdot 10^{-6}$

Table A.5: In-plane stresses and strains for Desai element 4. set

t/B	σ_x [Pa]	ε_x
$1 \cdot 10^{-1}$	$-5.058 \cdot 10^{1}$	$7.654 \cdot 10^{-4}$
$1 \cdot 10^{-2}$	$-5.294 \cdot 10^{1}$	$2.789 \cdot 10^{-4}$
$1 \cdot 10^{-3}$	$-5.314 \cdot 10^{1}$	$1.755 \cdot 10^{-5}$
$1 \cdot 10^{-6}$	$-5.317 \cdot 10^{1}$	$1.251 \cdot 10^{-5}$

Table A.6: In-plane stresses and strains for Desai element 5. set

t/B	σ_x [Pa]	ε_x
$1 \cdot 10^{-1}$	$1.054 \cdot 10^{4}$	$1.121 \cdot 10^{-3}$
$1 \cdot 10^{-2}$	$5.524 \cdot 10^{2}$	$1.145 \cdot 10^{-3}$
$1 \cdot 10^{-3}$	$-4.721 \cdot 10^{2}$	$1.145 \cdot 10^{-3}$
$1 \cdot 10^{-6}$	$-5.858 \cdot 10^{2}$	$1.145 \cdot 10^{-3}$

A.1.2 Analysis of tangential components

Table A.7: Shear stress in interface for 1.set

t/B	Shear stress τ_y [Pa] in Gauss points			
	1	2	3	4
$1 \cdot 10^{-1}$	$4.255 \cdot 10^{-1}$	$4.666 \cdot 10^{-1}$	7.733	7.774
$1 \cdot 10^{-2}$	$3.418 \cdot 10^{-1}$	$3.430 \cdot 10^{-1}$	7.780	7.781
$1 \cdot 10^{-3}$	$3.408 \cdot 10^{-1}$	$3.408 \cdot 10^{-1}$	7.767	7.767
$1 \cdot 10^{-6}$	$3.407 \cdot 10^{-1}$	$3.407 \cdot 10^{-1}$	7.765	7.765

Table A.8: Shear stress in interface for 2.set

t/B	Shear stress τ_y [Pa] in Gauss points			
	1	2	3	4
$1 \cdot 10^{-1}$	$3.284 \cdot 10^{-1}$	$3.712 \cdot 10^{-1}$	7.945	7.988
$1 \cdot 10^{-2}$	$2.684 \cdot 10^{-1}$	$2.697 \cdot 10^{-1}$	8.051	8.052
$1 \cdot 10^{-3}$	$2.690 \cdot 10^{-1}$	$2.691 \cdot 10^{-1}$	8.045	8.045
$1 \cdot 10^{-6}$	$2.692 \cdot 10^{-1}$	$2.692 \cdot 10^{-1}$	8.044	8.044

Table A.9: Shear stress in interface for 3.set

t/B	Shear stress τ_y [Pa] in Gauss points			
	1	2	3	4
$1 \cdot 10^{-1}$	1.506	1.536	4.700	4.730
$1 \cdot 10^{-2}$	1.488	1.489	4.680	4.682
$1 \cdot 10^{-3}$	1.487	1.487	4.673	4.674
$1 \cdot 10^{-6}$	1.487	1.487	4.673	4.674

Table A.10: Horizontal displacement of the reinforcement for 1.set

t/B	Horizontal displacement in Bar nodes		
	13	14	15
$1 \cdot 10^{-1}$	$2.113 \cdot 10^{-4}$	$5.181 \cdot 10^{-4}$	$5.181 \cdot 10^{-4}$
$1 \cdot 10^{-2}$	$2.236 \cdot 10^{-4}$	$3.321 \cdot 10^{-4}$	$5.245 \cdot 10^{-4}$
$1 \cdot 10^{-3}$	$2.240 \cdot 10^{-4}$	$3.321 \cdot 10^{-4}$	$5.241 \cdot 10^{-4}$
$1 \cdot 10^{-6}$	$2.241 \cdot 10^{-4}$	$3.321 \cdot 10^{-4}$	$5.241 \cdot 10^{-4}$

Table A.11: Horizontal displacement of the reinforcement for 2.set

t/B	Horizontal displacement in Bar nodes		
	13	14	15
$1 \cdot 10^{-1}$	$1.905 \cdot 10^{-4}$	$2.883 \cdot 10^{-4}$	$4.750 \cdot 10^{-4}$
$1 \cdot 10^{-2}$	$1.982 \cdot 10^{-4}$	$3.022 \cdot 10^{-4}$	$4.839 \cdot 10^{-4}$
$1 \cdot 10^{-3}$	$1.905 \cdot 10^{-4}$	$3.022 \cdot 10^{-4}$	$4.839 \cdot 10^{-4}$
$1 \cdot 10^{-6}$	$1.982 \cdot 10^{-4}$	$3.022 \cdot 10^{-4}$	$4.839 \cdot 10^{-4}$

Table A.12: Horizontal displacement of the reinforcement for 3.set

t/B	Horizontal displacement in Bar nodes		
	13	14	15
$1 \cdot 10^{-1}$	$8.433 \cdot 10^{-4}$	$9.774 \cdot 10^{-4}$	$1.286 \cdot 10^{-4}$
$1 \cdot 10^{-2}$	$8.505 \cdot 10^{-4}$	$9.823 \cdot 10^{-4}$	$1.285 \cdot 10^{-4}$
$1 \cdot 10^{-3}$	$8.505 \cdot 10^{-4}$	$9.823 \cdot 10^{-4}$	$1.285 \cdot 10^{-4}$
$1 \cdot 10^{-6}$	$8.505 \cdot 10^{-4}$	$9.823 \cdot 10^{-4}$	$1.285 \cdot 10^{-4}$

A.2 Standard continuum element

A.2.1 Analysis of normal and in-plane components

Table A.13: Normal stress and penetration for 3.set

t/B	σ_n [Pa]	$v_8 - v_5$ [m]
$1 \cdot 10^{-1}$	-10.000	$1.956 \cdot 10^{-3}$
$1 \cdot 10^{-2}$	-10.000	$1.956 \cdot 10^{-3}$
$1 \cdot 10^{-3}$	-10.000	$1.956 \cdot 10^{-3}$
$1 \cdot 10^{-6}$	-9.999	$1.956 \cdot 10^{-3}$

Table A.14: Normal stress and penetration for 4.set

t/B	σ_n [Pa]	$v_8 - v_5$ [m]
$1 \cdot 10^{-1}$	-9.999	$1.956 \cdot 10^{-5}$
$1 \cdot 10^{-2}$	-10.000	$1.956 \cdot 10^{-5}$
$1 \cdot 10^{-3}$	-9.999	$1.956 \cdot 10^{-5}$
$1 \cdot 10^{-6}$	-9.999	$1.956 \cdot 10^{-5}$

Table A.15: Normal stress and penetration for 5.set

t/B	σ_n [Pa]	$v_8 - v_5$ [m]
$1 \cdot 10^{-1}$	-10.000	$1.956 \cdot 10^{-7}$
$1 \cdot 10^{-2}$	-10.000	$1.956 \cdot 10^{-7}$
$1 \cdot 10^{-3}$	-10.000	$1.956 \cdot 10^{-7}$
$1 \cdot 10^{-6}$	-9.999	$1.956 \cdot 10^{-7}$

A.2.2 Analysis of tangential components

Table A.16: Shear stress in interface for 1.set

t/B	Shear stress τ_y [Pa] in Gauss points			
	1	2	3	4
$1 \cdot 10^{-1}$	$-8.572 \cdot 10^{-2}$	$-2.278 \cdot 10^{-2}$	$1.162 \cdot 10^{1}$	$1.162 \cdot 10^{1}$
$1 \cdot 10^{-2}$	$-2.421 \cdot 10^{-1}$	$-2.414 \cdot 10^{-1}$	$1.265 \cdot 10^{1}$	$1.265 \cdot 10^{1}$
$1 \cdot 10^{-3}$	$-2.450 \cdot 10^{-8}$	$-2.450 \cdot 10^{-7}$	$1.273 \cdot 10^{1}$	$1.273 \cdot 10^{1}$
$1 \cdot 10^{-6}$	no convergence	no convergence	no convergence	no convergence

Table A.17: Shear stress in interface for 2.set

t/B	Shear stress τ_y [Pa] in Gauss points			
	1	2	3	4
$1 \cdot 10^{-1}$	$-1.525 \cdot 10^{-1}$	$-8.579 \cdot 10^{-2}$	$1.160 \cdot 10^{1}$	$1.167 \cdot 10^{1}$
$1 \cdot 10^{-2}$	$-2.469 \cdot 10^{-1}$	$-2.462 \cdot 10^{-1}$	$1.265 \cdot 10^{1}$	$1.265 \cdot 10^{1}$
$1 \cdot 10^{-3}$	$-2.455 \cdot 10^{-8}$	$-2.455 \cdot 10^{-7}$	$1.273 \cdot 10^{1}$	$1.273 \cdot 10^{1}$
$1 \cdot 10^{-6}$	no convergence	no convergence	no convergence	no convergence

Table A.18: Shear stress in interface for 3.set

t/B	Shear stress τ_y [Pa] in Gauss points			
	1	2	3	4
$1 \cdot 10^{-1}$	$7.799 \cdot 10^{-2}$	$1.287 \cdot 10^{-1}$	$9.513 \cdot 10^{0}$	$9.564 \cdot 10^{0}$
$1 \cdot 10^{-2}$	$-2.409 \cdot 10^{-1}$	$-2.401 \cdot 10^{-1}$	$1.235 \cdot 10^{1}$	$1.235 \cdot 10^{1}$
$1 \cdot 10^{-3}$	$-2.452 \cdot 10^{-8}$	$-2.452 \cdot 10^{-7}$	$1.269 \cdot 10^{1}$	$1.269 \cdot 10^{1}$
$1 \cdot 10^{-6}$	no convergence	no convergence	no convergence	no convergence

Multifreedom Constraints - MFC B

This appendix introduces the procedure for implementing the Lagrange multiplier adjunction and the penalty method in Finite Element Method. Felippa [2004] is used as a source.

Multifreedom constrains are functional equations that connect *two or more* displacement components, in such a manner:

$$\boxed{F(\text{Nodal displacement components}) = \text{prescribed value}} \tag{B.1}$$

where the function F disappears if all its nodal displacement arguments do. A MFC of this form is called *multipoint* or *multinode* if it involves displacement components at different nodes. The constraint is called *linear* if all displacement components appear linearly on the left-hand-side of Equation (B.1), thus *nonlinear* otherwise.

The constraint is called *homogeneous* if while transferring all the terms that are dependant of the displacement from the right-hand-side over to the left-hand. Thereby leaving the "prescribed values" in Equation (B.1) to be equal to zero. Otherwise, the constraints are called *non-homogeneous*.

B.1 Methods for imposing Multifreedom Constraints

So that the multifreedom constraints are accounted for, the assembled master stiffness equation is changed into a modified system of equations, shown in Equation (B.2):

$$\mathbf{K}\,\mathbf{u} = \mathbf{f} \quad \stackrel{\text{MFC}}{\Longrightarrow} \quad \hat{\mathbf{K}}\,\hat{\mathbf{u}} = \hat{\mathbf{f}} \tag{B.2}$$

The modification process, Equation (B.2), is also called *constraint application.* The modified system is then implemented into the equation solver, that returns $\hat{\mathbf{u}}$. The procedure for solving the MFCs is presented in Figure B.1.

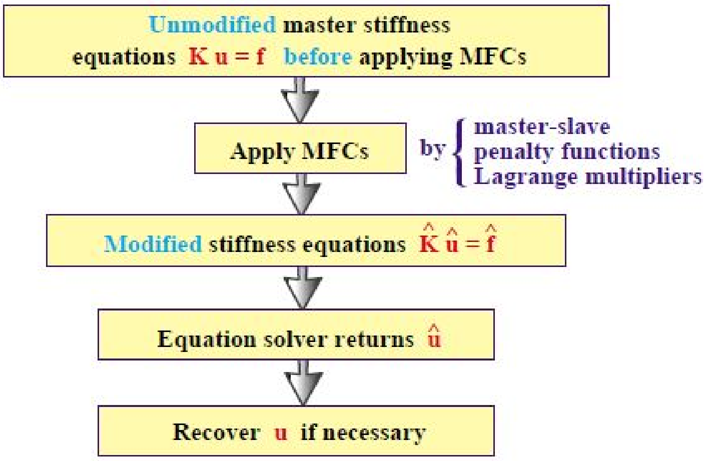

Figure B.1: Flowchart for MFC application, Felippa [2004]

The methods used in the MFC application is briefly explained below:

1. *Master-Slave Elimination*
   The degrees of freedom involved in each MFC are separated into master and slave freedoms. The slave freedoms are then eliminated and the modified equations do not contain the slave freedoms.

2. *Penalty Augmentation* also called penalty function method.
   Each MFC is considered as a elastic artificial structural element called *penalty element*. This element is dependent on a numerical weight. The MFCs are imposed by augmenting the finite element model with the penalty elements.

3. *Lagrange Multiplier Adjuction*
   For each MFC an unknown is added to the master stiffness equations. Physically, the additional unknows represent the constraint forces that would enforce the constraints exactly should they be applied to the constraint system.

Matrix forms of MFCs is convenient for compact notation. All multifreedom constraints are expressed a single matrix relation, shown in Equation (B.3)

$$\mathbf{A}\,\mathbf{u} = \mathbf{g} \tag{B.3}$$

where rectangular matrix $\mathbf{A}$ is formed by arranging a_i's as rows and columns that represents the constraints as a row vector. The $\mathbf{u}$ is formed by u_i that is a column vector that collects the degrees of freedom that participates in the constraints and $\mathbf{g}$ is formed by a column vector of g_i that represents the right-hand-side scalar.

B.2 Master-Slave Method

Each MFC is considered one at the time, and for each constraint a slave degree of freedom is chosen. The degrees of freedom that remains in the constraint is called masters. A new set of degrees of freedom $\hat{\mathbf{u}}$ is created by removing the slave degrees of freedom in $\mathbf{u}$. This new vector contains master degrees of freedom, including those that do not appear in the MFCs. Thereafter, a matrix transformation equation that relates $\mathbf{u}$ to $\hat{\mathbf{u}}$ is generated. This equation is used to apply a appropriate transformation to the master stiffness equations. This procedure yields a set of modified stiffness equations that are expressed in terms of the new degrees of freedom set $\hat{\mathbf{u}}$. Because the modified system does not contain the slave degrees of freedoms, these have been eliminated.

B.2.1 The General case

The master-slave method for general programs can be described as follows in Equation (B.4):

$$\begin{bmatrix} K_{uu} & K_{um} & K_{us} \\ K_{um}^T & K_{mm} & K_{ms} \\ K_{us}^T & K_{ms}^T & K_{ss} \end{bmatrix} \begin{Bmatrix} u_u \\ u_m \\ u_s \end{Bmatrix} = \begin{Bmatrix} f_u \\ f_m \\ f_s \end{Bmatrix} \tag{B.4}$$

where the degrees of freedoms in $\mathbf{u}$ is divided into three types: independent or unconstrained, masters and slaves. The degrees of freedoms are represented as $\mathbf{u_u}$, $\mathbf{u_m}$ and $\mathbf{u_s}$, respectively. The MFCs may be written in matrix form shown in Equation (B.5).

$$\mathbf{A_m}\,\mathbf{u_m} + \mathbf{A_s}\,\mathbf{u_s} = \mathbf{g_A} \tag{B.5}$$

where $\mathbf{A_s}$ is assumed square and nonsingular. If so, it is possible to solve for the slave freedoms following Equation (B.6):

$$\mathbf{u_s} = \mathbf{A_s^{-1}}\,\mathbf{A_m}\,\mathbf{u_m} + \mathbf{A_s^{-1}}\,\mathbf{g_A} \overset{\text{def}}{=} \mathbf{T}\,\mathbf{u_m} + \mathbf{g} \tag{B.6}$$

Inserting Equation (B.6) into Equation (B.5), and due to symmetry it yields Equation (B.7):

$$\begin{bmatrix} K_{uu} & K_{um} + K_{us}\,T \\ K_{um} + K_{us}\,T & K_{mm} + T^T\,K_{ms}^T + K_{ms} + T + T^T\,K_{ss}\,T \end{bmatrix} \begin{Bmatrix} u_u \\ u_m \end{Bmatrix} = \begin{Bmatrix} f_u - K_{us}\,g \\ f_m - K_{ms}\,g \end{Bmatrix} \tag{B.7}$$

Figure B.2 shows a bar with seven nodes. The process of the elimination of the slaves is presented in three stages.

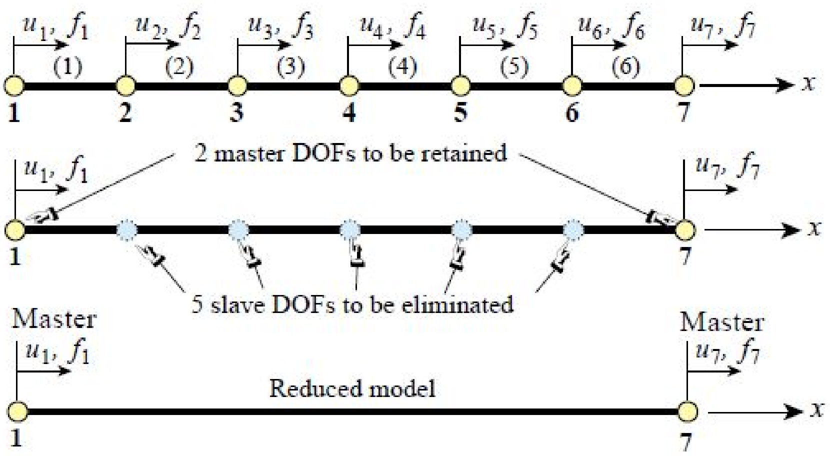

Figure B.2: Model where the slave reduction is present, Felippa [2004]

B.3 The penalty function method

The master-slave method previously explained has shortcomings considering arbitrary constraints. In this chapter the two methods the penalty method and Lagrange multiplier adjunction are studied. Both these techniques are considered a good implementation of the Finite Element Method for both linear and nonlinear.

B.3.1 Physical interpretation of the penalty function method

In this section a one-dimensional 6 bar finite element where the 7 nodes may move in the x-direction is considered. To connect node 2 and node 6 such that $u_2 = u_6$ it is imagined that the nodes are connected with a large additional bar of axial stiffness w. The additional bar is named element 7, as shown in Figure B.3. Element 7 is called a penalty bar and w is its penalty weight.

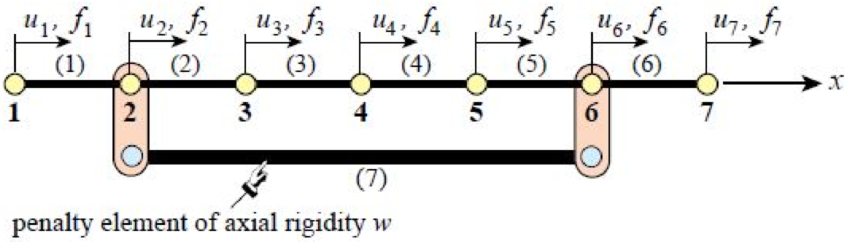

Figure B.3: Adjunction of a fictions penalty bar of axial stiffness w, where $u_2 = u_6$, Felippa [2004]

Such an element can be treated as any other bar element, as the assembly of the master stiffness equations. The penalty element stiffness equations, $[\mathbf{K}^{(7)}]\left\{\mathbf{u}^{(7)}\right\} = \left\{\mathbf{f}^{(7)}\right\}$, are written as Equation B.8:

$$w\begin{bmatrix} 1 & -1 \\ -1 & 1 \end{bmatrix}\begin{Bmatrix} u_2 \\ u_6 \end{Bmatrix} = \begin{Bmatrix} 0 \\ 0 \end{Bmatrix} \tag{B.8}$$

Thereafter, the global system is assembled together with the local system of the penalty, where the only change is an increase in stiffness, demonstrated in Equation (B.9).

$$\begin{bmatrix} K_{11} & K_{12} & 0 & 0 & 0 & 0 & 0 \\ K_{12} & K_{22}+w & K_{23} & 0 & 0 & -w & 0 \\ 0 & K_{23} & K_{33} & K_{34} & 0 & 0 & 0 \\ 0 & 0 & K_{34} & K_{44} & K_{45} & 0 & 0 \\ 0 & 0 & 0 & K_{45} & K_{55} & K_{56} & 0 \\ 0 & -w & 0 & 0 & K_{56} & K_{66}+w & K_{67} \\ 0 & 0 & 0 & 0 & 0 & K_{67} & K_{77} \end{bmatrix}\begin{Bmatrix} u_1 \\ u_2 \\ u_3 \\ u_4 \\ u_5 \\ u_6 \\ u_7 \end{Bmatrix} = \begin{Bmatrix} f_1 \\ f_2 \\ f_3 \\ f_4 \\ f_5 \\ f_6 \\ f_7 \end{Bmatrix} \tag{B.9}$$

B.3.2 Choosing the penalty weight

In this section the numerical integration of Equation (B.9) is investigated. Thus if a *finite* weight w is chosen, the constraint $u_2 = u_6$ is approximately satisfied in the sense that it yields $u_2 - u_6 = e_g$, where $e_g \neq 0$. The "gap error", e_g, is called *constraint violation.*

The magnitude of $|e_g|$ highly depends on finite weight w. More precisely, the larger w the smaller the violation.

Thereafter, the correct strategy seems like it would be to choose the largest w possible, but however this is misleading. As the penalty weight w increases towards the infinity ∞, the modified stiffness matrix from Equation (B.9) comes more and more in conflict with the respect to inversion conditions.

B.3.3 The square root rule

As mentioned in the previous section, by making w reduces the constraint violation error, but inconveniently also increases the solution error. It is concluded that the best w is that which makes both errors roughly equal in absolute value. The procedure to to find this absolute value is challenging while systematically running numerical experiments. In practice, the heuristic *square root rule* is often followed.

The rule is presented as follows. Imagine that the largest stiffness coefficient, before adding penalty elements, is in the order of 10^k and that the working machine precision is p digits. Such order-of-magnitude estimates can be readily found by scanning the diagonal of $\mathbf{K}$ because the largest stiffness coefficient of the actual structure is usually a diagonal entry. Thereafter, choose the penalty weights to be in the order of $10^{k+p/2}$ with the condition that the choice would not cause arithmetic overflow. If overflow occurs, the master stiffness should be scaled throughout or a better choice of physical units made.

A short example if the square root rule is presented. Following that $k \approx 0$ and $p \approx 16$, the optimal w would be $w \approx 10^8$. This w would yield a constraint violation and solution error of order 10^{-8}.

B.3.4 Penalty elements for general Multi Freedom Constraints (MFC)

For the constraints presented in previous section $u_2 = u_6$, the physical interpretation of the penalty element is quite straight forward. The nodal points 2 and 6 are connected and are obliged to move together along the x-axis, which can be approximately implemented by the penalty bar, element 7, shown in Figure B.3.

The procedure of more general constraints is linked to the theory of *Courant penalty functions*, which is a topic in variational calculus. A recipe of constructing a penalty element is stated here. Consider the homogeneous constraint (B.10):

$$3u_3 + u_5 - 4u_6 = 0 \tag{B.10}$$

1. Rewrite Equation (B.10) into matrix form

$$\begin{bmatrix} 3 & 1 & -4 \end{bmatrix} \begin{bmatrix} u_3 \\ u_5 \\ u_6 \end{bmatrix} = 0 \tag{B.11}$$

2. Pre-multiply both sides by the transpose of the coefficient matrix maybe write the equation
3. The unscaled stiffness matrix of the penalty element is multiplied by the penalty weight w ans assembled into the master stiffness matrix following the usual rules.

If the constraints is non-homogeneous, the force vector is also modified.

B.3.5 The theory behind the penalty method

The following is based on mathematical theory. Suppose we have a set of m linear MFCs. These will be stated as:

$$\mathbf{a_p}\,\mathbf{u} = b_p \quad p = 1, \dots m \tag{B.12}$$

where $\mathbf{u}$ contains all degrees of freedom and $\mathbf{a_p}$ is a row vector with same length as $\mathbf{u}$. To incorporate the MFCs into the FEM model, a weight $w_p > 0$ is selected for each constraints. Thus the Courant quadratic penalty function or "penalty energy" is constructed, P.

$$P = \sum_{p=1}^{m} P_p, \qquad \text{with} \qquad P_p = \frac{1}{2}\mathbf{u^T}\,\mathbf{K^{(p)}} - \mathbf{u^T}\,\mathbf{f^{(p)}} \tag{B.13}$$

Thereafter, a P is added to the potential energy function $\prod = \frac{1}{2}\,\mathbf{u^T}\,\mathbf{K}\,\mathbf{u} - \mathbf{u^T}\,\mathbf{f}$ to form the augmented potential energy $\prod_a = \prod + P$. Minimization of $\prod_a$ with respect to $\mathbf{u}$ yields:

$$\left(\mathbf{K}\,\mathbf{u}\sum_{\mathbf{p=1}}^{\mathbf{m}}\mathbf{K^{(P)}}\right)\,\mathbf{u} = \mathbf{f} + \sum_{\mathbf{p=1}}^{\mathbf{m}}\mathbf{f^{(P)}} \tag{B.14}$$

Each term of the sum of p, which derives from term P_p in Equation (B.13) may be viewed as contributed by a penalty element with globalized stiffness matrix, $\mathbf{K^P}$ and globalized added force term $\mathbf{f^{(p)}}$.

To use a more compact form of notation, the penalty augmented system can be written as the set of multifreedom constraints yielding:

$$(\mathbf{K} + \mathbf{A^T}\,\mathbf{W}\,\mathbf{A})\,\mathbf{u} = \mathbf{f} + \mathbf{W}\,\mathbf{A^T}\,\mathbf{b}, \tag{B.15}$$

where $\mathbf{W}$ is a diagonal matrix of penalty weights. However, this compact form of notation conceals the configuration of the penalty elements.

B.3.6 Evaluation of the Penalty Method

The main advantage is that it is easy to implement it into the computer. When considering the modified system, the $\mathbf{u}$ and $\hat{\mathbf{u}}$ stays the same, while only the stiffness matrix $\mathbf{K}$ change. Once all the elements are assembled, the system can be passed through the equation solver.

An important advantage is also that the penalty method is easily extendable to nonlinear constraints.

The main disadvantage, however, is a serious: the choice of weight values that balance solution accuracy with the violation of constraint conditions. For the more simple cases, the square root rule can be used, but that requires that the information of the magnitude of the stiffness program is known. Such information may be difficult to extract. For more difficult cases, the choice of weights may require extensive amount of numerical experimentation.

Plasticity theory C

In this appendix the plastic behavior of the material and plastic strains will be described. The theory takes its bases from Ottosen and Ristinmaa [2005].

Plasticity theory is applied with time-independent behavior that is nonlinear and where strains exist when the material is unloaded, also known as residual strains. in Appendix F, the condition for where the plastic effects are initiated, referred to as yield criterion. When the stress states exceeds the yield criterion, the plastic strains will develop and this will be discussed in this chapter.

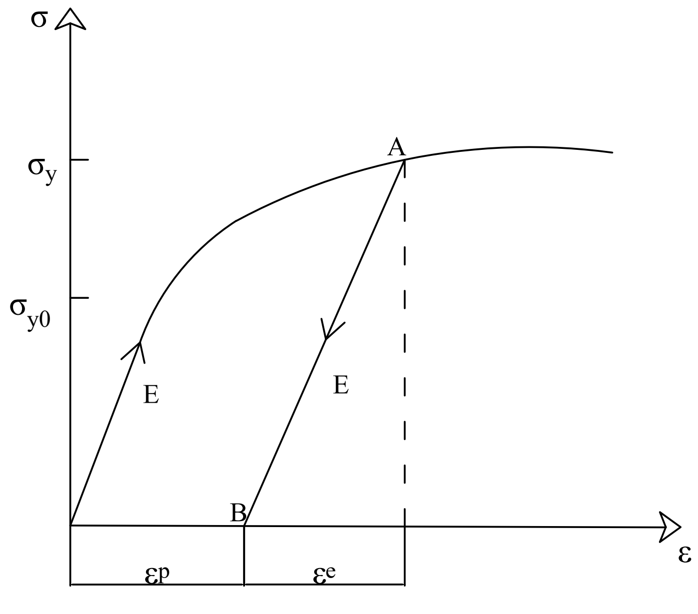

Figure C.1: Basic response of elastoplastic material

The basic behavior of an elastoplastic material is illustrated in Figure C.1. The material behaves linear elastically with stiffness E, until the initial yield stress σ_{y0} is reached. Then σ_{y0} is passed, plastic strains develop. Thereafter, unload from point A occurs elastically with stiffness E so that at complete unloading to point B, the residual strain yields the plastic strain ε^p developed at point A. Therefore, at point A, the total strain consists of the sum of the elastic strains and the plastic strains, defining Equation (C.1):

$$\varepsilon = \varepsilon^e + \varepsilon^p \tag{C.1}$$

If reloading occurs again from point B, the material reacts elastically until the stresses reach the value of σ_y at point A. The value of σ_y is therefore actling as the current yield stress. Furthermore, on loading beyond point A the material behaves as the previous unloading have not occurred. Moreover, the response illustrated in Figure C.1 is assumed to be independent of time, meaning that the same response irrespective of the loading rate is obtained. To characterize plastic behavior, several of idealized responses have been defined.

C.1 Fundamental equations

Equation (C.1) can also be expressed by Equation (C.2):

$$\dot{\varepsilon}_{ij} = \dot{\varepsilon}^e_{ij} + \dot{\varepsilon}^p_{ij} \tag{C.2}$$

where the dot denotes the time rate. The elastic strains are determined from Hooke's law, shown in Equation (C.3):

$$\sigma_{ij} = D_{ijkl}\left(\varepsilon_{kl} - \varepsilon^p_{kl}\right) \tag{C.3}$$

Due to the symmetry of σ_{ij} and ε_{ij}, D_{ijkl} possesses the usual symmetry properties. Assuming the tensor D_{ijkl} is constant with respect to loading, it is possible to obtain Equation (C.4) from Equation (C.3).

$$\dot{\sigma}_{ij} = D_{ijkl}\left(\dot{\varepsilon}_{kl} - \dot{\varepsilon}^p_{kl}\right) \tag{C.4}$$

The presence of a yield function $f(\sigma_{ij}, K_\alpha)$ is assumed so that development of plastic strains requires that Equation (C.5) is fulfilled.

$$f(\sigma_{ij}, K_\alpha) = 0 \qquad \textit{for development of plasticity} \tag{C.5}$$

where K_α represents the hardening parameter, which may be scalars of higher order tensors. Due to that $\alpha = 1, 2, \ldots$ there may be one, two or more hardening parameters present. By this, if the current yield surface is considered which for $K_\alpha = 0$ reduces to the initial yield surface $F(\sigma_{ij})$.

The state of material is described by the internal variables, that may be scalars or higher order tensors, denoted κ_α. Generally, the only quantities that can be directly measured or observed are total strains ε_{ij} and the temperature, defining κ_α as non-observant variables. The internal variables κ_α memorize the plastic loading history of the material. An example of a internal variable is the effective plastic strain. For elastoplastic material, the internal variables can be characterized as in Equation (C.6):

$$K_\alpha = K_\alpha(\kappa_\beta) \tag{C.6}$$

where $\beta = 1, 2, \ldots$. In Equation (C.6) the number of hardening parameters are equal to the number of internal variables. Similarly to the yield function, the presence of the potential function g is defined by Equation (C.7):

$$g(\sigma_{ij}) = g(\sigma_{ij}, K_\alpha) \tag{C.7}$$

Equation (C.7) shows that potential function depends on the same parameters as the yield function.

The corresponding flow rule is expressed in Equation (C.8):

$$\dot{\varepsilon}_{ij}^{p} = \dot{\lambda}\,\frac{\partial g}{\partial \sigma_{ij}}; \qquad \dot{\lambda} \geq 0 \tag{C.8}$$

In case of, $f = g$ associated plasticity occurs, while in case of $g \neq f$ non-associated plasticity holds. The flow rule describes the direction of the plastic strain rate $\dot{\varepsilon}_{ij}^{p}$, given by the gradient $\partial g/\partial \sigma_{ij}$, while the plastic multiplier $\dot{\lambda}$ describes the magnitude of the plastic strain rate. Furthermore, if $\dot{\lambda} = 0$, no plastic strain develop, whereas if $\dot{\lambda} > 0$, the plastic multiplier guarantees that the plastic strain and the gradient possesses the same direction.

Throughout the development of plastic strains, the consistency relation states that the yield criterion is fulfilled, shown in Equation (C.9):

$$\dot{f} = \frac{\partial f}{\partial \sigma_{ij}}\,\dot{\sigma}_{ij} + \frac{\partial f}{\partial K_{\alpha}}\,\dot{K}_{\alpha} = 0 \tag{C.9}$$

where $\dot{K}_{\alpha}$ can be obtained from Equation (C.6) as shown in Equation (C.10):

$$\dot{K}_{\alpha} = \frac{\partial K_{\alpha}}{\partial \kappa_{\beta}}\,\dot{\kappa}_{\beta} \tag{C.10}$$

where $\dot{\kappa}_{\alpha}$ are obtained by the so called evolution law, expressed in Equation (C.11):

$$\dot{\kappa}_{\alpha} = \dot{\lambda}\,k_{\alpha}\,(\sigma_{ij}, K_{\beta}) \tag{C.11}$$

where the evolution functions k_{α} are allowed to depend on the same variables as the yield function and the potential function and shows that no internal variables change when $\dot{\lambda} = 0$ which means, by the flow rule, that no plastic strains develop. This shows the evolution law for the yield surface.

In summation, to obtain a specific plasticity model it is required to choose the yield function f, the potential function g, the hardening parameters K_{α} and the internal variables. The choice of hardening parameters implies the choice of hardening rule. The plasticity model chosen for this project is the elastic perfectly-plastic which will be describes more detailed in Appendix D.

C.2 Plastic modulus

As mention in Section C.1, the flow rule determines the direction of the plastic strain rates, however the magnitude of the plastic multiplier is unknown. For determination of $\dot{\lambda}$, the consistency relation and $\dot{\kappa}_{\alpha}$ are used, yielding Equation (C.12):

$$\dot{K}_{\alpha} = \dot{\lambda}\,\frac{\partial K_{\alpha}}{\partial \kappa_{\beta}}\,k_{\beta} \tag{C.12}$$

By inserting Equation (C.12) into Equation (C.9), it provides Equation (C.13):

$$\frac{\partial f}{\partial \sigma_{ij}}\,\dot{\sigma}_{ij} - H\,\dot{\lambda} = 0; \qquad H = -\frac{\partial f}{\partial K_{\alpha}}\,\frac{\partial K_{\alpha}}{\partial \kappa_{\beta}}\,k_{\beta} \tag{C.13}$$

where H is the generalized plastic modulus. It is possible now to determine the plastic multiplier by Equation (C.14), if $H \neq 0$:

$$\dot{\lambda} = \frac{1}{H} \frac{\partial g}{\partial \sigma_{ij}} \frac{\partial f}{\partial \sigma_{kl}} \dot{\sigma}_{kl} \tag{C.14}$$

This can then be substituted into the flow rule and the stress driven format is obtained in Equation (C.15), where the increment stresses describes the incremental plastic strains:

$$\dot{\varepsilon}^{p}_{ij} = \frac{1}{H} \frac{\partial g}{\partial \sigma_{ij}} \frac{\partial f}{\partial \sigma_{kl}} \dot{\sigma}_{kl} \qquad \text{for} \qquad H \neq 0 \tag{C.15}$$

C.3 Elastoplastic stiffness

The stress driven format for obtaining the plastic strains from Equation (C.15) is used to retrieve the constitutive flexibility tensor for elasto-plasticity. Combining Equation (C.2) with Equation (C.4), yields Equation (C.16):

$$\dot{\varepsilon}_{ij} = C_{ijkl}\, \dot{\sigma}_{kl} \tag{C.16}$$

C_{ijkl}	Elastic flexibility tensor.

A combination of Equation (C.2), Equation (C.15) and Equation (C.16), gives Equation (C.17):

$$\dot{\varepsilon}^{e}_{ij} = C^{ep}_{ijkl}\, \dot{\sigma}_{kl} \qquad \text{where} \qquad C^{ep}_{ijkl} = C_{ijkl} + \frac{1}{H} \frac{\partial g}{\partial \sigma_{ij}} \frac{\partial f}{\partial \sigma_{kl}} \tag{C.17}$$

Thus, if $H \neq 0$ and if the stress state $\dot{\sigma}_{kl}$ is known, then Equation (C.17) determines the response completely. This formulation form the so called stress driven format.

For it to be possible to determine the response for a general case, if $H = 0$, the total strain rate $\dot{\varepsilon}_{ij}$ and not the prescribes stress state $\dot{\sigma_{ij}}$ needs to be given. To obtain this general format, the flow rule in Equation (C.8) is inserted into Hooke's law in Equation (C.4), yielding (C.18):

$$\dot{\sigma}_{ij} = D_{ijkl}\, \dot{\varepsilon}_{kl} - \dot{\lambda}\, D_{ijst} \frac{\partial g}{\partial \sigma_s t} \tag{C.18}$$

Equation (C.18) is then multiplied by $\partial f / \partial \sigma_{ij}$ and then use Equation (C.13), Equation (C.19): is obtained for the plastic multiplier:

$$\dot{\lambda} = \frac{1}{A} \frac{\partial f}{\partial \sigma_{ij}} D_{ijkl}\, \dot{\varepsilon}_{kl} \qquad \text{where} \qquad A = H + \frac{\partial f}{\partial \sigma_{ij}} D_{ijkl} \frac{\partial g}{\sigma_{kl}} \tag{C.19}$$

For it to be possible to derive Equation (C.19), $A > 0$ can always be assumed. Combining the results of the plastic multiplier and the formulation for Hooke's Law in Equation (C.16), the strain driven format is found Equation (C.20):

$$\dot{\sigma}_{ij} = D^{ep}_{ijkl}\, \dot{\varepsilon}_{kl} \qquad \text{where} \qquad D^{ep}_{ijkl} = D_{ijkl} - \frac{1}{A} D_{ijst} \frac{\partial g}{\partial \sigma_{st}} \frac{\partial f}{\partial \sigma_{mn}} D_{mnkl} \tag{C.20}$$

where D^{ep}_{ijkl} represents the *elastoplastic stiffness tensor* and Equation (C.20) comprises the so called strain driven format.

D Linear elastic perfectly-plastic constitutive model

This appendix account for the theory of linear elastic perfectly-plastic that is the material behavior used. The theory takes its basis from Ottosen and Ristinmaa [2005] and PLAXIS [2016].

A perfectly-plastic model is a constitutive model with a fixed yield surface, which means a yield surface that is fully defined by model parameters and not affected by plastic straining.

The basic principle of elastoplastisity is that the strains and strain rates are divided into an elastic part and a plastic part, shown in Equation (D.1):

$$\varepsilon = \varepsilon^e + \varepsilon^p \qquad\qquad \dot{\varepsilon} = \dot{\varepsilon^e} + \dot{\varepsilon^p} \tag{D.1}$$

Following is the Hooke's law used to relate the stress rates to the elastic strain rates. Hence, substituting Equation (D.1) into Hooke's law yields Equation (D.2):

$$\dot{\sigma'} = \dot{D^e}\,\dot{\varepsilon^e} = \dot{D^e}\,\dot{\varepsilon} - \dot{\varepsilon^p} \tag{D.2}$$

In accordance with classical plasticity theory, plastic strain rates are proportional to the derivative of the yield function with respect to the stresses. This means that the plastic strain rates can be describes as vectors perpendicular to the yield surface. This is called associated plasticity. However, when using the Mohr-Coulomb yield functions, the theory of the theory of associated plasticity may overestimate the dilatancy. To avoid this, an plastic potential function g is introduced in addition to the yield function. Hence, by $f \neq g$ it is refered to as non-associated plasticity.

Generally, the plastic strain rates are defined as in Equation (D.3):

$$\dot{\varepsilon} = \lambda \frac{\partial g}{\partial \sigma'} \tag{D.3}$$

λ	Plastic multiplier

For purely elastic behavior $\lambda = 0$, while in the case of plastic behavior $\lambda > 0$. The relations are shown in Equations (D.4) and (D.5):

$$\lambda = 0 \qquad \text{for:} \qquad f < 0 \qquad \text{or:} \qquad \frac{\partial f^T}{\partial \sigma'} D^e\,\dot{\varepsilon} < 0 \qquad \text{Elastic} \tag{D.4}$$

$$\lambda > 0 \qquad \text{for:} \qquad f = 0 \qquad \text{or:} \qquad \frac{\partial f^T}{\partial \sigma'} D^e\,\dot{\varepsilon} = 0 \qquad \text{Plastic} \tag{D.5}$$

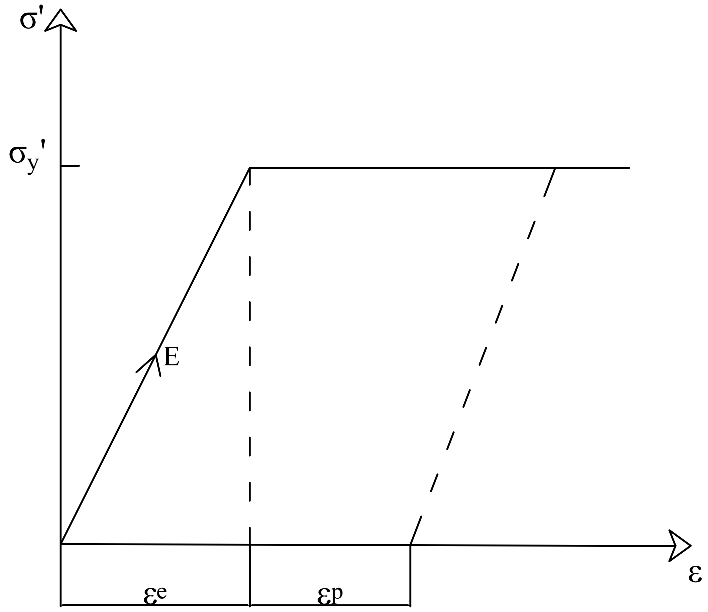

Figure D.1: Elastic perfectly plastic material model

The Equations (D.4) and (D.5) can be used to create a relationship between the effective stress rate and the strain rates for elastic perfectly-plastic behavior, shown in Equation (D.6):

$$\dot{\sigma'} = \left(D^e - \frac{\alpha}{d}\, D^e\, \frac{\partial g}{\partial \sigma'}\, \frac{\partial f^T}{\partial \sigma'}\, D^e \right) \dot{\varepsilon} \tag{D.6}$$

where:

$$d = \frac{\partial f^T}{\partial \sigma'}\, D^e\, \frac{\partial g}{\partial \sigma'}$$

The parameter α is used to switch between an elastic behavior, $\alpha = 0$, and plastic behavior, $\alpha = 1$.

The theory of plasticity above is restricted to smooth yield surfaces and does not cover the multiple types of yield surfaces present in the Mohr-Coulomb model. In this case, the theory of plasticity has been extended to account for flow peaks involving two or more potential functions, as expressed in Equation (D.7):

$$\dot{\varepsilon^p} = \lambda_1\, \frac{\partial g_1}{\partial \sigma_1} + \lambda_2\, \frac{\partial g_2}{\partial \sigma_2} + \dots \tag{D.7}$$

Similarly, several yield functions $(f_1, f_2, \dots)$ are used to determine the plastic multipliers $(\lambda_1, \lambda_2, \dots)$.

Nonlinear Finite Element E

In this appendix, the concept of nonlinear problems is described. Following, a presentation of different solution methods. The theory in this Appendix takes its source from Cook et al. [2002] and Ottosen and Ristinmaa [2005].

For linear problems in Finite Elements the solution method are fairly straightforward. Elastoplastic problems nevertheless are nonlinear and raise questions that must be solved before reliable results can be reached. Thus, it is necessary to account for new formulation of the nonlinear finite element method as well as solutions of the nonlinear equilibrium equations. Foremost, a formulation of general nonlinear problems based on virtual work. Furthermore, the equations of motions and static conditions are described.

E.1 Equations of motion

Firstly, the equations of motion in finite element format by the weak format is express as:

$$\int_V \rho\, \nu_i\, \ddot{u}_i\, dV + \int_V \varepsilon^v_{ij}\, \sigma_{ij}\, dV = \int_S \nu_i\, t_i\, dS + \int_V \nu_i\, b_i\, dV \tag{E.1}$$

ν_i	Arbitrary weight vector
t_i	Traction vector
b_i	Body force (force pr unit volume)
$\ddot{u}_i$	Acceleration vector
ε^v_{ij}	Strain tensor related to ν_i
σ_{ij}	Stress tensor

It is possible to rewrite this weak from into matrix form which is convenient considering finite element formulation. Thus, Equation (E.1) is rewritten as:

$$\int_V \rho\, \nu^T\, \ddot{u}\, dV + \int_V (\varepsilon^v)^T\, \sigma\, dV = \int_S \nu^T\, t\, dS + \int_V \nu^T\, b\, dV \tag{E.2}$$

The boundary conditions can be expressed as that the displacement vector u is prescribed along the boundary surface S_u and the traction vector t is prescribed along the boundary surface S_t, whereas the total boundary is composed of the sum of the two boundary surfaces.

The finite element method is based on the concept that the displacement vector u, can be expressed by the global shape functions N and nodal displacements a of the body, shown in Equation (E.3):

$$u = N\, a \tag{E.3}$$

Given by Equation (E.3), the corresponding strains can be derived and used to establish:

$$M\,\ddot{a} + \int_V B^T\,\sigma\,dV = f; \qquad\qquad M = \int_V \rho\,N^T\,N\,dV \tag{E.4}$$

M	Mass matrix
B	Strain interpolation matrix
N	Shape functions

Whereas the force is defined based on external forces shown in:

$$f = \int_S N^T\,t\,dS + \int_V N^T\,b\,dV \tag{E.5}$$

Equation (E.4) is solely derived from equations of motions meaning that it hold for any constitutive relation.

E.2 Static conditions

Considering static conditions, the nodal accelerations $\ddot{a}$ are assumed to be zero. Hence, the equation of motions are reduced to equilibrium equations, shown in:

$$\Psi = 0 \qquad \text{where} \qquad \Psi = \int_V B^T\,\sigma\,dV - f \tag{E.6}$$

As mentioned in Section E.1, the force is an expression of external forces when the loading of the body is given by the traction vector and the body load, while similarly the term $\int_V B^T\,\sigma\,dV$ expresses the internal forces corresponding with the stresses σ. Thus the internal forces must be equal to the external forces.

Following, constitutive relations are applied in order to solve a specific boundary problem. Generally, for nonlinear problems, the solution is quite different than for linear elastic problems. The current stresses σ cannot be expressed directly in terms of the current strains ε. Instead, an incremental relation is drawn between the stress state and the strain rate. For elastoplastic problems, the relation is given as in Equation (C.20) where it is rewritten into matrix form, gives as:

$$\dot{\sigma} = D^{ep}\,\dot{\varepsilon} \tag{E.7}$$

where the current stresses σ must be obtained by integration along the actual load history. The nonlinearity of the constitutive relations in Equation (E.7) results in that also Equation (E.6) becomes nonlinear. Due to that the constitutive relation is incremental, the equilibrium equations are differentiated with respect to time, yielding:

$$\int_V B^T\,\dot{\sigma}\,dV \qquad \text{where} \qquad \dot{f} = \int_S N^T\dot{t}\,dS + \int_V N^T\,\dot{b}\,dV \tag{E.8}$$

From this incremental elastoplastic constitutive relation, it can be rewritten by substitute the expression for incremental strains $\dot{\varepsilon} = B\,\dot{a}$ into Equation (E.7), yielding:

$$\dot{\sigma} = D_t\,B\,\dot{a} \qquad \text{where} \qquad D_t = \begin{cases} D \\ D^{ep} \end{cases} \tag{E.9}$$

Due to that the incremental nodal displacements $\dot{a}$ are independent of position, the use of Equation (E.9) and Equation (E.8), yields:

$$K_t\,\dot{a} = \dot{f} \qquad \text{where} \qquad \dot{f} = \int_V B^T\,D_t\,B\,dV \tag{E.10}$$

It is important to emphasis that the tangential stiffness matrix K_t is not a constant matrix and is composed of a system of nonlinear equations. The external load f increases in small steps and for each of these steps, the corresponding change of nodal displacements $\dot{a}$ is determined by Equation (E.10).

The main essential problem in nonlinear finite element method is to solve the global nonlinear equations in Equation (E.10), where the solution has to ensure that the total equilibrium equation of the body is fulfilled for Equation (E.6). Nevertheless, to use Equation (E.6) the total stresses of the body need to be known beforehand to reach a solution. This requires an integration of the constitutive relations from Equation (E.7). Various solution schemes for solving the global equilibrium equation are presented in the following Section E.3

E.3 Solution methods

In structural mechanics, the types of nonlinearity follows:

- Material nonlinearity
- Contact nonlinearity
- Geometric nonlinearity

Problems in these categories are nonlinear because of the stiffness matrix $[K]$, and maybe the load vector $\{R\}$, becomes functions of displacement or deformation, $\{D\}$, where Equation (E.11) represent structural equations, respectively:

$$[K]\,\{D\} = \{R\} \tag{E.11}$$

$[K]$	Stiffness matrix
$\{D\}$	Displacement vector
$\{R\}$	Load vector

The problem just presented is not immediately solvable for $\{D\}$ because information needed to assemble $[K]$ and $\{R\}$ is unknown beforehand. Therefore, an iterative process is required to obtained $\{D\}$ and its associated $[K]$ and $\{R\}$, in condition that the product $[K]\,\{D\}$ is in equilibrium with $\{R\}$.

In this section some frequently used methods of solving nonlinear problems are stated. Nonlinear problems are solved by nonlinear equations, where the equilibrium equations are referred to as nonlinear equations. The external loading f are assumed to be known. This loading is applied stepwise where the external loading is increased in small steps, this procedure is called *incremental solution procedure*.

In order to interpret procedures as two-dimensional plots of load versus response, solution methods for a special case such as single nonlinear equation $f(u, x) = 0$ and $u = u(x)$ where u is the only dependant variable, are applied. In one-dimensional nonlinear spring analogy, stiffness is a function of u, but a prescribed load is simply a value of P, independent of u. In a multidimensional problem, both $[K]$ *and* $\{R\}$ may be a function of $\{D\}$.

E.3.1 Newton-Raphson scheme

The method of Newton-Raphson scheme can be explain in the way of extracting the root of a polynomial, where a $P - u$ curve is generated as its shape is unknown. If a case of a single force applied to a nonlinear spring is considered, the relation between load and displacement is yield from:

$$k\,u = P \qquad or \qquad (k_0 + k_N)\,u = P \qquad \text{where} \qquad k_N = k_N(u) \tag{E.12}$$

k	Stiffness
u	Displacement
P	Load

In Equation (E.12), it is envisioned that initially $u = 0$. Then a load arbitrary load P_1 is applied and the corresponding displacement u_1 is desired. The initial tangent stiffness k_{t0} and the initial load increment is the load itself, $\Delta P_1 = P_1$ due to the choice to start from zero. Following, the current displacement increment is calculated and the solution is updated by Equation (E.13).

$$k_{t0}\,\Delta u = P \qquad \Delta u = k_{t0}^{-1}\,\Delta P_1 \qquad u_A = 0 + \Delta u \tag{E.13}$$

Equation (E.13) yields u_A, which is the current estimate of the desired result of u_1. Due to that the problem does not exert a force that is in equilibrium with P_1, the current force error is introduced, e_{PA}, yielding:

$$e_{PA} = P_1 - k\,u_A \quad \text{where} \quad k = k(u) \ \ \text{is evaluated using displacement } u_A \tag{E.14}$$

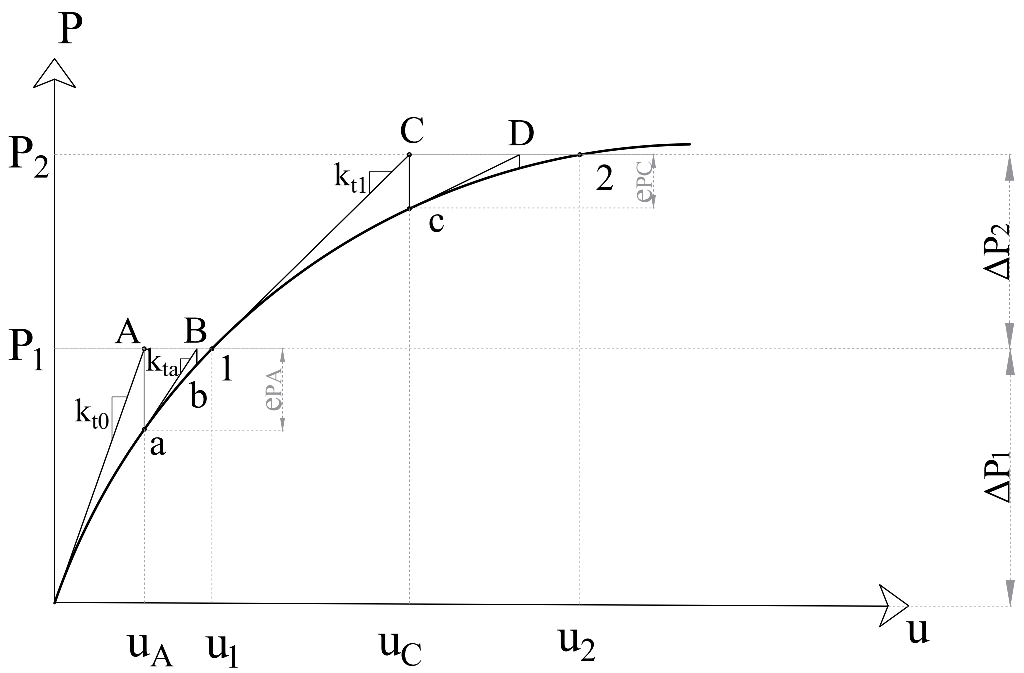

Figure E.1: Newton-Raphson iterations

Following, the equilibrium iterative process begins where the goal is to reduce the current force error to zero. While keeping P_1 constant another step is taken, starting at point a as shown in Figure E.1 and then moving along a tangent to the curve at point a. Then, a more accurate displacement u_B is obtained as:

$$k_{tA}\,\Delta u = e_{PA} \qquad \Delta u = k_{tA}^{-1}\,e_{PA} \qquad u_B = u_A + \Delta u \tag{E.15}$$

with the current force error $e_{?B}$ yielding from Equation (E.16):

$$e_{PB} = P_1 - k\,u_B \quad \text{where} \quad k = k(u) \quad \text{is evaluated using displacement } u_B \tag{E.16}$$

The next step is equivalent to the retirement of the displacement increment Δu and updating displacement from displacement u_A.

This method is not guaranteed to converge for all nonlinear problems. By continuing the iterations causes the force error to decrease that leads to the displacement increment to approach zero, and at last, the updated solution to approach the correct value u_1.

To obtain a sufficient representation of the $P - u$ curve, it is applied on several load levels. By iteration to convergence for each, many points are obtained. The likelihood of convergence to a correct solution of each load level increases by considering small load steps.

E.3.2 Modified Newton-Raphson

The development to modified Newton-Raphson is that the rather than updating the tangent stiffness k_t prior to each calculation of the displacement increment Δu, the same tangent stiffness is used for several iterative processes. The procedure is represented in Figure E.2,

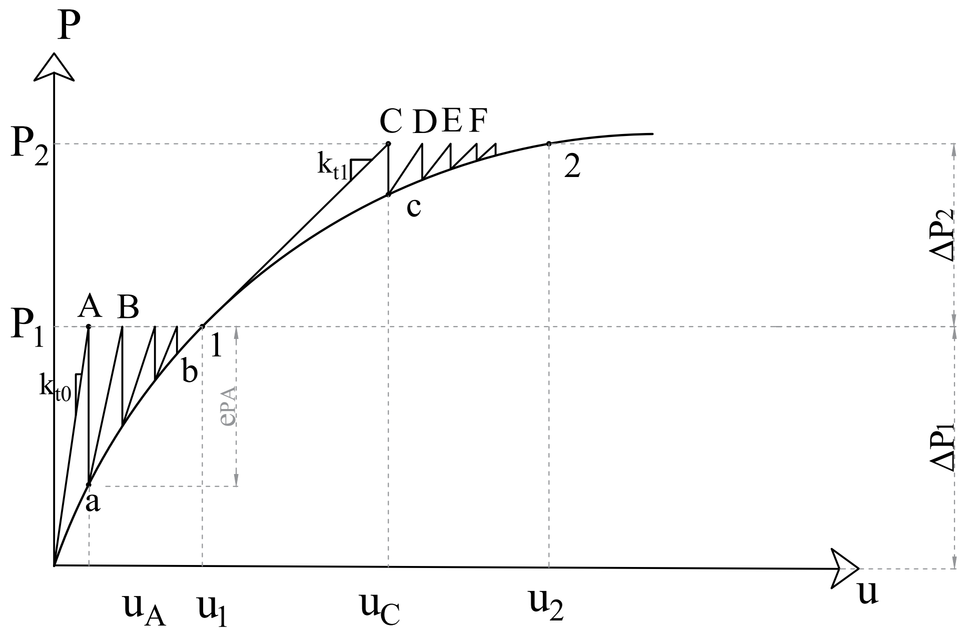

Figure E.2: Modified Newton-Raphson iterations

where is it shown that the initial tangent stiffness k_{t0} is used until convergence at load level P_1. Then the tangent stiffness is updated to k_{t1} and maintained at k_{t1} when convergence at load level P_2 is in process. Modification to the tangent stiffness is needed in Equation (E.13) and for the other evaluated load steps. The main purpose for adopting the modified Newton-Raphson method is cost reduction.

E.3.3 Direct substitution

Direct substitution is considered the most basic solution method. In this method the stiffness matrix is not used, but instead the coefficient matrix is updated and the entire solution is repeated. In the case that $\{R\}$ is constant, it is permitted to start with the initial assumption $\{D\}_0$ for the degrees of freedom. The next step is to establish the corresponding $[K]_0$ and solve for equations $[K]_0\{D\}_1 = \{R\}$ for $\{D\}_1$. Then $[K]_1$ is established based on $\{D\}_1$ and solve for $\{D\}_2$. This process is repeated as many steps that is necessary.

The method is inefficient, and is more likely to encounter convergence difficulties than the tangent stiffness methods.

E.3.4 The initial stiffness method

This solution method uses the stiffness matrix $[\mathrm{K}_0]$ throughout the whole process, regardless of the load level. Nonlinearities are places on the right side of the Equation (E.11) and is repeatedly updated until convergence is achieved.

To apply the same notion as in Equation (E.12), the method is represented by:

$$[K_0]\,\{D\}_i = \{R\} - [K_N]\,\{D\}_{i-1} \quad \text{where} \quad [K] = [K_0] + [K_N] \tag{E.17}$$

$[K_0]$ and $[K_N]$ are respectively constant and displacement-dependant matrices. Due to that $[K_0]$ if the equivalent to $[K_t]$ when the displacements are zero, the initial stiffness matrix is equal to a modified Newton-Raphson method where the stiffness matrix never is updated. Like the method explained above, the initial stiffness method may converge slowly or never depending on the specific problem considered.

Introduction to yield criterion F

In this appendix the criteria of where the material the plastic deformations i.e. yielding of the material or failure occurs is explained. In addition, this appendix accounts for the Haigh-Westergaard coordinate system. The theory in this appendix takes its bases from Ottosen and Ristinmaa [2005].

The conditions for failure or initial yielding are called failure or initial yield criteria respectively. The criterion is a function that is equal to zero when fulfilling the conditions for the failure or initial yielding.

For a homogeneous material with a proportional loaded by a homogeneous stress state with failure or initial yield criterion being independent of the loading rate. The failure of initial yield criterion is only dependent of the stress tensor as shown in:

$$F(\sigma_{ij}) = 0 \tag{F.1}$$

When this condition is fulfilled, initial yielding and failing occur. If the stress state is below zero, $F(\sigma_{ij}) < 0$, the failure has yet to occur, while if $F(\sigma_{ij}) > 0$ the failure already has occurred. These conditions are established in an arbitrary x_i' coordinate system, but for the conditions to be applicable they have to hold when another x_i'-coordinate system is adopted. This implies that the value of F is an invariant.

The stress tensor, σ_{ij}, in Equation (F.1) can also be described by the three principle stresses, σ_1, σ_2 and σ_3, and their corresponding principle stress directions. As an isotropic material does not have directional properties, the yield criterion can be expressed by:

$$F(\sigma_1, \sigma_2, \sigma_3) = 0 \tag{F.2}$$

Determination of the principle stresses require the solution of the eigenvalue problem. However, this can be avoided by expressing the criterion based on the stress invariants. It has been proven more convenient to use the invariants I_1, J_2 and J_3, though $\cos 3\,\theta$ is used instead of J_3. Hence the yield criteion is finally expressed in:

$$F(I_1, J_2, \cos 3\,\theta) = 0 \tag{F.3}$$

One of the advantages of the format in Equation (F.3) is that is separates the influence of the hydrostatic stress I_1 from the influence of the deviatoric stresses expressed by J_2 and $\cos 3\,\theta$ respectively. The following Section F.1 account for how the yield criterion can be illustrated and interpreted.

F.1 Haigh-Westergaard coordinate system

The yield criterion in Equation (F.2) on the previous page can be interpreted in the Cartesian coordinate system as a surface describing when yielding will occur. This is called the Haigh-Westergaard coordinate system, that uses the principle stresses, $\sigma_1, \sigma_2, \sigma_3$, as axes. Furthermore, it is possible to describe the yield criterion related to the stress invariants I_1, J_2 and $\cos 3\,\theta$ as seen on the preceding page in Equation (F.3).

For determining the geometric quantities, an arbitrary point P with $(\sigma_1, \sigma_2, \sigma_3)$ is considered. In the stress space the unit vector, n_i, along the space diagonal as:

$$n_i = \frac{1}{\sqrt{3}}\,(1, 1, 1) \tag{F.4}$$

In the case that the point P is located along the space diagonal, the principle stresses are equal and the space diagonal is therefore called the hydrostatic axis.

For any stress point P, a plane can be located whcich are perpendicular to the hydrostatic axis and that contains the point P. This plane is called the deviatoric plane and it includes the line PN, as shown in Figure F.1: Rather then expressing the position of an arbitrary point by Cartesian coordinates $(\sigma_1, \sigma_2, \sigma_3)$, the coordinates (ξ, ρ, θ) may be used. The coordinate ξ is the distance from origin 0 to the point N, $|\overline{ON}|$. The coordinate ρ represents the distance $|\overline{NP}|$ and θ is tha angle in the deviatoric plane between the projection of the σ_1-axis on the deviatoric plane and the line NP. For describing these coordinates, the unit vector in Equation (F.4) is used. The expression for the coordinate, xi, is expressed by:

$$\xi = n^T\,|\overline{NP}| = \frac{1}{\sqrt{3}}\,\begin{bmatrix}1 & 1 & 1\end{bmatrix}\,\begin{bmatrix}\sigma_1 \\ \sigma_2 \\ \sigma_3\end{bmatrix} \tag{F.5}$$

$$\xi = \frac{I_1}{\sqrt{3}}$$

Likewise, an expression for the coordinate ρ is derived as the length of the vector $\overline{NP}$. This is done on the basis of the deviatoric plane and its stresses s_1, s_2, s_3 which are expresses by:

$$\rho = |\overline{NP}| \qquad \text{where} \qquad \rho^2 = s_1^2 + s_2^2 + s_3^3 \tag{F.6}$$

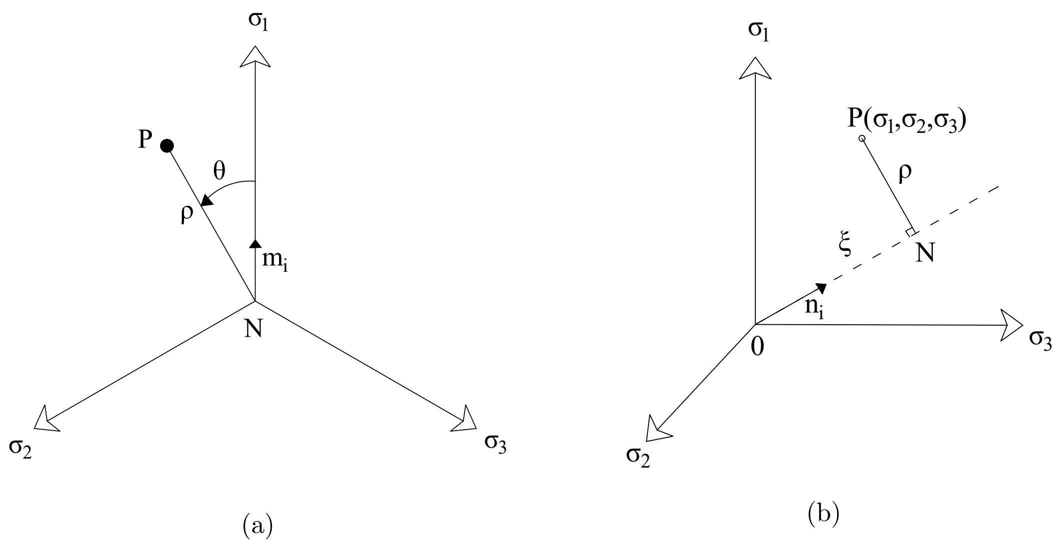

Figure F.1: Haigh-Westergaard coordinate system

$$\rho = \sqrt{2\,J_2}$$

To obtain an expression for the angle θ, some further manipulation needs to be carried out. Thus the angle θ can be expressed by using the invariants J_2 and J_3 in:

$$\cos 3\,\theta = \frac{3\sqrt{3}}{2}\,\frac{J_3}{J_2^{3/2}} \tag{F.7}$$

One of the advantages with this formulation is that the θ is expressed in terms of the stress invariants and not the principle stresses. This implies that the eigenvalue problem does not have to be solved as the stress invariants are obtained directly from the stress tensor. Moreover, the formulation in Equation (F.3) seperates the hydrostatic stress from the influence of the deviatoric stresses expressed by J_2 and $\cos 3\,\theta$. Whereas the invariant J_2 describes the influence of the magnitude of the deviatoric stresses, while the invariant $\cos 3\,\theta$ describes the influence of the direction of the deviatoric stresses.

F.2 Mohr-Coloumb yielding criterion

When considering failure characteristic of concrete, soil and rocks, the description given by:,

$$F(\sigma_1, \sigma_2, \sigma_3) = 0 \tag{F.8}$$

with the convention that

$$\sigma_1 \geq \sigma_2 \geq \sigma_3$$

Generally, obtaining Equation (F.8) is quite complex, and some simplifications have to be performed. This is done by assuming that σ_2 is of insignificant importance, that yields the expression in:

$$F(\sigma_1, \sigma_3) = 0 \tag{F.9}$$

The expression in Equation (F.9) is rewritten into a linear relation between σ_1 and σ_3.

$$k\,\sigma_1 - \sigma_3 - m = 0 \tag{F.10}$$

where k and m are material parameters. This expression in Equation (F.10) is required to predict the uniaxial compressive strength value σ_c, and by implying the stress state $(\sigma_1, \sigma_2, \sigma_3) = (0, 0, -\sigma_c)$, Equation (F.10) is fulfilled, yielding:

$$k\,\sigma_1 - \sigma_3 - \sigma_c = 0 \tag{F.11}$$

This criterion is called the Coulomb criterion and was presented in 1776. Traditionally, the criterion is derived in a different manner. During the derivation of the traditional formulation, Mohr's circle of stress is used. From the center position P and the radius R in Figure F.2a, is given by:

$$P = \frac{1}{2}\,(\sigma_1 + \sigma_3) \qquad\qquad R = \frac{1}{2}\,(\sigma_1 - \sigma_3) \tag{F.12}$$

By the assumption that the stress state fulfills the Coulomb criterion, σ_3 is then isolated

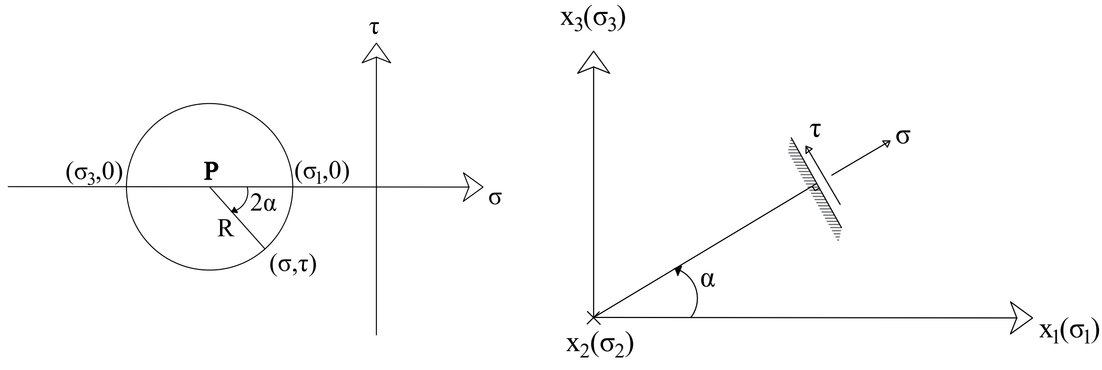

(a) (b)

Figure F.2: Mohr's stress circle and corresponding interpretation of τ and σ.

in Equation (F.11) and inserted in Equation (F.12), which yields:

$$P = \frac{1}{2}\left[(k+1)\sigma_1 - \sigma_c\right] \qquad R = \frac{1}{2}\left[\sigma_c - (k-1)\sigma_1\right] \tag{F.13}$$

by elimination of σ_1, Equation (F.14) is obtained:

$$R = \frac{\sigma_c}{k+1} - \frac{k-1}{k+1}\,P \tag{F.14}$$

Hence, the radius R varies linearly with the position of the center P.

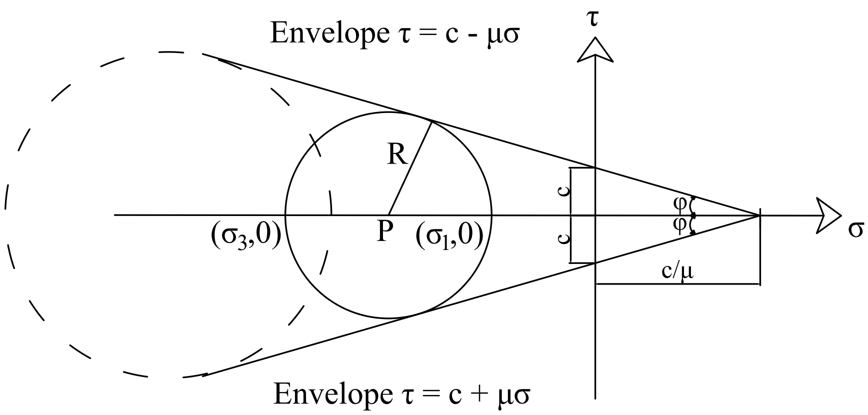

Figure F.3: Coulomb criterion in Mohr's diagram

Thereupon, as illustrated in Figure F.3, all the Mohr's circles of stress that fulfill the Coulomb criterion have two symmetrically positioned straight lines as their envelopes. These straight lines can be written as:

$$|\tau| = c - \sigma_n \tan\phi \tag{F.15}$$

c	Cohesion
ϕ	Angle of internal friction
τ	Shear stress
σ_n	Normal stress

The normal and shear stresses represent the stresses acting in the plane where failure occurs though shear, with $\tan\phi$ acting like the friction coefficient, μ.

Mohr-Coulomb model G

This appendix deals with the Mohr-Coulomb material model which is used for interpreting the behavior of the soil, when plasticity is accounted for. The theory is based on Ottosen and Ristinmaa [2005] and PLAXIS [2016].

The Mohr-Coulomb material model, also known as linear perfectly plastic model, is a materiel model that can be used as a first approximation of soil behavior. The linear elastic part of the model is based ion Hooke's law of isotropic elasticity, while the perfectly plastic part of the model is based on the Mohr-Coulomb failure criterion. Thus the Coulomb criterion is introduced. In Appendix F it is explained that the the yield criterion of a soil material is expressed by the principle stresses, σ_1, σ_2 and σ_3, as shown in Equation (F.2), repeated below:

$$F(\sigma_1, \sigma_2, \sigma_3) = 0$$

As mentioned in Appendix F, the Coulomb yield criterion is expressed in Equation (F.10), repeated below:

$$k\,\sigma_1 - \sigma_3 - m = 0$$

The material parameters, k and m, depend on the friction angle and the failure stresses in an uniaxial tension and compression. The yield surface of the Coulomb criterion in the deviatoric and meridian plan is presented in Figures G.1 and G.2.

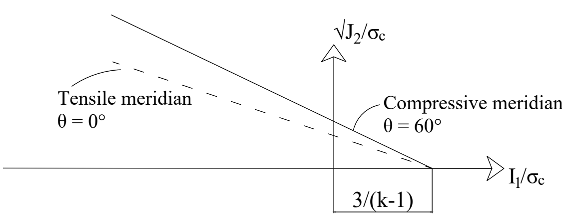

Figure G.1: Coulomb criterion in the meridian plan.

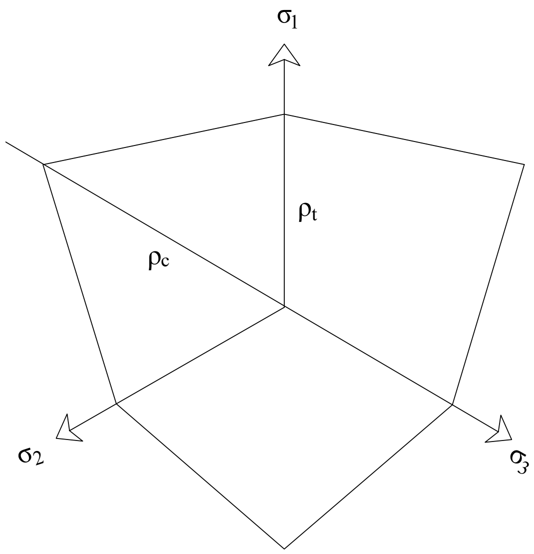

Figure G.2: Coulomb yield surface in the deviatoric plane.

In effect of the yield surface formulated by Coulomb criterion, the elastic material behavior can be accounted for inside the surface, while on the other hand the surface describes the failure or yielding of the material, $F = 0$.

G.1 Formulation for the Mohr-Coulomb model

The yield surface is fixed in the principle and deviatioric stress space while undergoing plastic straining. For any stress state of a point inside the yield surface, the behavior of the material is purely elastic, meaning that all strains are reversible. Stress states represented by point on or outside the yield surface, the behavior of the material is plastic, meaning that the plastic part of the strains is irreversible.

Mohr-Coulomb model introduces several yield functions, f_i, as a function of stresses and strains to determine whether or not plasticity occurs in the model. Plstic yielding is still related to the criterion $f = 0$, due to that the yield surface is presented in the principle stress state. The full Mohr-Coulomb model is represented by six yield functions formulated in terms of principle stresses. The yield functions are represented in Equations (G.1) to (G.6):

$$f_{1a} = \frac{1}{2}(\sigma_2' - \sigma_3') + \frac{1}{2}(\sigma_2' - \sigma_3')\sin\varphi - c\,\cos\varphi \leq 0 \tag{G.1}$$

$$f_{1b} = \frac{1}{2}(\sigma_3' - \sigma_2') + \frac{1}{2}(\sigma_3' - \sigma_2')\sin\varphi - c\,\cos\varphi \leq 0 \tag{G.2}$$

$$f_{2a} = \frac{1}{2}(\sigma_3' - \sigma_1') + \frac{1}{2}(\sigma_3' - \sigma_1')\sin\varphi - c\,\cos\varphi \leq 0 \tag{G.3}$$

$$f_{2b} = \frac{1}{2}(\sigma_1' - \sigma_3') + \frac{1}{2}(\sigma_1' - \sigma_3')\sin\varphi - c\,\cos\varphi \leq 0 \tag{G.4}$$

$$f_{3a} = \frac{1}{2}(\sigma_1' - \sigma_2') + \frac{1}{2}(\sigma_1' - \sigma_2')\sin\varphi - c\,\cos\varphi \leq 0 \tag{G.5}$$

$$f_{3b} = \frac{1}{2}(\sigma_2' - \sigma_1') + \frac{1}{2}(\sigma_2' - \sigma_1')\sin\varphi - c\,\cos\varphi \leq 0 \tag{G.6}$$

The condition, $f_i = 0$, for all yield functions together, represents a fixed hexagonal cone in the principle stress space, illustrated in Figure G.3:

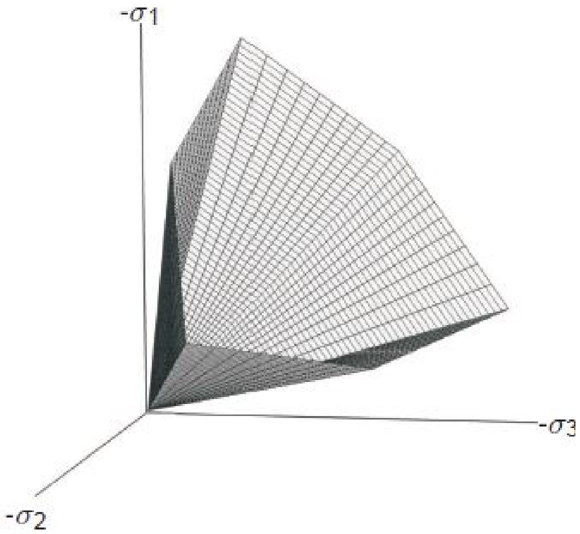

Figure G.3: Mohr-Coulomb yield surface in principle stress space ($c = 0$), PLAXIS [2016].

By solely use of these yield functions, the plastic strains are determined for associate flow, which have been proven to overestimate the dilantancy. To account for the dilatational behavior, six plastic potential functions have been introduced for the Mohr-Coulomb model with the dilatancy angle ψ as a plastic parameter. The dilatancy angle is required to model positive plastic volumetric strain increments as actually observed for dense soils. These function are defined in Equation (G.7) to (G.12):

$$g_{1a} = \frac{1}{2}\left(\sigma_2' - \sigma_3'\right) + \frac{1}{2}\left(\sigma_2' + \sigma_3'\right)\sin\psi \tag{G.7}$$

$$g_{1b} = \frac{1}{2}\left(\sigma_3' - \sigma_2'\right) + \frac{1}{2}\left(\sigma_3' + \sigma_2'\right)\sin\psi \tag{G.8}$$

$$g_{2a} = \frac{1}{2}\left(\sigma_3' - \sigma_1'\right) + \frac{1}{2}\left(\sigma_3' - \sigma_1'\right)\sin\psi \tag{G.9}$$

$$g_{2b} = \frac{1}{2}\left(\sigma_1' - \sigma_3'\right) + \frac{1}{2}\left(\sigma_1' - \sigma_3'\right)\sin\psi \tag{G.10}$$

$$g_{3a} = \frac{1}{2}\left(\sigma_1' - \sigma_2'\right) + \frac{1}{2}\left(\sigma_1' - \sigma_2'\right)\sin\psi \tag{G.11}$$

$$g_{3b} = \frac{1}{2}\left(\sigma_2' - \sigma_1'\right) + \frac{1}{2}\left(\sigma_2' - \sigma_1'\right)\sin\psi \tag{G.12}$$

When implementing the Mohr-Coulomb model for general stress state some special requirements have to be done for the interaction between two surfaces. The transition between two surfaces can either be smooth of sharp. When dealing with this, PLAXIS uses exact form for full Mohr-Coulomb model implemented and using a sharp transition from one yield surface to another.

By implementation of the Mohr-Coulomb criterion for $c > 0$, it allows some tension, meaning that with increase in tensile stresses the cohesion increases. Generally, soil can sustain none or only very small tension stresses. PLAXIS includes this behavior the its analysis by specifying a tension cut-off, where Mohr circles with positive principle stresses are not allowed. The term tension cut-off introduced three new yield functions defined from Equation (G.13) to (G.15):

$$f_4 = \sigma_1' - \sigma_t \leq 0 \tag{G.13}$$

$$f_5 = \sigma_2' - \sigma_t \leq 0 \tag{G.14}$$

$$f_6 = \sigma_3' - \sigma_t \leq 0 \tag{G.15}$$

where the $\sigma_t = 0$ when using the tension cut-off procedure.

Overall, the Mohr-Coulomb model can account for non-associated flow, in addition to tension cut-off. The model is widely used due to its simplicity, and only require five parameters that are friction angle φ, cohesion c, dilatancy angle ψ, Young's elastic modulus E and friction coefficient μ.

Axisymmetric element H

In this appendix the axisymmetry of finite element formulation is described in regard to three noded triangular element with cylindrical coordinates. Throughout this appendix NPTEL [2015] and Logan [2017] will be used as a source.

H.1 Introduction

Several three-dimensional problems can be solved using two-dimensional finite elements, thus the considered problem can fulfill the criteria of axisymmetry. If the problem geometry is symmetric around an axis, usually the axis of rotation, and the loading and the boundary conditions are symmetric around the same axis, the problem can be defined as axisymmetric. Axisymmetric problems are defined by polar coordinate system with coordinates (r, θ, z). Following an axisymmetric analysis, the following conditions must be fulfilled:

1. The domain should have an axis of symmetry and is conveniently considered as z axis.
2. The loading of the domain have to be symmetric around the axis of revolution, thus the loads are independent of the circumferential coordinate θ.
3. The boundary conditions and material properties are symmetric around the same axis and will be independent of circumferential coordinate.

Axisymmetric bodies are totally symmetric around the axis of revolution (i. e., z-axis), the field variables, such as the stress and deformation are independent of the rotational angle θ. Therefore the field variables can be defined as functions of (r, θ), hence making the problem two-dimensional. The axisymmetric problem included in this report are a circular footing on a soil domain with uniform loading, shown in Figure H.1. In the following sections, the axisymmetric finite element formulation will be derived.

H.2 Relation between strain and displacement

Axisymmetric problems are preferably described by cylindrical polar coordinates: r, θ and z. In this case, θ measures the plane containing a considered point and the axis of the coordinate system. At $\theta = 0$, the radial and axial coordinates correspond with the global Cartesian x and y coordinates. Figure H.2 shows the cylindrical coordinate system both including the Cartesian and cylindrical coordinates. Let r*, θ* and z* be unit vectors in the radial, circumferential and and axial direction at a point in the cylindrical coordinate system. If the material properties and the loading, either radial or axial components, are independent of θ will the displacement at any point only have radial (u_r) and axial (u_z)

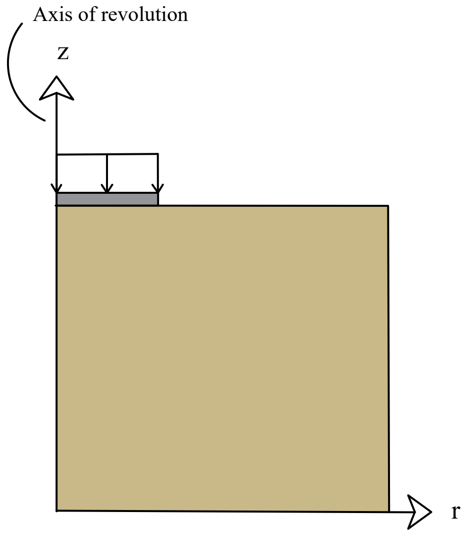

Figure H.1: Axisymmetric footing on a soil domain with an uniform load.

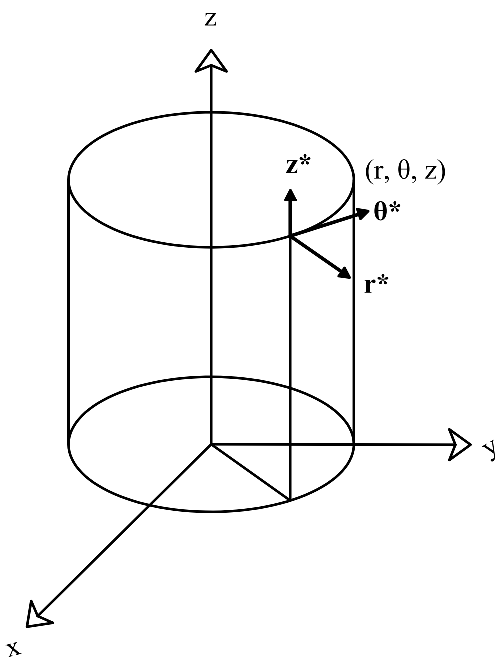

Figure H.2: Cylindrical coordinate system.

components. Including the only stress components that are nonzero are $\sigma_{rr}, \sigma_{\theta\theta}, \sigma_{zz}$ and τ_{rz}.

For the case of that the element experiences deformation the in radial direction, it will initiate an increase in circumference and associated circumferential strain. The radial displacement is defined as u, the circumferential displacements is defined as v, whereas the axial displacement is defined as w. Figure H.3 shows the deformed positions of the element illustrated with thicker line, where the dashed line represents the initial element form.

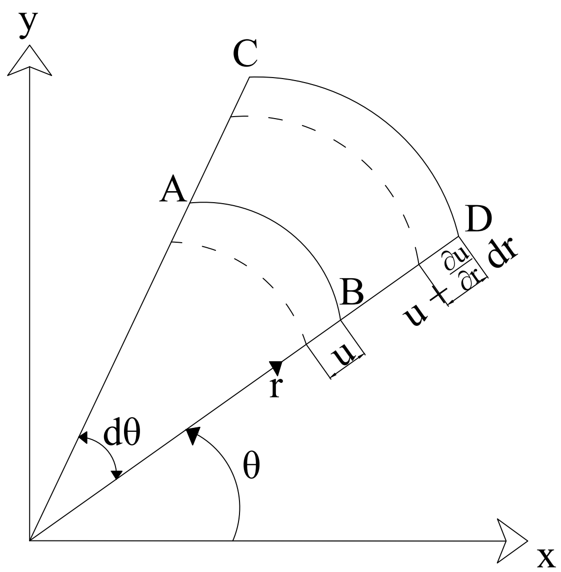

Figure H.3: Element in r-θ plane.

Thus, the strains can be calculated as shown in:

$$\varepsilon_r = \frac{1}{dr}\left(u + \frac{\partial u}{\partial r}\,dr - u\right) = \frac{\partial u}{\partial r} \tag{H.1}$$

$$\varepsilon_z = \frac{1}{dz}\left(w + \frac{\partial w}{\partial z}\,dz - w\right) = \frac{\partial w}{\partial z} \tag{H.2}$$

After deformation, the deformed arc length have expanded from its initial arc length in the circumferential direction. By defined the initial arc length as $ds = r\,d\theta$, the arc length after deformation is obtained by $ds = (r+u)\,d\theta$. This gives the tangential strain by:

$$\varepsilon_\theta = \frac{(r+u)\,d\theta - r\,d\theta}{r\,d\theta} = \frac{u}{r} \tag{H.3}$$

Due to that the r-z plane is similar to the x-y coordinate system, the shear strains can be expressed as:

$$\gamma_{rz} = \frac{\partial u}{\partial z} + \frac{\partial w}{\partial r} \tag{H.4}$$

$$\gamma_{r\theta} = 0 \quad \text{and} \quad \gamma_{z\theta} = 0$$

The strains can be written in matrix from as shown in:

$$\{\varepsilon\} = \begin{Bmatrix} \varepsilon_r \\ \varepsilon_z \\ \varepsilon_\theta \\ \gamma_{rz} \end{Bmatrix} = \begin{Bmatrix} \frac{\partial u}{\partial r} \\ \frac{\partial w}{\partial z} \\ \frac{u}{r} \\ \frac{\partial u}{\partial z} + \frac{\partial w}{\partial r} \end{Bmatrix} = \begin{bmatrix} \frac{\partial}{\partial r} & 0 \\ 0 & \frac{\partial}{\partial z} \\ \frac{1}{r} & 0 \\ \frac{\partial}{\partial z} & \frac{\partial}{\partial r} \end{bmatrix} \begin{Bmatrix} u \\ w \end{Bmatrix} \tag{H.5}$$

H.3 Stress-strain relationship

The isotropic stress-strain relationship can be derived from the three dimensional constitutive relations corresponding to a three dimensional solid, which are known as:

$$\begin{Bmatrix} \sigma_x \\ \sigma_y \\ \sigma_z \\ \tau_{xy} \\ \tau_{yz} \\ \tau_{zx} \end{Bmatrix} = \frac{E}{(1+\nu)(1-2\nu)} \begin{bmatrix} 1-\nu & \nu & \nu & 0 & 0 & 0 \\ \nu & 1-\nu & \nu & 0 & 0 & 0 \\ \nu & \nu & 1-\nu & 0 & 0 & 0 \\ 0 & 0 & 0 & \frac{1-2\nu}{2} & 0 & 0 \\ 0 & 0 & 0 & 0 & \frac{1-2\nu}{2} & 0 \\ 0 & 0 & 0 & 0 & 0 & \frac{1-2\nu}{2} \end{bmatrix} \begin{Bmatrix} \varepsilon_x \\ \varepsilon_y \\ \varepsilon_z \\ \gamma_{xy} \\ \gamma_{yz} \\ \gamma_{zx} \end{Bmatrix} \tag{H.6}$$

ν	Poisson's ratio
E	Young's modulus

By comparing the stress-strain components present in the axisymmetric case, the stress-strain relationship can be expressed from:

$$\begin{Bmatrix} \sigma_r \\ \sigma_z \\ \sigma_\theta \\ \tau_{rz} \end{Bmatrix} = \frac{E}{(1+\nu)(1-2\nu)} \begin{bmatrix} 1-\nu & \nu & \nu & 0 \\ \nu & 1-\nu & \nu & 0 \\ \nu & \nu & 1-\nu & 0 \\ 0 & 0 & 0 & \frac{1-2\nu}{2} \end{bmatrix} \begin{Bmatrix} \varepsilon_r \\ \varepsilon_z \\ \varepsilon_\theta \\ \gamma_{rz} \end{Bmatrix} \tag{H.7}$$

Hence, the constitutive matrix $[D]$ for an axisymmetric elastic solid is given by:

$$[D] = \frac{E}{(1+\nu)(1-2\nu)} \begin{bmatrix} 1-\nu & \nu & \nu & 0 \\ \nu & 1-\nu & \nu & 0 \\ \nu & \nu & 1-\nu & 0 \\ 0 & 0 & 0 & \frac{1-2\nu}{2} \end{bmatrix} \tag{H.8}$$

H.4 Finite element formulation

Finite element formulation of an axisymmetric problem is derived similarly as for a two dimensional solid element. As mentioned in Section H.2, the stresses and strains are independent of the rotational angle θ, thus no circumferential displacement will be present. Therefore the displacement field variables will be obtained in:

$$u(r,z) = \sum_{i=1}^{n} N_i(r,z)\, u_i \tag{H.9}$$

$$w(r,z) = \sum_{i=1}^{n} N_i(r,z)\, w_i \tag{H.10}$$

u_i	Radial nodal displacements
w_i	Axial nodal displacements
$N_i(r,z)$	Shape functions

Due to the independence of the rotational angle θ, interpolation function $N_i(r,z)$ can be expressed similar to two dimensional problems by replacing the variables x and y terms with r and z respectively.

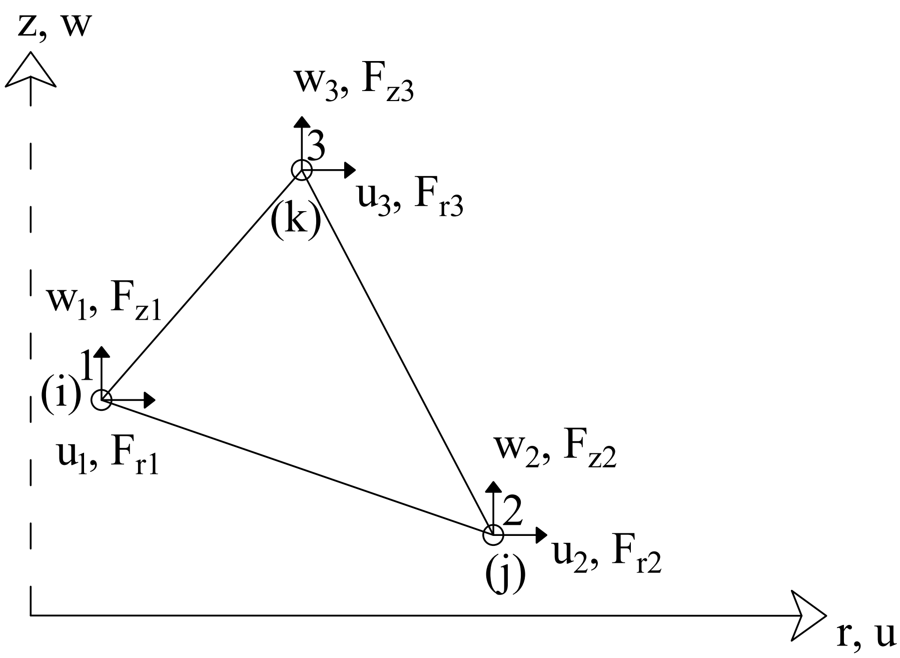

Figure H.4: Axisymmetric three node triangle in cylindrical coordinates

For simplicity, a three noded triangular element with cylindrical coordinates is derived, that are illustrated in Figure H.4. Therefore, the analysis for the axisymmetric element can be performed in a similar manner as for CST elements, where the element displacements functions can be expressed as:

$$\begin{aligned} u(r,z) &= \alpha_1 + \alpha_2\, r + \alpha_3\, z \\ w(r,z) &= \alpha_4 + \alpha_5\, r + \alpha_6\, z \end{aligned} \tag{H.11}$$

or:

$$\{d\} = [\phi]\,\{\alpha\} \tag{H.12}$$

where:

$$\{d\} = \begin{Bmatrix} u \\ w \end{Bmatrix} \qquad [\phi] = \begin{bmatrix} 1 & r & z & 0 & 0 & 0 \\ 0 & 0 & 0 & 1 & r & z \end{bmatrix} \quad \text{and} \quad \{\alpha\}^T = \{\alpha_1\alpha_2\alpha_3\alpha_4\alpha_5\alpha_6\}$$

Rewriting the above equations into full matrix form yields:

$$\begin{Bmatrix} u_1 \\ u_2 \\ u_3 \\ w_1 \\ w_2 \\ w_3 \end{Bmatrix} = \begin{bmatrix} 1 & r_i & z_i & 0 & 0 & 0 \\ 1 & r_j & z_j & 0 & 0 & 0 \\ 1 & r_k & z_k & 0 & 0 & 0 \\ 0 & 0 & 0 & 1 & r_i & z_i \\ 0 & 0 & 0 & 1 & r_j & z_j \\ 0 & 0 & 0 & 1 & r_k & z_k \end{bmatrix} \begin{Bmatrix} \alpha_1 \\ \alpha_2 \\ \alpha_3 \\ \alpha_4 \\ \alpha_5 \\ \alpha_6 \end{Bmatrix} \tag{H.13}$$

or:

$$\begin{aligned} \{\bar{d}\} &= [A]\{\alpha\} \\ \alpha &= [A]^{-1}\{\bar{d}\} \end{aligned} \tag{H.14}$$

$\{\bar{d}\}$	nodal displacement vectors

Inserting Equation (H.14) into Equation (H.12), yields the expression in:

$$\{d\} = [N]\{\bar{d}\} \tag{H.15}$$

or:

$$\begin{Bmatrix} u \\ w \end{Bmatrix} = \begin{bmatrix} N_i & N_j & N_k & 0 & 0 & 0 \\ 0 & 0 & 0 & N_i & N_j & N_k \end{bmatrix} \begin{Bmatrix} r_1 \\ r_2 \\ r_3 \\ z_1 \\ z_2 \\ z_3 \end{Bmatrix} \tag{H.16}$$

where the shape functions $[N_i, N_j, N_k]$ are functions the r and z coordinates. Combining Equation (H.16) into Equation (H.5), gives:

$$\{\varepsilon\} = [B]\{\bar{d}\} = \begin{bmatrix} \frac{\partial N_i}{\partial r} & \frac{\partial N_j}{\partial r} & \frac{\partial N_k}{\partial r} & 0 & 0 & 0 \\ \frac{N_i}{r} & \frac{N_j}{r} & \frac{N_k}{r} & 0 & 0 & 0 \\ 0 & 0 & 0 & \frac{\partial N_i}{\partial z} & \frac{\partial N_j}{\partial z} & \frac{\partial N_k}{\partial z} \\ \frac{\partial N_i}{\partial z} & \frac{\partial N_j}{\partial z} & \frac{\partial N_k}{\partial z} & \frac{\partial N_i}{\partial r} & \frac{\partial N_j}{\partial r} & \frac{\partial N_k}{\partial r} \end{bmatrix} \begin{Bmatrix} r_1 \\ r_2 \\ r_3 \\ z_1 \\ z_2 \\ z_3 \end{Bmatrix} \tag{H.17}$$

where the strain interpolation matrix is defined as $[B]$ and $r = \frac{r_i + r_j + r_k}{3}$. The stresses are given as:

$$\{\sigma\} = [D]\{\varepsilon\} \tag{H.18}$$

Thus, the stiffness matrix is defined as in Equation (H.19):

$$[K] = \iiint_V [B]^T [D] [B] \, dV \tag{H.19}$$

If an integration is performed along the circumferential boundary, can Equation (H.19) be rewritten as:

$$[K] = 2\pi \iint_A [B]^T [D] [B] r \, dr \, dz \tag{H.20}$$